Remora-Inspired Dynamic Recovery Strategies for the Autonomous Underwater Vehicle

By

Yunxin Xu

Student Registration Number: 201978657

A THESIS

Submitted in partial fulfilment of the requirements for the degree of

PhD- Naval Architecture with Ocean Engineering

UNIVERSITY OF STRATHCLYDE

Declaration

This thesis is the result of the author's original research. It has been composed by the author and has not been previously submitted for examination which has led to the award of a degree.

The copyright of this thesis belongs to the author under the terms of the United Kingdom Copyright Acts as qualified by University of Strathclyde Regulation. Due acknowledgement must always be made of the use of any material contained in, or derived from, this thesis.

This thesis has been approved in partial fulfilment of the requirements for the Degree of Doctor of Engineering in Naval Architecture with Ocean Engineering, Department of Naval Architecture, Ocean and Marine Engineering.

Thesis Advisor: *Weichao Shi, Laibing Jia, Yigit Kemal Demirel*

Student Name: Yunxin Xu

Signature: Yunxin Xu

Date: 30/06/2023

Acknowledgements

This thesis journey has been deeply influenced by numerous individuals and experiences, and I am grateful to all who have contributed to its completion. First and foremost, I would like to express my heartfelt gratitude to my principal supervisor, Dr. Weichao Shi. Your support, guidance, and patience have been instrumental in shaping this research. Beyond academic mentorship, your genuine concern for my personal well-being has been profoundly appreciated.

I would also like to extend my sincere thanks to another supervisor, Dr. Laibing Jia. Your support during the latter stages of my thesis and your attention to both my academic progress and personal challenges have been invaluable. Additionally, I am grateful to my co-supervisor, Dr. Yigit Kemal Demirel.

My sincere thanks also go to the colleagues and friends in the Applied Biomimetics Marine Hydrodynamics Research Group and the NAOME Department. Zhongsheng, Callum, Abel, Hongbo, Moritz, Yang, Guangwei, Yi, Kaan, Zeynep, and others—thank you for your collaboration and help. I was particularly fortunate to meet Zhongsheng as a master's student, and we spent the whole of our PhDs together.

I must also highlight the immense support of my family. To my parents, sister, and brother-in-law: your constant encouragement and support during the pandemic and other challenges have been my pillar of strength. Without your unwavering belief in me, this journey would have been far more arduous.

In closing, I recognize the broader challenges posed by the pandemic, which added layers of difficulty to this endeavour. Personal struggles during and after this period have tested my resilience, but the support from all these wonderful individuals has made a tremendous difference. Thank you all for being an integral part of this journey.

Abstract

Autonomous Underwater Vehicles (AUVs) are employed across various industries to enhance maritime operations' efficiency and safety. Traditional AUV docking and recovery techniques often face inefficiencies, necessitating the development of a dynamic underwater recovery mechanism. This thesis explores the design and development of a remora-inspired AUV equipped with an innovative dynamic recovery system. Drawing inspiration from the unique adhesion and hitchhiking behaviours of remora fish, the research addresses AUV recovery challenges by leveraging biomimetic principles.

The study begins by examining the hydrodynamic mechanisms of the remora fish to understand their efficient swimming and attachment strategies, which serve as a foundation for novel AUV design. Numerical simulations demonstrate that remora fish exploit the boundary layer and the adverse pressure gradient regions around sharks to significantly reduce resistance. Building on these insights, a remora-inspired AUV is developed, and its hydrodynamic performance is assessed using computational fluid dynamics simulations. The research then identifies optimal attachment locations on a benchmark submarine, focusing on drag reduction and operational feasibility.

Further simulations explore the hydrodynamic characteristics of the AUV during the docking process, particularly as it enters the submarine's boundary layer and approaches it. The docking processes can be analysed in five stages: approach, enter, contact, bounce and attach. After the docking process, this boundary layer flow not only affect the AUV's resistance but also generates a force that attracts the AUV toward the submarine.

This study investigates the reasons behind remora’s choice of attachment locations, identifies optimal attachment sites for AUVs, and examines the effects on AUVs when two underwater vehicles of significantly different sizes are in close proximity. The findings lay the groundwork for future research aimed at developing dynamic underwater docking operations.

Contents

List of Figures

List of Tables

Chapter 1

Introduction

The primary goal of this chapter is to introduce the PhD project, which aims to develop a novel dynamic recovery strategy for AUVs inspired by the swimming strategy of the remora fish. Section 1.1 provides the background and motivation behind the research, followed by the main aim and objectives of the project in section 1.2. The structure of the thesis chapters is outlined in section 1.3, while a brief summary of this chapter is presented in section 1.4.

1.1 Background and Motivation

The study of the ocean and its vast ecosystems plays a crucial role in the sustainable development and well-being of our planet. As a significant part of Earth's environment, the oceans cover approximately 70% of the planet's surface, regulate climate patterns, support biodiversity, and provide valuable resources and ecosystem services. Understanding and exploring the ocean is essential for addressing pressing environmental challenges, managing marine resources sustainably, and advancing scientific knowledge [1-6]. Traditionally, ocean research heavily relied on ships and manned vehicles to collect data and explore the underwater world. These methods have contributed significantly to our understanding of the oceans but have inherent limitations. Ships are expensive to operate, requiring significant financial resources and a substantial crew. They are also constrained by their size and mobility, often unable to access remote or inaccessible regions, such as deep-sea trenches or polar ice caps. Moreover, the presence of humans and the noise generated by ships can disturb marine life and alter natural behaviours, potentially impacting the accuracy of scientific observations [7, 8].

Since the 1960s, the development of Autonomous Underwater Vehicles (AUVs) has significantly transformed the field of ocean research. AUVs have revolutionised traditional research methods by providing numerous advantages depending on the specific environment and research objectives. These advantages include improved manoeuvrability, extended research and monitoring capabilities, reduced disruption to marine ecosystems, and cost-effectiveness. Consequently, AUVs have found extensive applications across a wide range of industries, such as ocean surveying, surveillance, pipeline inspection, treasure hunting, and search and rescue missions [9-14].

Despite the numerous benefits they offer, the recovery of AUVs remains one of the most challenging and risky stages of a mission. The development of reliable recovery technology faces several obstacles [15-18]. The traditional method for recovering AUVs involves a surface mothership traveling to the AUV's location using GPS signals and employing an 'A'-frame or onboard crane for retrieval. However, this approach presents several challenges, including the requirement for precise location information and the difficulty of recovering AUVs in adverse weather conditions without causing damage [16].

Figure 1-1 Recovering a MBARI Mapping AUV onto the R/V Rachel Carson [19].

To overcome these challenges, researchers and engineers are exploring alternative methods to minimize the need for frequent retrieval for charging and communication. One emerging trend is the development of underwater docking stations that facilitate data transfer and charging [20-25]. However, these docking stations are typically stationary and limited to known areas. On the other hand, there have been efforts to develop unmanned surface vehicles (USVs) capable of automatically launching and recovering AUVs [26-32]. Nevertheless, these solutions are also stationary and susceptible to weather conditions. At the moment, there is no efficient method available for dynamically recovering AUVs.

The development of AUVs remains an active area of research, and addressing this challenge is crucial to enhance the autonomy and operational capabilities of AUVs. By overcoming the limitations associated with current recovery methods, dynamic recovery systems could significantly improve the efficiency of AUV missions, enabling longer deployment durations and enhanced data collection. Therefore, the development of efficient and robust dynamic recovery technologies is a pressing research priority in the field of AUVs.

Figure 1-2 The unique docking behaviour of remora fishes with the shark [33].

To tackle this challenging problem of dynamic AUV recovery, a natural cooperative relationship observed between remora fish and sharks is inspiring (Figure 1-2). Remora fish, also referred to as "suckerfish," exhibit a unique attachment behaviour and are often found attached to a host rather than swimming independently. The fish attach to their hosts in order to travel and forage, compensating for their limited swimming abilities.

While remora fish attach to various marine organisms such as sharks, turtles, and man-made marine vehicles, their attachment positions on the host's body are not randomly chosen [34-36]. Brunnschweiler, J.M. [34] found that nearly 40% of the attachments (137 out of 345) have been performed near the sharks' belly area, followed by 27% at the back and with the lowest number of attachments in the caudal fin area. This intriguing behaviour has prompted numerous researchers to investigate the reasons behind it. From a marine biology perspective, it was suspected that remora fish tend to select positions that do not irritate the host [36]. Additionally, they prefer locations with minimal motion and deformation when the host is swimming, ensuring a stable platform for attachment [35]. Flammang, et al. [37] found that the remora fish prefer regions with lower drag, and as they approach a host surface, a suction effect help them to stay close. However, detailed knowledge about the hydrodynamic effects of attachment locations is still lacking. Therefore, further investigation is required to understand the hydrodynamic impact on remora fish due to different attachment positions.

The hydrodynamic characteristics of remora fish in different attachment locations have served as a key source of inspiration for this study on dynamic recovery systems for AUVs. In this study, the concept involves utilizing another larger underwater vehicle as a mother ship for the AUV recovery system. However, the interaction between two underwater vehicles of significantly different sizes, particularly in close proximity, has received relatively little attention in the existing research. Understanding the hydrodynamics of such interactions is crucial for the successful implementation of an efficient and reliable dynamic recovery system. The close proximity between the mother ship and the AUV during the recovery process introduces complex flow, hydrodynamic forces, and potential disturbances. These factors can significantly impact the stability, manoeuvrability, and safety of the recovery operation.

The above-reviewed developments and technical observations have motivated the author to explore and develop the feasibility of dynamic recovery systems for AUVs inspired by biomimetic principles.

1.2 Aim and Objectives

Based on the motivation and literature review presented in Chapter 2, this PhD research aims to explore the hydrodynamics feasibility of a novel dynamic recovery strategy for AUVs, learning from the remora fish's hitchhiking strategy.

In order to achieve the above aim, the following objectives were specified:

- **Objective 1**: Review the literature to examine the current state-of-the-art AUV recovery strategies and explore the applications of biomimetic principles in order to refine the development approach; conduct a comprehensive review to obtain a deeper understanding of the research topics and identify the gaps in knowledge that require attention in current research within this field; propose an appropriate research methodology to effectively achieve the aims and objectives of the research.

- **Objective 2**: Conduct an investigation into the hydrodynamics mechanism of the remora fish swimming to understand its behaviour from a hydrodynamic point of view.

- **Objective 3**: Develop a AUV inspired by remora fish and understand its hydrodynamic performance for the following study.

- **Objective 4**: Investigate the hydrodynamic characteristics of the remora-inspired AUV attached to various locations of the submarine and identify the optimal docking location.

- **Objective 5**: Investigate the process of the docking and the forces experienced in the docking process when docking a remora-inspired AUV to a benchmark submarine with the fixed AUV attitude and variable AUV attitude, and the influence of different approaching paths on the docking operation.

1.3 Thesis Layout

The aim and objectives of the research have been successfully addressed through the work conducted in this study, which is presented in several chapters of the thesis. A brief overview of each chapter is provided following:

- **Chapter 1** provides an introduction to the research conducted in this thesis, presenting the background, author's motivation, aim and objectives, and an overview of the thesis layout. It serves as a concise introduction to the research carried out in the subsequent chapters.

- **Chapter 2** presents a comprehensive literature review on state of the art for AUV recovery strategies and explore the applications of biomimetic principles, which targets ‘Objective 1’. This is to get a broader understanding of research topics and hence refine the aim and objectives of the thesis by identifying the knowledge gaps that needed to be addressed in this research.

- **Chapter 3** is dedicated to ‘Objective 2’ to understand the hydrodynamic characteristics of the remora docking to the shark. The results will form the foundations to investigate the feasibility of dynamically docking a novel remora-inspired AUV to a submerged mother vehicle.

- **Chapter 4** centres on ‘Objective 3’, which aims to develop a new design AUV inspired by the remora. The principal goal is to investigate the hydrodynamic performance of the remora-inspired AUV, thereby establishing a foundational benchmark for subsequent analyses.

- **Chapter 5** focuses on 'Objective 4' to identify the optimum docking location for the remora-inspired AUV attached to a full-scale self-propelled submarine, and also the effect of the submarine's forward velocity. This is to provide a foundation for the next chapter's analysis on the AUV docking process.

- **Chapter 6** undertakes a fully coupled analysis to satisfy 'Objective 5'. The chapter conducts two types of simulations aimed at exploring the hydrodynamic characteristics of the remora-inspired AUV during the docking process. These simulations serve to identify the various stages of the docking process are identified and evaluate the impact on the AUV when it comes into close proximity with underwater vehicles of significantly different sizes.

- **Chapter 7** presents a detailed overview of the study conducted by scrutinising its aim and objectives as well as the main conclusions drawn from the research work. The chapter also recommended further work on future studies to be carried out.

1.4 Summary

Chapter 1 serves as an introduction to the research project presented in the thesis. It provides an overview of the motivation, aim, and objectives of the research, along with an outline of the thesis structure. This chapter offers a concise introduction to the conducted research study.

Chapter 2

Literature Review

The primary focus of this chapter is to define the aim and objectives of the research through a comprehensive review of the existing literature. This process involved identifying the current gaps in knowledge within the state-of-the-art literature concerning different Autonomous Underwater Vehicle (AUV) recovery systems.

The chapter begins by reviewing the latest advancements in Autonomous Underwater Vehicles (AUVs) (Section 2.1). Next, recent progress in recovery systems is explored, focusing on various methods such as surface, seabed, and mid-water approaches to better understand their applications and limitations (Section 2.2). Subsequently, the distinctive adaptations and behaviours of remora fish are examined, highlighting their unique suction mechanisms and attachment strategies, which serve as a source of inspiration for innovative biomimetic applications in AUV dynamic recovery systems (Section 2.3). Finally, a summary of the findings and the current knowledge gaps have been addressed in confirming the aim and objectives of the thesis.

2.1 Autonomous Underwater Vehicles (AUVs)

Autonomous Underwater Vehicles (AUVs) are unmanned submersible vehicles designed to operate without a tether or immediate operator control, carrying out data collection based on pre-programmed instructions. The first AUV, known as the SPURV, was developed in 1957 at the Applied Physics Laboratory of the University of Washington in the USA. Its creation was motivated by the need to collect oceanographic data along precise trajectories, including under ice conditions [38, 39]. Since then, the development of AUVs has remained an active area of research. AUVs offer several advantages over traditional methods that rely on ships for ocean research. These advantages include higher autonomy, compact size, and the absence of physical connections. These characteristics make AUVs well-suited for overcoming the limitations of traditional research methods [40-42].

In comparison to early AUVs, modern AUVs have undergone significant advancements, becoming more compact, multifunctional, and cost-effective, thus AUVs are now widely used across a range of industries, including ocean surveying, surveillance, pipeline inspection, treasure hunting, and search and rescue missions [9-14]. Some AUVs are now even accessible for exploration and recreational purposes among the general population. Moreover, as AUV technology has progressed and mission requirements have diversified, AUVs can now be classified into three main types based on their movement modes: propelled AUVs, non-propelled AUVs, and biomimetic AUVs. These different types of AUVs cater to various applications and operational needs in the field.

a) Propelled AUVs

Traditional AUVs are commonly categorized as propelled AUVs, which utilize propellers or thrusters for propulsion. These AUVs typically adopt a torpedo-shaped body design inspired by torpedoes and submarines. Propelled AUVs excel in maintaining direct cruising and constant altitude, making them ideal for various research applications, including seafloor mapping and monitoring [13, 43-46]. In order to enhance their ability to collect seafloor data with higher resolution, propelled AUVs have undergone advancements in pressure resistance performance to meet the demands of research requirements. An example of a versatile industrial AUV is the 'REMUS-6000' (Figure 2-1), developed by The Oceanographic Systems Laboratory of the Woods Hole Oceanographic Institution. It has been employed in numerous mapping and search operations, such as the mapping of a section of the Roseau Fault [47] and the search for wreckage from Air France Flight 447 [48] (shown in Figure 2-1).

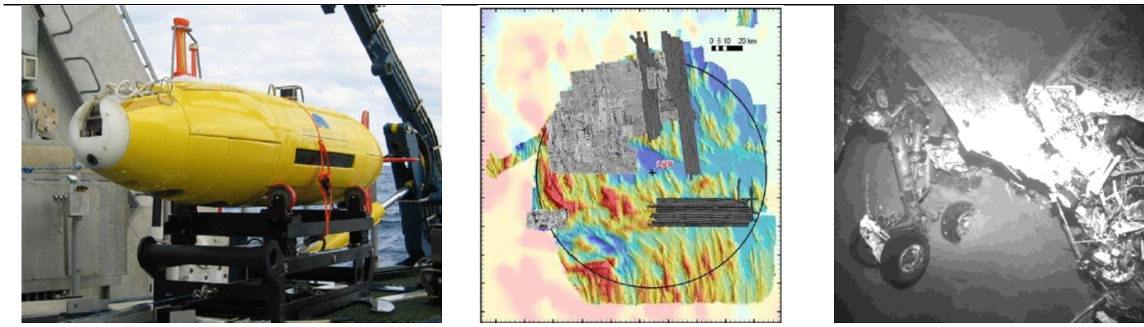

a. b. c.

Figure 2-1 REMUS 6000 AUVs were used in the wreckage search for the Air France Flight 447 a.) The Remus 6000 b.) Side scan coverage c.) Electronic still camera picture of landing gear [48].

b) Non-Propelled AUVs

Comparing propelled AUVs with non-propelled AUVs, the latter employ alternative propulsion methods that are specifically designed to suit particular operational goals and environments. These methods include underwater gliders, crawlers, jet-propelled AUVs, and sail-powered AUVs. While several types of non-propelled AUVs have been developed, the majority of those in service today are underwater gliders, such as Slocum [49], Spray [50], Seaglider [51], as Figure 2-2 shows.

a. b. c.

Figure 2-2 a.) Slocum glider [52] b.) Spray2 [53] c.) Seaglider [54].

Underwater gliders operate by controlling their buoyancy and mass position, allowing them to glide through the water. This means that underwater gliders must change their depth to achieve gliding motion, often following a zig-zag path [55, 56]. Due to their reliance on buoyancy systems and low-power components, underwater gliders are capable of covering long distances and undertaking extended-duration tasks. Additionally, since they use buoyancy instead of propellers for propulsion, underwater gliders are quieter during operation and are well-suited for tasks involving biomonitoring and other applications where minimal disturbance is critical [57-62].

c) Biomimetic AUVs

Biomimetic AUVs draw inspiration from marine animals such as fish, rays, and snakes for their design. These AUVs often feature biomimetic bodies that enhance hydrodynamic performance. They may incorporate fish-like designs with propulsion systems that use oscillating fins or an undulating body [63, 64]. Biomimetic AUVs leverage the advanced features found in the bodies and movements of marine animals. This can lead to increased propulsion efficiency, greater manoeuvrability, or improved stability in challenging environments. For some specific missions, biomimetic AUVs can even push the limits of traditional AUV technology [65-67].

a. b. c.

Figure 2-3 a.) GhostSwimmer [68] b.) Eelume [69] c.) Cownose ray robot [70].

Figure 2-3 displays several examples of biomimetic AUVs. Among them, GhostSwimmer, developed by the Boston Engineering group, draws inspiration from tuna fish. Primarily designed for military applications, it achieves locomotion by manipulating its dorsal, pectoral, and caudal fins [71-73]. The snake robot Eelume was designed for subsea resident inspection, maintenance, and repair (IMR) tasks. It offers several competitive advantages, including modularity, flexibility, two propulsion modes, and an adaptable shape for specific mission requirements [74]. The cownose ray robot propels itself by flapping its pectoral fins, a mechanism that offers benefits in terms of manoeuvrability and stability. Furthermore, this propulsion method is particularly advantageous for environmental monitoring and marine life observation since it doesn't disturb wildlife [70, 75-77].

In this section, the background and main types of the AUVs were introduced. Given the current and future advantages of Autonomous Underwater Vehicles (AUVs), they hold a crucial position in fields like marine research and operations. The versatility of AUVs allows them to effectively fulfil operational needs across different environments and tasks. In the case of specific tasks, such as Biomimetic AUVs, although these specialized designs may entail certain sacrifices in AUV performance, their targeted design is unparalleled. Hence, for the unique recovery scenario in this study, the hydrodynamic shape of the AUV will undergo biomimetic design to adapt to the dynamic recovery system.

2.2 AUV Recovery Systems

From the aforementioned reviews, diverse types of AUVs have been developed and are actively employed across various fields due to their notable advantages. However, regardless of the different types of AUVs, recovering AUVs remains one of the riskiest stages of a mission and the development of reliable recovery technology still faces several obstacles [15-18]. Hence, the development of AUV recovery systems has emerged as a global research focal point.

AUV recovery methods can be divided into three main types: surface recovery, seabed recovery, and mid-water recovery. The surface recovery method is the traditional approach and remains the primary method in use today. The seabed recovery method mainly employs a docking station located on the seabed, which serves as a base for charging, data collection, and relaunch. Mid-water recovery methods, including dynamic recovery systems and submarine recovery systems, are a popular research area. Detailed descriptions of these methods are provided in the following sections.

2.2.1 Surface Recovery: Traditional AUV Recovery Systems

Presently, the traditional AUV recovery systems are still primary recovery method. The traditional method for recovering AUVs primarily involves shipboard recovery techniques. In this approach, a dedicated vessel equipped with specialized tools and personnel trained in AUV recovery procedures is deployed. After completing its mission, the AUV ascends to a shallower depth or the water surface, facilitating easier access for recovery personnel. Skilled operators aboard the recovery vessel employ a combination of manual and mechanical methods to secure and lift the AUV safely. This can involve the use of ropes, hooks, and other physical tools. Additionally, some submarines equipped with a dry casing-mounted hangar also recover AUVs at the sea surface [78].The success of this process heavily depends on the coordination and expertise of the recovery team, particularly in adverse weather conditions or challenging sea states. Some vessels are equipped with specialized AUV handling systems such as A-frames, winches, or cranes [45]. These mechanical systems enhance the control and efficiency of the recovery process. While shipboard recovery techniques have demonstrated effectiveness, they are not without challenges. Adverse weather conditions, rough seas, and the need for skilled operators are factors that can impact the success of the recovery mission [16, 79].

a. b. c.

Figure 2-4 a.) A-frame on the vessel [80] b.) Small boat recovers a AUV [81]c.) Guiding the Autosub6000 to the positions underneath the LARS carriage [82].

2.2.2 Seabed Recovery: Underwater Docking Stations

Underwater docking stations serve as fixed base stations, providing functions such as recharging and data transfer for AUVs. These stations are securely positioned at known locations. When an AUV needs to replenish energy or transmit data, it can navigate to the nearest station to initiate the docking operation. Subsequently, the AUV can be relaunched for its next task. Currently, this static docking technology is relatively mature and is categorized into three main types based on the docking target: capture-type, guided-type, and landed-type [83-85].

a) The capture-type docking: the rope/pole as docking target

The docking approach requires the AUV to possess a capture mechanism capable of securing targets like ropes and poles to finalize the docking procedure. The merit of this docking technique lies in its relative resilience to external environmental disruptions, a heightened success rate for docking, and the capability for omnidirectional docking. Conversely, its drawback stems from the relatively intricate structure of the docking station, demanding certain modifications to the AUV. This method aligns well with AUVs featuring rotating body-shaped hulls, with the Odyssey IIB AUV underwater docking system from the United States serving as a prime example [20] (Figure 2-5). The docking apparatus primarily comprises two components. The V-shaped docking structure is employed to seize the docking pole linked to the docking station, while the spring-trigger mechanism ensures the docking pole remains securely locked in position, as shown.

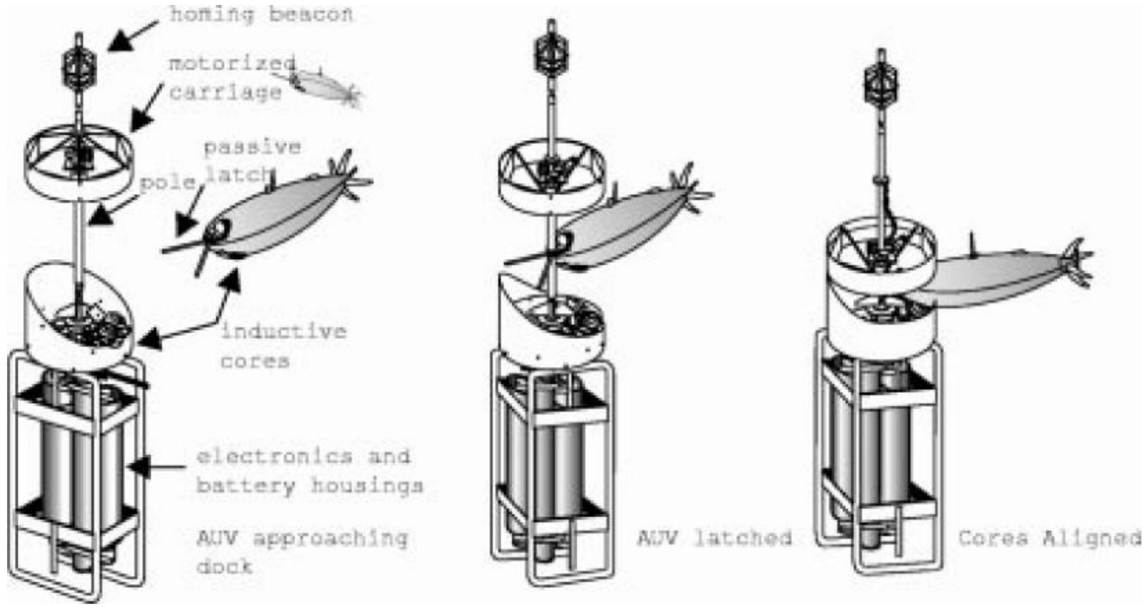

Figure 2-5 Underwater docking system of Odyssey IIB AUV [20].

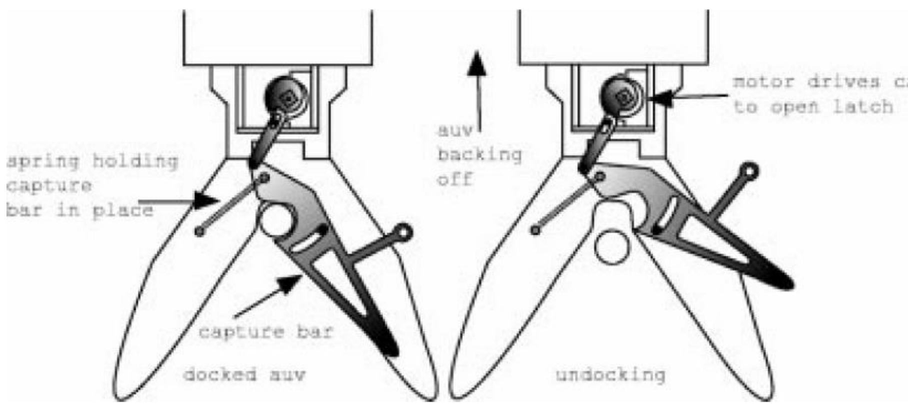

Figure 2-6 Spring-trigger mechanism for locking AUV [20].

b) The guided-type docking: the guide cage as docking target

The guided-type docking system requires the underwater docking station to feature a guiding cage-like mechanism, and the cone shaped funnel are the most common. This mechanism directs the AUV, facilitating its entry into the docking mechanism to complete the docking process. One of the merits of this docking technique is the relative simplicity of the underwater docking device. Upon docking, the device itself offers a certain degree of safeguarding to the AUV, protecting it from the effects of ocean currents. However, a limitation is its requirement for enhanced manoeuvrability and motion control capabilities for the AUV. In the meantime, a specific AUV size is required, too large or too small to use the station [86]. This method aligns well with cylindrical or torpedo-shaped AUVs with sleek surfaces, exemplified by the REMUS AUV underwater docking system from the United States [87] (Figure 2-7). The funnel-based design, owing to its inherent funnel shape, offers a superior capture envelope. As the AUV navigates into the funnel, it undergoes a combination of bouncing and sliding along the funnel's surface. Once inside the funnel, the AUV gets securely locked in, initiating the power transfer process. Subsequently, the AUV employs reverse thrust until it attains a safe distance, following which it recommences its designated mission [88].

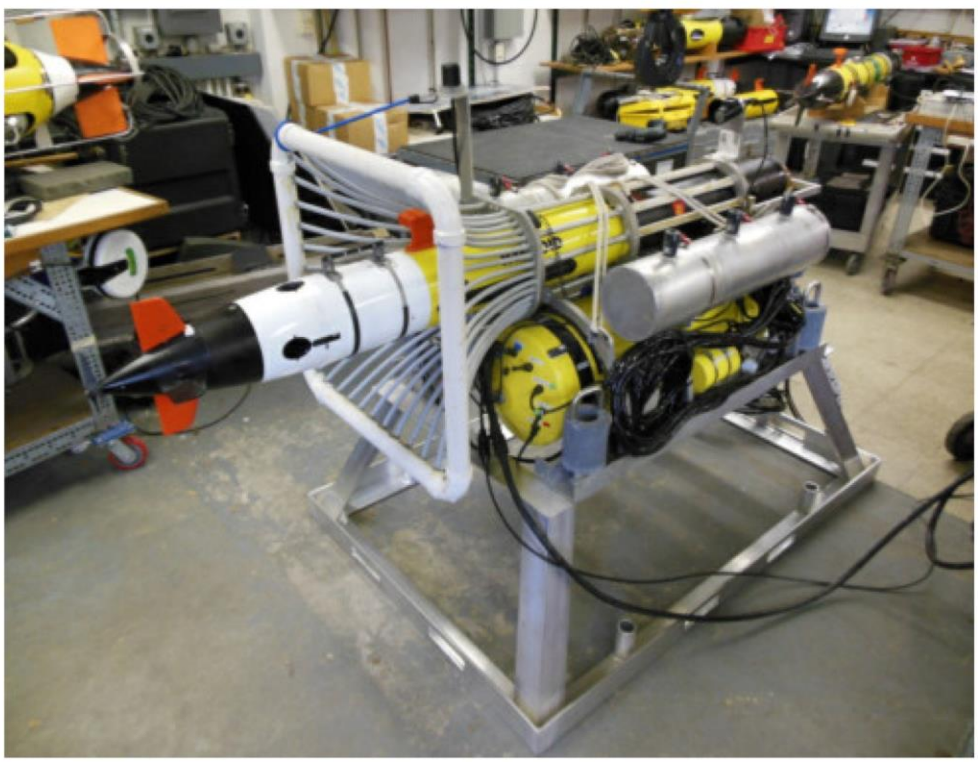

Figure 2-7 REMUS docking station [87].

c) The landed-type docking: the underwater platform as docking target

The landed-type docking system employs an underwater platform as the docking target, necessitating the AUV to land on a designated platform located on the seabed. This method utilizes a stationary docking station often equipped with visual markers or acoustic beacons to assist the AUV in precise navigation and alignment during the docking process. A key advantage of the landed-type docking system is its robustness in various underwater environments, offering stability and protection from dynamic water conditions such as currents and waves. The fixed nature of the platform simplifies docking mechanics and reduces the complexity of the docking infrastructure. However, this approach demands high-precision control and navigation capabilities from the AUV to ensure accurate landing on the platform. It also requires the AUV to have a flat or compatible surface for stable contact with the platform [64, 84]. A typical example is the Japanese MARINE BIRD underwater docking system, which operates on a principle similar to an airplane landing on an aircraft carrier. The AUV slowly navigates above the platform, captures the mechanism on the platform with a capture arm, and then locks the two together via a locking mechanism [89]. The MARINE BIRD docking process is illustrated in Figure 2-8.

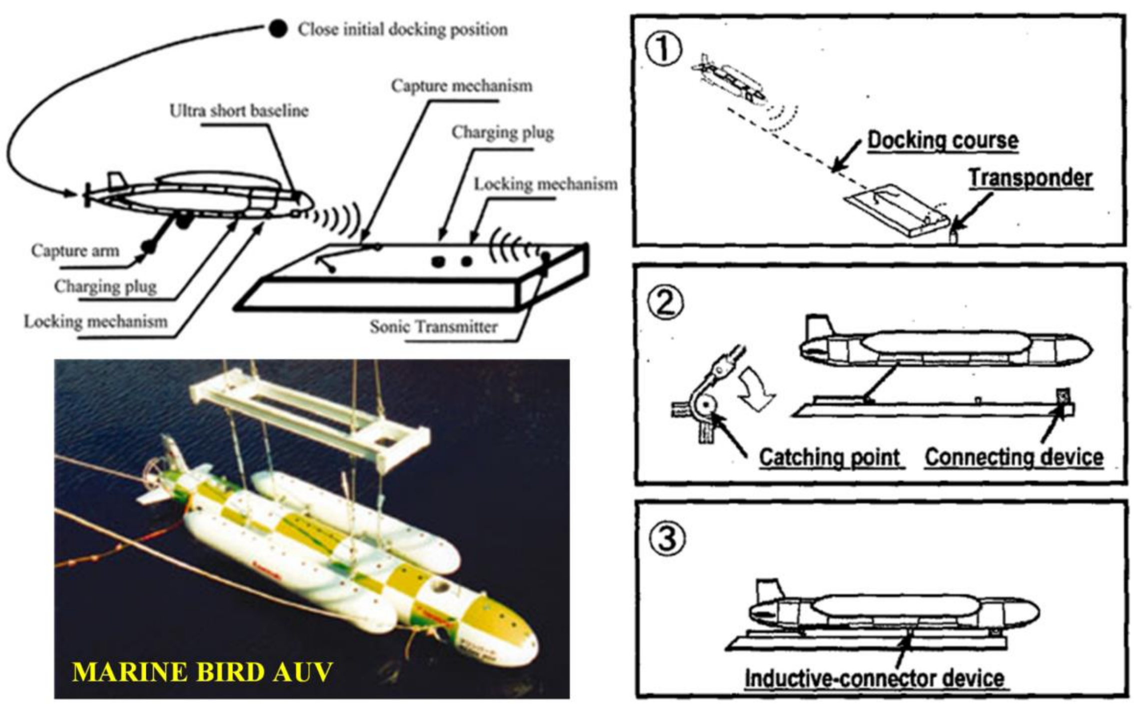

Figure 2-8 MARINE BIRD underwater docking system [89].

Several studies have focused on the landed-type docking system, as illustrated in Figure 2-9. In 2021, Zhejiang University developed an autonomous underwater helicopter (AUH) and a subsea docking station, subsequently conducting sea trials. The AUH is a disc-shaped vehicle, and the docking station is a three-dimensional frame structure with an interior that tapers to an upward-facing opening to accommodate the AUH. The path is adjusted based on real-time sensing information and geographic location [90, 91]. In February 2022, the United Kingdom's Modus Subsea Services achieved autonomous docking of the hybrid autonomous underwater vehicle (HAUV) with a subsea docking station (SDS) [92]. Dong, et al. [93] proposed an omnidirectional docking system and an autonomous charging-oriented docking method for bionic robotic fish, designing and simulating five motion modes using both swimming and gliding techniques.

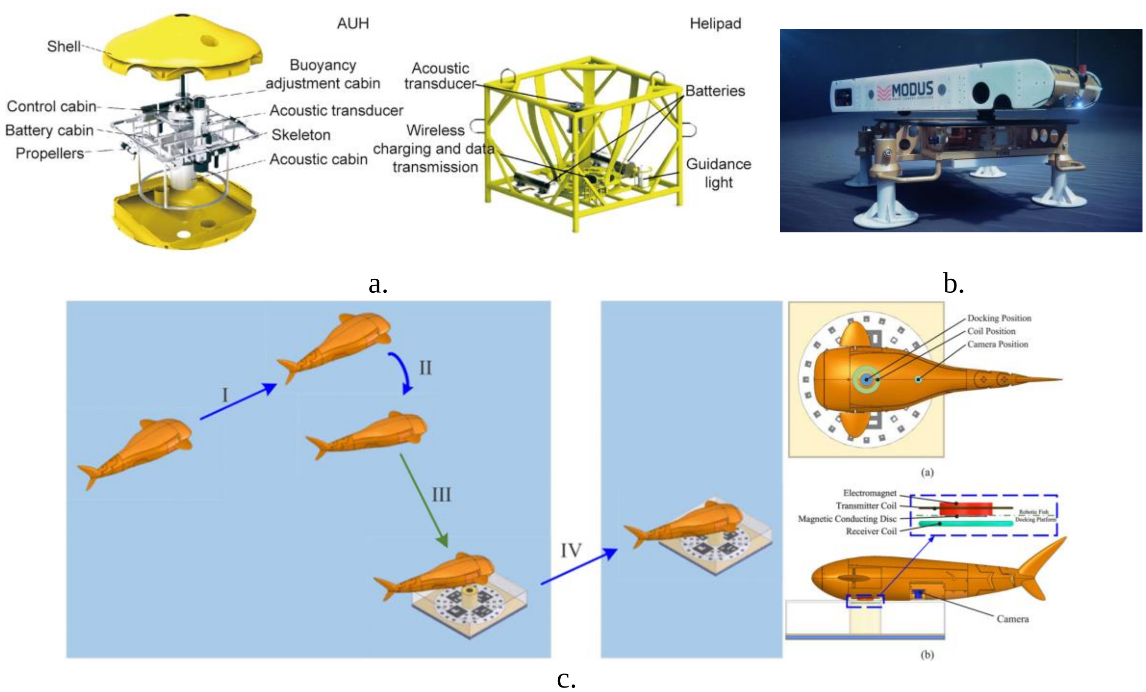

Figure 2-9 a.) AUH and Helipad by Zhejiang University [90, 91] b.) HAUV and SDS by Modus Subsea Services [92] c.) Bionic robotic fish and docking system [93].

2.2.3 Mid-Water recovery: Dynamic Recovery Systems & Manned Underwater Vehicle

a) Dynamic Recovery Systems

Dynamic recovery methods have emerged as is a solution in recent years. Dynamic recovery involves both the AUV and the docking platform being in motion during the recovery process. Compared to the static recovery methods previously introduced, dynamic recovery methods enable the AUV to complete recovery within the operational area. This means recharging, data transfer, and relaunch can be achieved during operation, reducing energy consumption, extending operation time, and expanding the operational area. Additionally, the relative speed between the AUV and the docking station remains low during the docking process, minimizing impact collisions. However, from the perspective of docking feasibility and maturity, static recovery methods are much simpler to execute. Dynamic recovery methods require not only consideration of the AUV's motion but also the motion of the dynamic docking platforms, imposing higher requirements for the AUV's manoeuvrability.

Unmanned Surface Vehicles (USVs) or AUV combined with tapered structures are often used as motherships for dynamic recovery methods. Although USVs cruise on the sea surface, the recovery process occurs underwater. This allows for a more seamless and efficient recovery, reducing the risks associated with surface conditions and enabling continuous operation without the need for the AUV to surface.

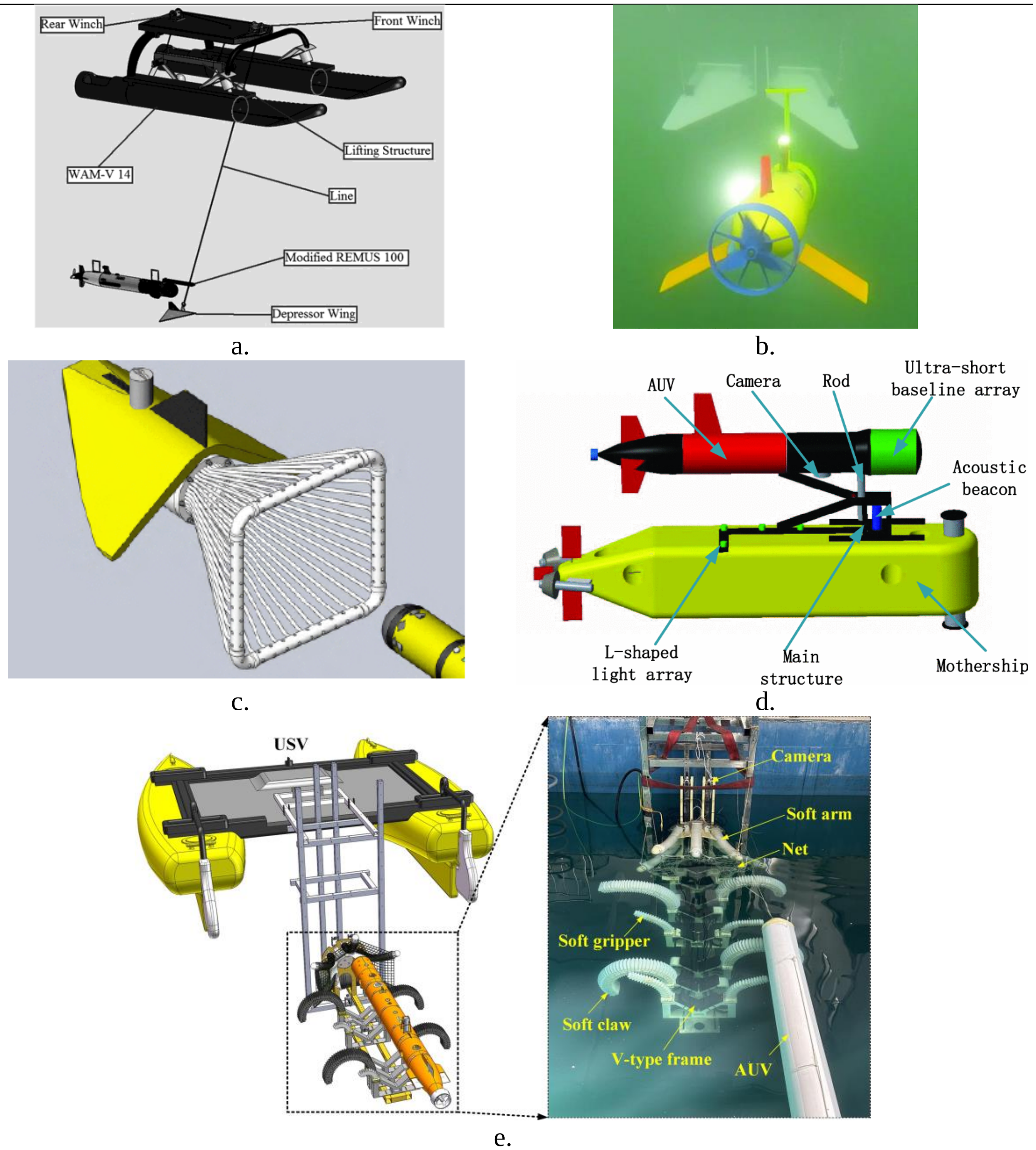

Figure 2-10 a.) b.) e.) AUV docking with USV [26, 94, 95] c.) d.)AUV docking with AUV [96, 97].

As Figure 2-10 shows, In 2012, Hydroid designed a dynamic recovery system with a submerged towed docking cone for REMUS 100 [97]. In 2017, Sarda and Dhanak [26] introduced a concept design for the automated launch and recovery (L&R) of a small autonomous underwater vehicle (AUV) from an unmanned surface vehicle (USV). During the recovery process, the AUV employs a custom pincer-type mechanism to capture a thin line from the USV. In 2019, Purdue University conducted an experimental study on AUV and USV docking and recovery [98]. They designed a novel prototype of a docking station that is streamlined, foldable, and supports multiple torpedo-shaped AUVs. The AUV is equipped with a T-mast docking adapter on top and operates at a speed of 0.5 m/s to 0.6 m/s. The USV operates in both slow (0.2 m/s) and fast (0.4 m/s) modes. In 2020, Yan, et al. [96] performed a simulation study to evaluate the feasibility of dynamic recovery of an AUV by a mobile mothership. Their docking device utilized a fork-carrying pole, and both visual and acoustic guidance systems were employed to assist in the docking process. In 2024, Lin, et al. [95] developed an innovative solution: an in-situ fluid-driven soft dock. During their tests, this system achieved a success rate of 90% with a maximum AUV velocity of 1.6 m/s.

b) Manned Underwater Vehicle

There is a need for some manned underwater vehicles to carry Launch and Recovery Systems (LARS) due to the unique advantages offered by AUVs. Current research on LARS systems for manned underwater vehicles primarily focuses on submarines serving as mother ships. LARS on submarines can be categorized into three main types: internal systems, external systems, and attachment systems. Given the limited information available, a brief description follows [78, 99-101].

The Internal Launch and Recovery System (LARS) of a submarine can be classified into two primary types (Figure 2-11): launching and recovering AUVs using torpedo launch tubes or missile launch tubes. The recovery stage, on the other hand, primarily relies on auxiliary devices such as robotic arms or Remotely Operated Vehicles (ROVs) to assist in recovering the AUV. Using the torpedo launch tube for launching and recovery is relatively easier to retrofit onto existing submarines or incorporate into new ones. However, even with an enlarged torpedo launch tube, t the size of the AUV that can be accommodated is still strictly limited. Similarly, employing missile launch tubes for launching and recovery presents comparable challenges, with the more complex auxiliary recovery devices required. Nevertheless, missile launch tubes, being generally more numerous on submarines, offer the potential to deploy multiple AUVs, forming an array for coordinated missions.

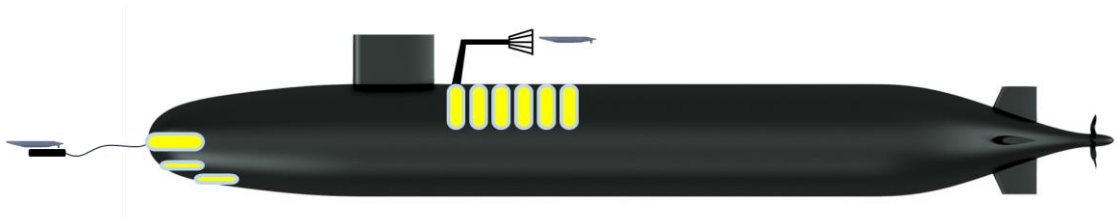

Figure 2-11 Launching and recovering via torpedo launch tubes and missile launch tubes.

__The External Launch and Recovery System (LARS)__ of a submarine also can be classified into two types (Figure 2-12): dry Casing Mounted Hangar (CMH) and wet Casing Mounted Hangar (CMH). The Casing Mounted Hangar (CMH) is a specialized recovery device mounted on a submarine's deck. The dry CMH is an enclosed, pressure-resistant module that connects to the submarine's interior through an airtight passage. During launch or recovery operations, specialized divers typically flood the CMH with seawater and open the hatch to allow the AUV to be guided or autonomously navigate into the chamber. While the dry CMH offers protection from environmental conditions and pressure changes, it has several drawbacks. It is challenging to install on smaller submarines and requires complex systems for drainage, air, and pressure management. In contrast, the wet CMH is an open hangar that remains in direct contact with seawater. The LARS for a wet CMH are similar to those for the dry CMH. However, since there is no passage between the hangar and the submarine, personnel cannot enter the wet CMH for maintenance or assistance. As a result, the wet CMH typically requires a more sophisticated, often automated, LARS. Despite these complexities, the wet CMH is lighter than the dry CMH, making it easier to retrofit and apply to existing submarines.

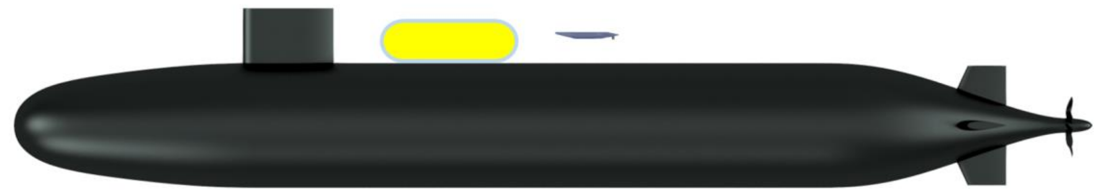

Figure 2-12 Launching and recovering via Casing Mounted Hangar (CMH).

The Attachment Launch and Recovery System (LARS) for submarines is designed to launch and recover AUVs from the side or bottom of a submarine through attachment and separation mechanisms (Figure 2-13). This concept functions like an underwater aircraft carrier. Since the LARS system is semi-embedded in the submarine's hull, it minimizes drag and noise when AUVs are onboard. However, implementing this system poses significant technical challenges, particularly in terms of automation and autonomy, making it more complex to realize.

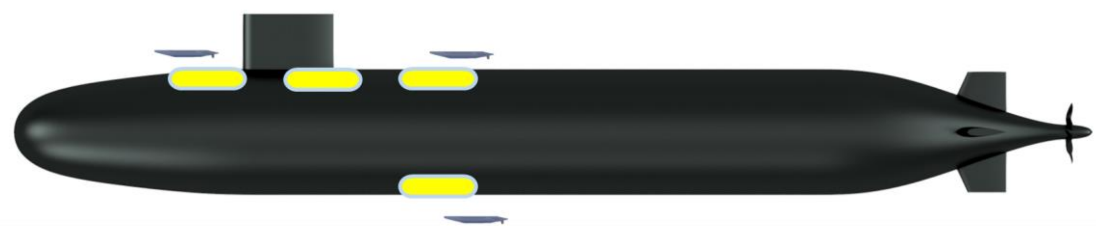

Figure 2-13 Launching and recovering via Attachment Launch and Recovery System (LARS).

To effectively implement the attachment Launch and Recovery System (LARS) for AUVs, a comprehensive understanding of the hydrodynamic interactions between the AUV and the mothership is essential. Previous studies have investigated these interactions, providing insights into how proximity affects the dynamics between the vehicles. Leong, et al. [102] conducted a model-scale study examining the hydrodynamic interaction effects between an AUV and a submarine operating in close proximity. Their findings indicated that the AUV tends to be attracted towards the submarine when near the stern, while it experiences repulsion near the bow. The study also noted minimal interaction effects in the midship region of the submarine, suggesting that the AUV encounters less hydrodynamic interference when positioned along the central body of the submarine. Similarly, Luo, et al. [103] used full-scale numerical simulations to explore these interactions under relatively stationary conditions. Their research confirmed the presence of repulsive and attractive forces acting on the AUV due to the flow field around the submarine's bow and stern, respectively. Importantly, they observed that the AUV's resistance remained relatively unaffected by its distance from the submarine, with the drag remaining nearly constant when the AUV was aligned with the midship region.

Despite these findings, there remains a notable gap in the research concerning the interaction between two underwater vehicles of significantly different sizes, particularly when they are in close proximity under non-stationary conditions. Understanding these dynamics is crucial for optimizing the design and operation of LARS, ensuring safe and efficient recovery processes while minimizing potential risks associated with hydrodynamic forces. This calls for further investigation into the complex interactions that occur during dynamic manoeuvres, which could greatly enhance the operational reliability and efficiency of AUV recovery systems.

2.2.4 Summary

The recovery of Autonomous Underwater Vehicles (AUVs) is a critical aspect of their operational lifecycle, presenting unique challenges across various environments. This section has explored the primary methods of AUV recovery: surface, seabed, and mid-water, each offering distinct advantages and challenges based on their operational context.

Surface recovery remains the most traditional and widely used method, relying on shipboard techniques that demand significant human expertise and specialized equipment. While effective, surface recovery is often constrained by weather conditions and requires careful coordination to ensure the safe retrieval of AUVs.

Seabed recovery methods involve fixed underwater docking stations, offering robust solutions for energy replenishment and data transfer. These systems—capture-type, guided-type, and landed-type—are well-suited for stable environments, providing AUVs with secure docking and protection from dynamic water conditions. However, these systems require the prior deployment of docking stations and a thorough understanding of the operational area. This implies that the docking stations must be strategically positioned based on detailed knowledge of the seabed and environmental conditions.

Mid-water recovery methods, including dynamic recovery systems and manned underwater vehicle approaches, have emerged as innovative solutions to enhance operational flexibility. Dynamic recovery allows for on-the-fly recharging and data transfer, significantly extending the operational range and time. Although technically challenging, it minimizes relative speeds and impact collisions during the docking process, offering a seamless integration of recovery operations within the AUV's mission profile. The integration of Launch and Recovery Systems (LARS) with manned underwater vehicles, particularly submarines, highlights a sophisticated approach to AUV deployment and retrieval. Internal, external, and attachment systems provide varied strategies for embedding AUV operations within larger underwater missions, each requiring advanced automation and autonomy to overcome the technical complexities involved. While there is a growing need for dynamic LARS to support these manned vehicles, significant challenges remain.

Overall, the development of AUV recovery systems continues to be a pivotal research area, with each method presenting specific trade-offs between operational efficiency, technical complexity, and environmental adaptability. Future advancements in AUV technology and recovery methodologies promise to enhance the reliability and effectiveness of underwater missions, enabling more complex and longer-duration operations in challenging environments. However, there is currently limited research available on dynamic recovery systems for the submarine. One of the key challenges in this area is understanding the interactions between two underwater vehicles of vastly different sizes, especially during the approach and final docking stages. At full scale, the fluid dynamics and hydrodynamic forces between the two vehicles become complex, particularly when they are in close proximity. These interactions can significantly affect the stability and safety of the docking process, making this an important focus for future studies. Addressing these challenges will be crucial for advancing dynamic recovery systems, allowing for more efficient and safe recovery operations in increasingly diverse and unpredictable underwater environments.

2.3 Biomimetic Applications Inspired by Remora Fishes

Based on the review of AUVs and their recovery systems, it is clear that the field of Autonomous Underwater Vehicle (AUV) recovery is rapidly advancing, yet significant challenges persist, especially for dynamic recovery in mid-water environments. A promising direction for overcoming these challenges is the exploration of biomimetic technologies inspired by natural systems. Among the numerous biological models, the remora fish stands out due to its unique adaptations for attachment and interaction with larger marine animals. This section introduces remora fish and discusses the biomimetic research inspired by them.

Natural cooperative relationships have evolved over time, exemplified by the remora fish (e.g., *Echeneis neucratoides*), sometimes referred to as "suckerfish." These fish are known for their tendency to attach to hosts rather than swimming independently, as depicted in Figure 2-14. Despite their poor swimming abilities, remoras can travel long distances by "hitchhiking" on various marine creatures, including sharks, turtles, and even man-made marine vehicles. The remora's remarkable attachment ability is attributed to its specialized suction disk, illustrated in Figure 2-15. This organ is an oval-shaped, sucker-like structure with slat-like formations that create suction, reinforced by numerous parallel pectinated lamellae that enhance adhesion to the host's surface [104].

Additionally, the soft lip around the rim of the suction disk allows for a perfect fit on various attachment surfaces, further improving the suction [105]. Dolphins often attempt to dislodge remora fish by leaping out of the water, spinning in the air, and using centrifugal and water impact forces [106]. However, this does not occur with sharks, where the remora remains mostly undisturbed.

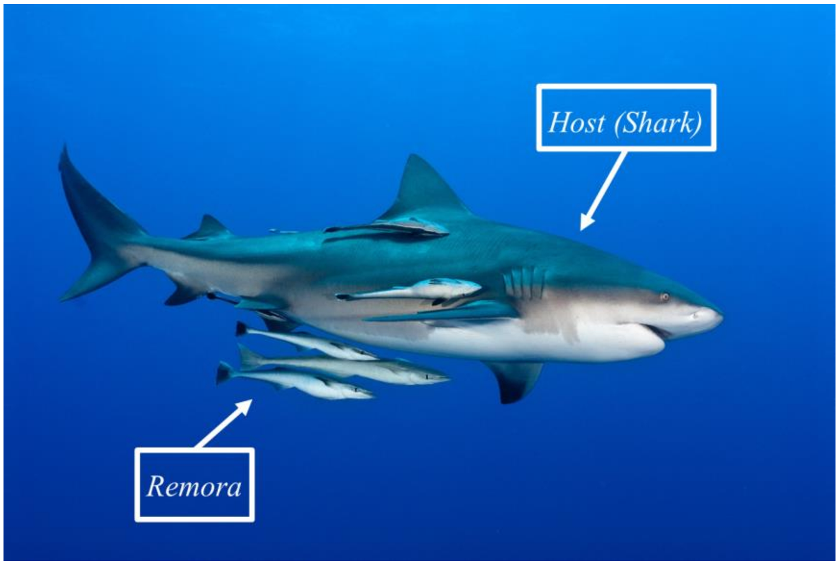

Figure 2-14 The attached swimming of remora with the host [107].

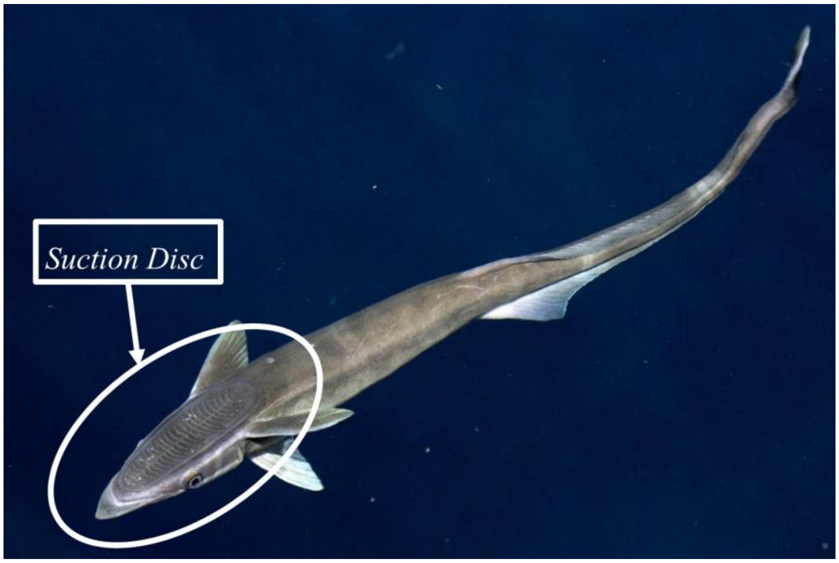

Figure 2-15 The suction disc of the remora [108].

Research on remora fishes and their biomimetic applications began early, focusing initially on their unique attachment mechanisms. Over time, our understanding of these fascinating creatures has deepened. Most current research emphasizes the mechanics of the remora’s suction disk, with less focus on their attachment locations and hydrodynamic characteristics.

The remora fish, with its high fineness ratio, is well-adapted for hitchhiking on host surfaces rather than free-stream swimming [35]. Remarkably, remoras can remember their previous attachment spots via touch receptors in their suction disks [109, 110]. Their attachment sites are not chosen randomly. For instance, Brunnschweiler, J.M. [34] found that nearly 40% of the attachments (137 out of 345) occurred near the belly of sharks, 27% on the back, and the fewest on the caudal fin. This has attracted researchers to study the reasons for such behaviour.

Marine biology research suggests that remoras may prefer attachment locations that minimize irritation to the host [36]. They also tend to choose areas with minimal motion and deformation during the host’s swimming to ensure a stable attachment platform [35]. Flammang, et al. [37] s observed that remoras often attach to areas on whales with lower hydrodynamic resistance, which helps reduce their energy expenditure. Despite these insights, the hydrodynamic advantages of specific attachment sites remain underexplored. Based on the study conducted by Brunnschweiler, 2006, it seems like the remora fish have learnt to seek for areas with adverse pressure gradients and developed boundary layers. Therefore, whether the remora fish selects its attachment location based on hydrodynamic criteria still needs to be investigated.

In terms of biomimetic applications, the remora's sucker mechanism and living habits have inspired various technological innovations. Wang, et al. [111] developed a robot featuring a biomimetic remora disc capable of attaching to different surfaces and generating significant pull-off forces, up to 340 times the weight of the disc prototype. Lee, et al. [112] s investigated a reversible PDMS adhesive inspired by the remora’s suction disk, which demonstrates utility in various wet conditions.

Jia, et al. [113] introduced the Remora Optimization Algorithm (ROA), a novel bionics-based, nature-inspired, and meta-heuristic algorithm designed to solve complex optimization problems.

The exploration of biomimetic applications inspired by remora fishes has revealed valuable insights into designing advanced technologies. Remora fishes, with their distinctive "hitchhiking" behavior and specialized suction disks, offer a compelling model for developing innovative solutions for dynamic underwater operations. Current research has predominantly focused on the mechanical properties of the remora's suction disk and less on the hydrodynamic implications of attachment site selection. However, further investigation is needed to fully understand whether remoras choose their attachment sites based on specific hydrodynamic criteria, such as adverse pressure gradients and boundary layers. Therefore, the distinctive behaviours of remora fish are utilized as inspiration for this study of an underwater AUV dynamic recovery system, where another large underwater vehicle acts as a mother ship for the recovery system.

2.4 Concluding Remarks

Chapter 2 has provided a comprehensive literature review on the current state of Autonomous Underwater Vehicles (AUVs) and their recovery systems, along with an exploration of biomimetic applications inspired by remora fishes. The insights gathered from this chapter highlight both the advancements and the ongoing challenges within these areas, setting the stage for the research focus of this thesis.

In Section 2.1, we explored the background and primary types of AUVs, underscoring their critical role in marine research and operations. AUVs offer a unique combination of versatility and adaptability, making them indispensable tools across various marine environments and tasks. While biomimetic AUVs may require certain compromises in performance due to specialized designs, their targeted capabilities offer unparalleled advantages for specific applications. This section establishes the necessity for adapting AUV designs, particularly their hydrodynamic shapes, to accommodate dynamic recovery systems, drawing inspiration from natural models.

Section 2.2 focused on the recovery methodologies of AUVs, categorizing them into surface, seabed, and mid-water recovery approaches. Each method was examined for its operational benefits and limitations. Mid-water recovery methods, particularly dynamic recovery systems for the manned underwater vehicle, are emerging as flexible solutions that can extend the operational capabilities of AUVs by allowing real-time data transfer and recharging. However, the attachment Launch and Recovery System (LARS) for AUVs presents a significant research gap, specifically regarding the hydrodynamic interactions between significantly different-sized vehicles operating in close proximity under non-stationary conditions.

Section 2.3 introduced the remora fishes, highlighting their unique "hitchhiking" behaviors facilitated by specialized suction disks. These natural adaptations provide a rich source of inspiration for developing biomimetic solutions in underwater vehicle recovery. While much research has been conducted on the mechanical aspects of remora adhesion, there remains a notable gap in understanding the hydrodynamic benefits of specific attachment locations. Addressing this knowledge gap could open up new possibilities for designing AUV dynamic recovery systems inspired by remora fishes, potentially improving their efficiency and reliability.

To address these gaps, this study will explore several key questions in the forthcoming chapters:

1. *Boundary Layer Effects*: What are the effects of the developed boundary layer flow on the remora's hydrodynamic characteristics?
2. *Attachment Hydrodynamics*: How do popular attachment locations on the surface of sharks affect the hydrodynamics of remoras?
3. *Biomimetic Improvement*: How is the improvement of the hydrodynamics performances of the AUV inspired by remora fishes?

4. *AUV-Specific Attachment:* What impact do various attachment locations on the submarine surface have on a remora-inspired AUV?
5. *Optimal Recovery Location:* Which location is more advantageous as a recovery area for the remora-inspired AUV?
6. *Velocity Influence*: How does the forward velocity of the submarine influence the effect of the low-velocity region on the remora-inspired AUV?
7. *Proximity Effects*: What is the impact on the AUV when it comes into close proximity with underwater vehicles of significantly different sizes?
8. *Docking Process Stages*: What are the stages of the docking process when the AUV approaches a submarine?

Chapter 3

Hydrodynamic Characteristics of Remora Fish

As delineated in the preceding chapter, a systematic investigation is conducted to understand the remora's swimming strategy in their attachment state from a hydrodynamic point of view. This foundational understanding lays the groundwork for exploring the feasibility of dynamically docking a remora-inspired AUV to a submerged mother vehicle.

Within this framework, based on existing literature, a general remora fish model and a shark model as the host are established. Subsequently, the simulations in this study are divided into three cases, which are: 1) the free-swimming case, 2) the flat plate boundary layer case and 3) the host attachment case. By comparing and analysing those simulations, the effects of the developed boundary layer flow and the adverse pressure gradient on the remora's hydrodynamic characteristics are investigated.

Section 3.1 introduces the models of the remora and shark, which are used in following sections. Additionally, the free-swimming case primarily serves as a reference to benchmark and understand the individual hydrodynamic performance of both the remora and the shark. Section 3.2 focused on the flat plate boundary layer case, aiming to investigate the relationship between the remora drag and key variables such as boundary layer thickness, incoming flow velocity, and associated Reynolds number. Then, Section 3.3 explored the attachment location, revealing the combined effects of the boundary layer flow and pressure gradient. Finally, the concluding remarks presented in Section 3.4.

3.1 Remora and Shark Free-Swimming Analyses

Numerical simulations were conducted using the CFD software STAR-CCM+ to explore the hydrodynamic free-swim behaviours of both the remora and the shark, establishing our benchmark cases. The oceanic whitetip shark typically maintains an average speed ranging between 1.2kn to 1.4kn, with recorded peak speeds reaching up to 8.9kn [114]. Given that the remora attaches itself to the shark, it moves at the same speeds as its host. Hence, for this study, the velocities assigned to the remora varied between 1kn to 8kn. The simulations in this chapter assumed both the remora and the shark as rigid bodies. This assumption is justified by the fact that during attachment, the remora's body remains mostly still, with minimal motion apart from its suction disc. Furthermore, the remora-inspired AUV, which is the focus of later research, is based on a traditional AUV design that features a rigid body. Similarly, the submarine model used in the simulations is rigid as well. Thus, the assumption of rigidity in this study aligns with the characteristics of both the natural remora-shark system during attachment and the dynamic recovery systems being developed. Throughout the simulation process, drag characteristics were meticulously calculated. The subsequent sections detail the methodology employed in these computations.

3.1.1 Numerical Methodology

A Reynolds-Averaged Navier–Stokes (RANS) model along with a K-ω Shear Stress Transport (K-ω SST) turbulence model which has been extensively utilised in industrial applications [115, 116] is employed in following studies. The K-ω SST turbulence model offers the benefits of both the standard K-ω turbulence model and K-ε turbulence model. It utilizes the K-ω formulation in the inner parts of the boundary layer to capture complex flow phenomena. Conversely, the K-ε formulation can be applied in regions away from the wall, where the turbulence properties have lower sensitivity [117].

a) Geometry Preparation

The section below describes the details of the simulated models for the remora fish and the shark model. The models were created based on the natural shape and sizes of the actual remora and shark but adapted to be suitable for CFD simulation, and rigid models were used.

The model of the remora fish is designed based on the natural characteristics and key dimensions of the remora found in the Puerto Rico sea region. Literature indicates that remoras in this area typically range in length from 51 to 73 cm. Therefore, for this study, a model length of 65 cm, representing an average size, was chosen [118]. It is to note that when a remora attaches to its host, all four of its pectoral fins open, with two remaining close to the host. This behaviour has been accurately represented in the simulation. Additionally, when the remora's suction disc attaches to a surface, its body assumes an inclined position of approximately 5 degrees. Interestingly, we note that when the remoras swim on their own, their suction discs face upwards. For subsequent simulations, it is essential to retain critical hydrodynamic features, such as the pectoral fins, while simplifying elements that have minimal hydrodynamic impact. Based on the above principles, a 3D remora model has been developed for subsequent CFD simulations. The foundational parameters of this remora model, along with its 3D CAD representation, are depicted in Figure 3-1.

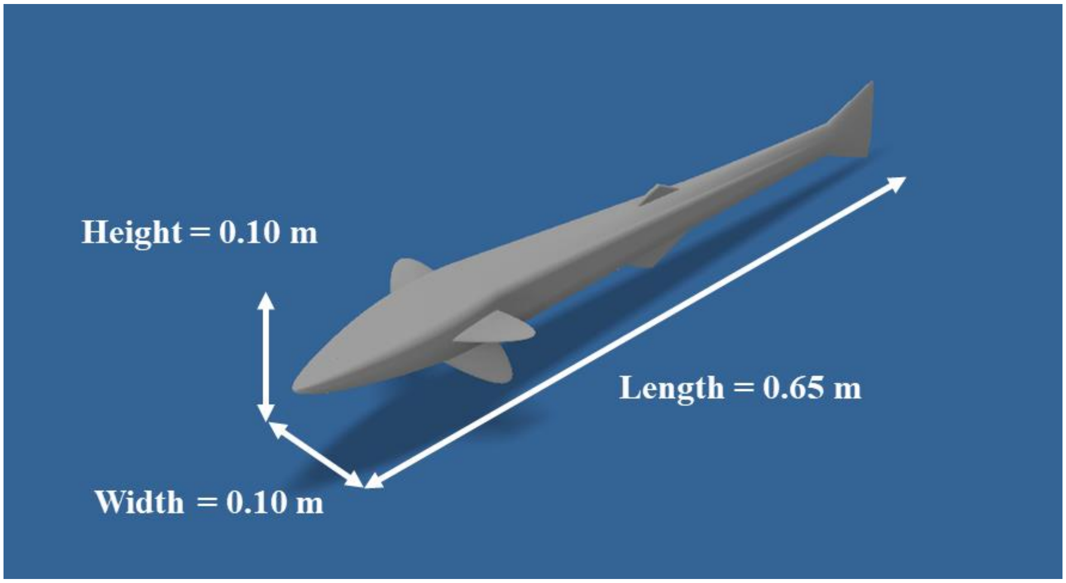

Figure 3-1 The 3D remora fish model.

The oceanic whitetip shark, which swims also in the Puerto Rican area [119], was selected with an average length of 2m [120]. Similarly to the remora model, the original shark model is simplified for the CFD simulation. Figure 3-2 shows the basic parameters of the shark model.

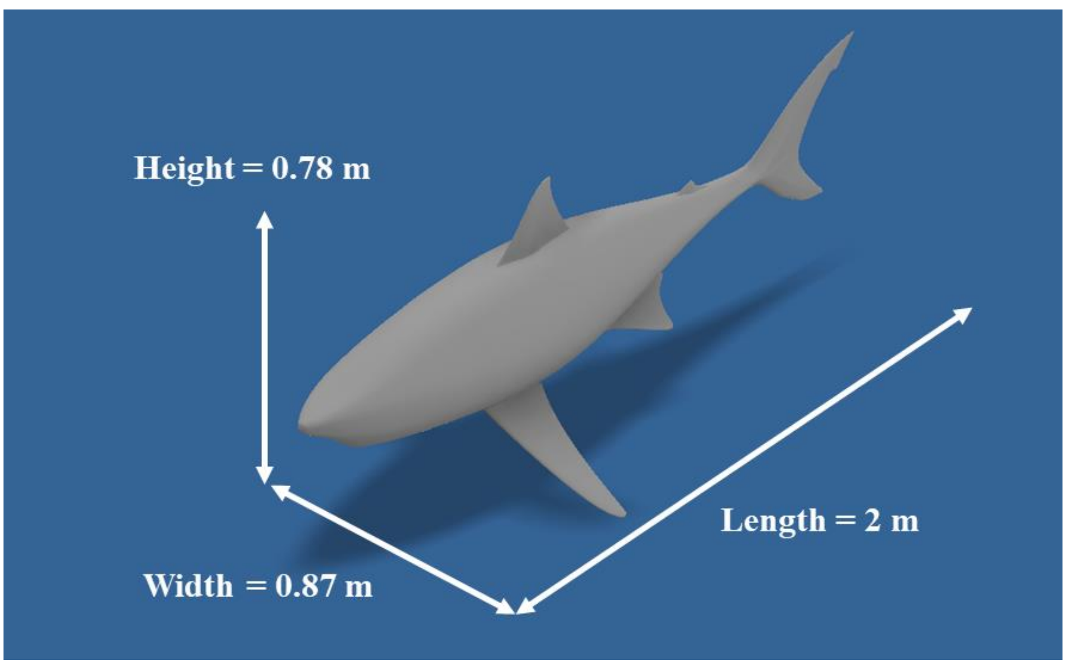

Figure 3-2 The 3D shark model.

b) Computational Domain

The computational domain utilized in this study is depicted as a cuboid, as illustrated in Figure 3-3. According to ITTC Practical Guidelines for Ship CFD Applications guidelines [121], the inlet and exterior boundary should be located 1-2L away from the model, and outlet has to be placed 3-5L downstream. Therefore, in this simulation, symmetry boundary conditions are established on the surrounding planes, positioned at a distance of 1.5L from the model's body. Both the shark and remora models are subjected to non-slip wall conditions. For the fluid flow, the inlet is defined as the velocity inlet and positioned 5L upstream from the model. Conversely, the outlet is positioned 5L downstream and set as a pressure outlet. As a validation measure, the outlet was further extended by threefold. Analysis indicated that this extension had a negligible impact on the computed drag. To ensure that the width of the channel was adequate, the blockage ratios were computed, with the highest 0.33% appearing in the shark free-swimming condition which deems to be very low.

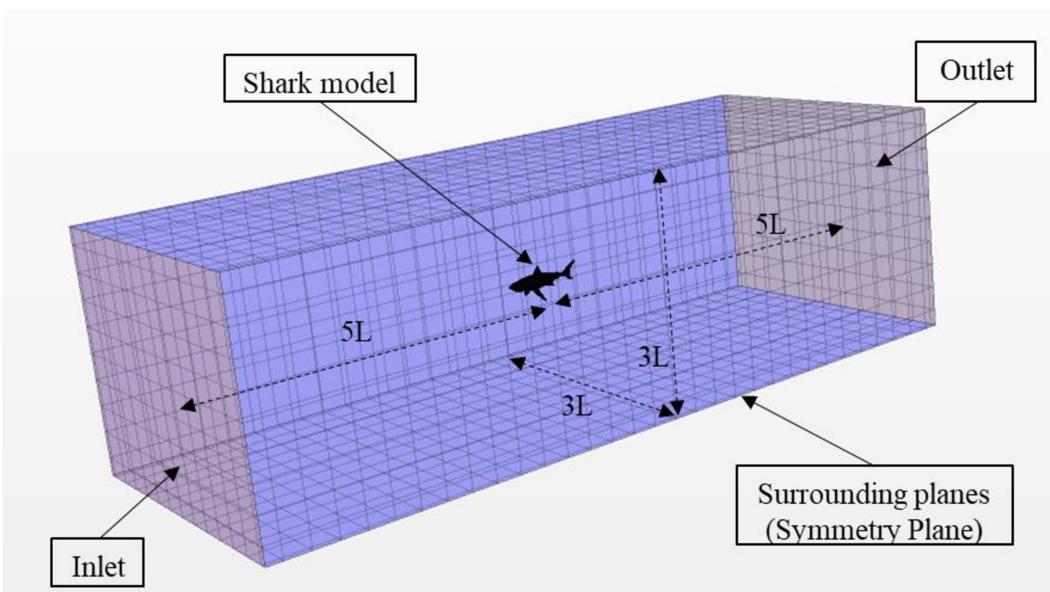

Figure 3-3 Domain and boundary conditions of the free-swimming simulation.

c) Mesh Generation

The mesh generation process employed an automatic meshing tool equipped with volumetric control. For wall treatment within the simulation, the 'all y+' setting in STAR-CCM+ was adopted. This hybrid method incorporates a high-y+ treatment (y+ > 30) for coarser meshes and a low-y+ treatment (y+ < 1) for finer meshes[116]. Specifically, a refined grid, approximately 0.1L in proximity to the models, was utilized. It is noted that this refinement was consistently applied across all tested cases (free swimming, flat plate and attached) as illustrated in Figure 3-4, Figure 3-5, Figure 3-13 and Figure 3-22, respectively. Furthermore, the height of the initial cell near the wall was meticulously controlled to maintain a y+ value less than 5 [116, 122-124]. Overall, the simulation employed approximately 3.4 million cells. Detailed mesh configurations for both simulations can be found in Figure 3-4 and Figure 3-5.

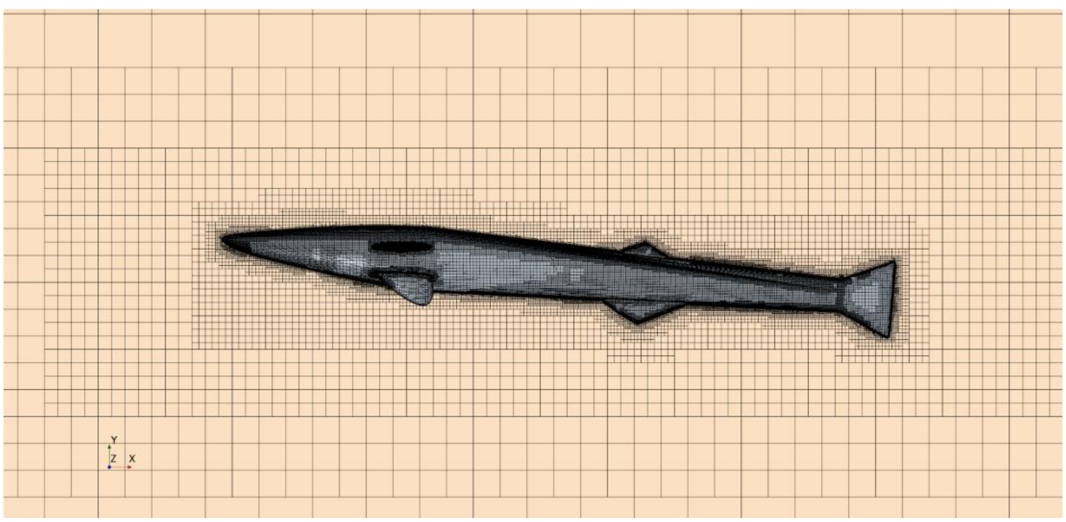

Figure 3-4 Mesh view for free-swimming remora simulations.

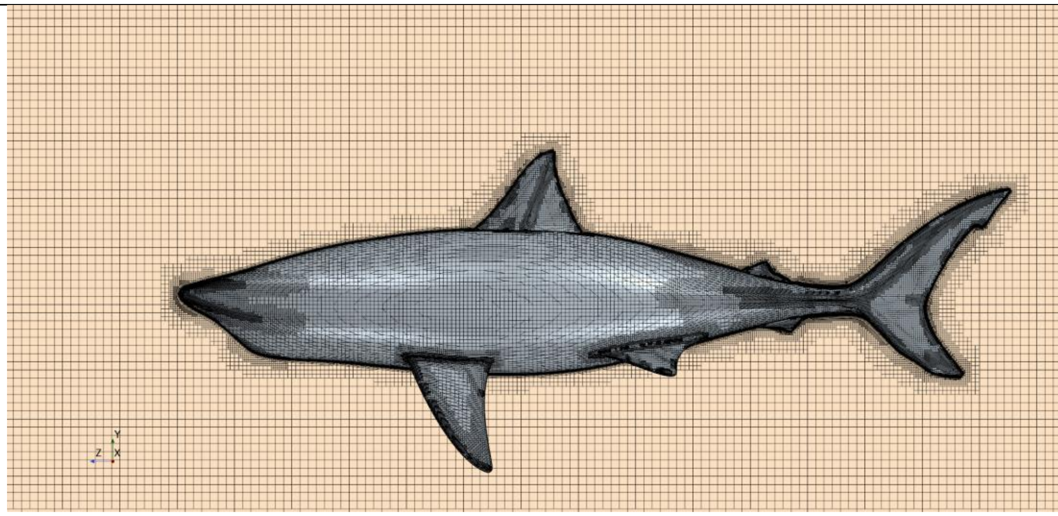

Figure 3-5 Mesh view for free-swimming shark simulations.

A grid independence study was conducted to verify the accuracy of the numerical simulation [125, 126]. There are three different grid configurations to be implemented in the CFD software STAR-CCM+ namely: coarse, medium, and fine grid. Utilizing a grid refinement ratio of R = √2, the free-swimming remora simulation at a speed of 1 kn served as the basis for this investigation. The cell numbers of the three grids increased from 1.6 million cells for the coarse case to 8.4 million cells for the fine case, as outlined in Table 3-1. The numerical uncertainty values for the drag force are about 2.26%. Therefore, considering the computational cost, the medium grid will be used in the subsequent analysis.

Table 3-1 Grid independence study-remora.

Parameter	
Fine Grid	8446216
Medium Grid	3724865
Coarse Grid	1634396
Resistance-Find Grid	0.107N
Resistance-Medium Grid	0.110N
Resistance-Coarse Grid	0.117N
GCI_{fine}	2.26 %

d) Validation Analysis

Since no direct validation data is available for the rigid remora and shark resistance, a resistance analysis using a benchmark submarine model was conducted to validate the CFD simulation methodology. The experimental data for the model-scale DARPA Suboff AFF-0 submarine (without appendages) resistance was provided by Liu and Huang [127], a with the key parameters of the model shown in Figure 3-6.

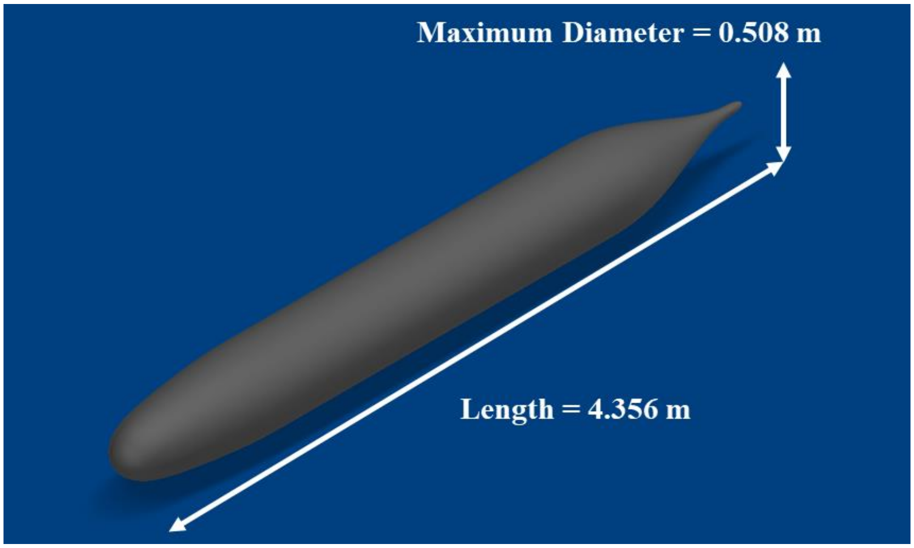

Figure 3-6 The 3D DARPA Suboff AFF-0 submarine model.

For this resistance simulation, the numerical simulation settings, including the domain size and mesh generator, were kept consistent with the previous sections. The inflow velocities used in the simulations ranged from 3.045 m/s to 9.254 m/s, matching the velocities used in the experimental data. Figure 3-7 illustrates a good correlation between the numerical and experimental results, with differences ranging from -3.45% to 0.87%. This validates the accuracy of the CFD simulation approach used in the analysis.

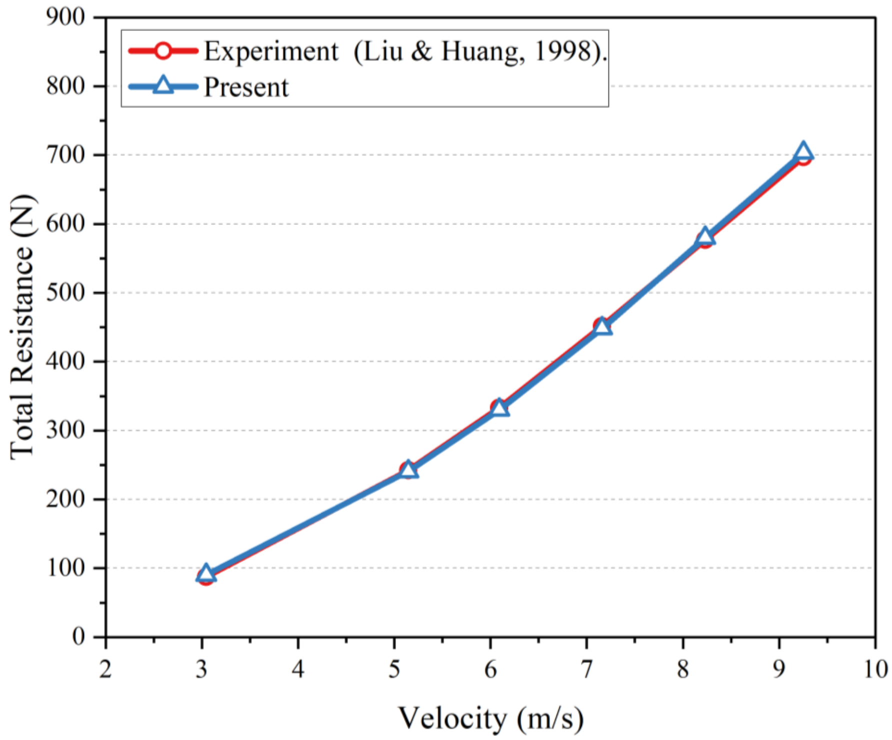

Figure 3-7 The comparison of the model-scale DARPA Suboff AFF-0 submarine resistances between the numerical and experimental results.

3.1.2 Hydrodynamic Performance of Free-Swimming Remoras and Sharks

This section shows the drag results of the remora and the shark in free-swimming conditions at different velocities. Nondimensional numbers are used to compare the resistance performance. The Reynolds number, Re, is calculated with following equation 3-1:

$$Re = \frac{\rho * L * V}{\mu}, \qquad 3\text{-}1$$

where, ρ is the density of the water, 997kg/m^3; L is the reference length, m; V is the incoming velocity, m/s; μ is the dynamic viscosity of water, 0.001kg/(m*s).

And the drag coefficient, C_D, is calculated with following equation 3-2:

$$C_D = \frac{F}{\frac{1}{2} * \rho * V^2 * A}, \qquad 3\text{-}2$$

where, F is the drag force, N; A is the reference frontal area of the model (width * height, m^2).

The simulation results are presented in Figure 3-8, whilst the associated drag coefficients are shown in Figure 3-9. The table illustrates that, at a given velocity, the remora fish exhibits a considerably lower Reynolds number compared to the shark, owing to their differing body lengths. However, under the same Reynolds number as shown in Figure 3-9, the drag coefficient of the remora is much higher than the one of the sharks, and in terms of absolute drag, the remora's drag is quite low due to its smaller size. Therefore, in its free-swimming mode, the remora fish does not show any competitive drag performance. In fact, the remora has a non-streamlined body compared to the highly streamlined body of the shark body. The remora’s body is designed for attachment rather than fast swimming, with a flat suction pad on top of the head. This feature, while crucial for attachment, increases frictional resistance and form drag, especially when the remora is free-swimming. The flat top surface and the specialized suction disc, which increases the frontal area exposed to the water, further contribute to this higher drag coefficient. This unique body shape creates more turbulence and inefficient flow around the body when it is swimming on its own, compared to more streamlined fish like sharks, whose body shapes are optimized for minimizing drag during fast swimming. Therefore, while the remora has low absolute drag due to its size, its drag coefficient is high due to the trade-offs in body design favouring attachment efficiency over swimming efficiency. Additionally, we also observe in Figure 3-9, that at 4 knots (Reynolds number of 4.5 x 10^6), the shark resistance characteristics indicate laminar to turbulent transition, due to a peak in the drag coefficient. At the investigated is velocity range (up to Reynolds number of 1.3 x 10^6), flow transition is not observed on the remora, indicating fully turbulent flow around the remora.

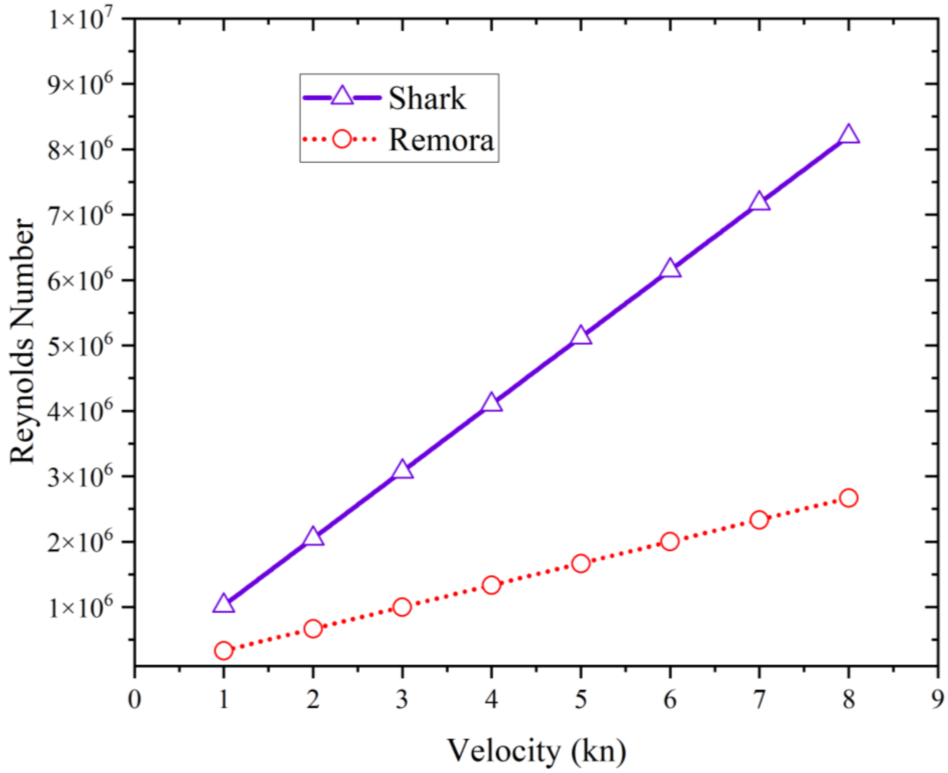

Figure 3-8 Velocity vs. Reynolds numbers of remora and shark in free swimming.

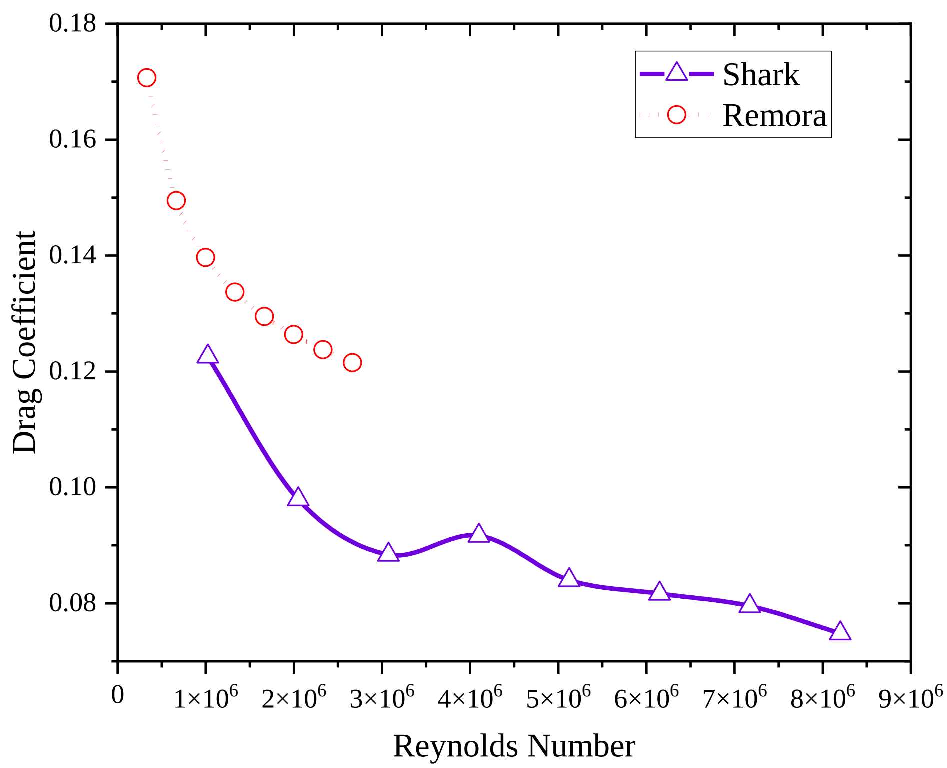

Figure 3-9 Drag coefficients vs. Reynolds numbers of remora and shark in free swimming.

To further investigate the hydrodynamic characteristics of both remora and shark in free-swimming states, velocity and pressure contours were analysed. While the contours across different velocities exhibited similarities, those for the 8kn inflow velocities for both the remora and shark are specifically showcased in Figure 3-10 and Figure 3-11. It is worthy noticing that as shown in Figure 3-11 due to the bulky build of the whitetip shark, adverse pressure gradient regions with low flow velocity develop gradually after the belly and the back regions. This hints the hydrodynamic reasons why the remora prefers to attach to those locations rather than to the pectoral fins.

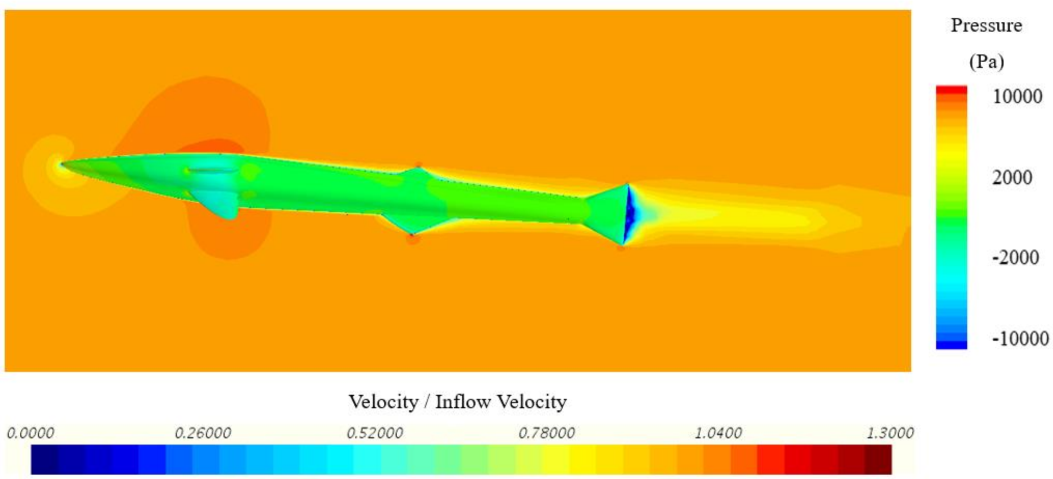

Figure 3-10 Velocity and pressure contours of the remora fish in free-swimming condition (Pressure contour displayed on the surface of model, and velocity contours displayed on the section plane).

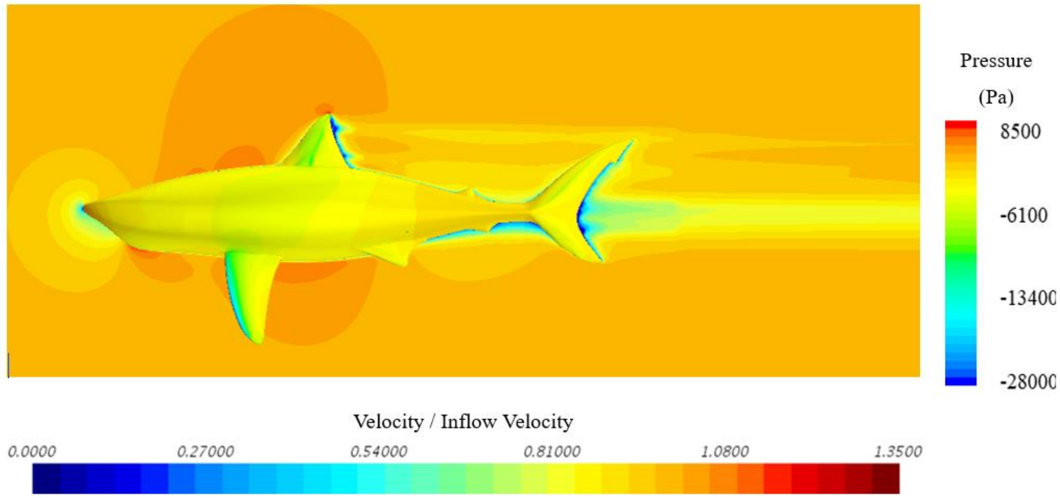

Figure 3-11 Velocity and pressure contours of the shark in free-swimming condition (Pressure contour displayed on the surface of model, and velocity contours displayed on the section plane).

3.2 Remora-Flat Plate Attachment analysis

Once the free-swimming conditions of both remora and shark have been evaluated, this section focuses on investigating the hydrodynamic impact of the boundary layer flow on the remora fish swimming performance. To investigate this question, a fundamental approach of a boundary layer flow over a flat plate has been used. We demonstrate this in the following section.

3.2.1 Systematic Approach to Introduce the Boundary Layer Flow

In this section, we set to investigate firstly, the effect of the boundary layer thickness in the drag reduction rate of the remora. Secondly, we attempt to develop a relationship between the average velocity of a boundary layer profile to the drag reduction on the remora. These two points will help in future design problems where fast design computations could be required. To address the first point, we systematically vary the flow velocity and the remora's attachment location to a flat plate.

This will provide us with a relationship that computes the drag reduction rate to the boundary layer height in which the remora is swimming. To address the second point, we estimate first a drag reduction rate based on the average velocity of the boundary layer and compare this estimation to the drag reduction rate computed with the simulations.

By defining a reference frame at the leading-edge and at the centre of a flat plate, with the x-axis oriented in the streamwise direction, the transition point $x_{c,}$ is the x- coordinate where laminar to turbulent transition occurs. This transition point $x_{c,}$ is estimated using equation 3-3 and the results are shown in Table 3-2.

$$x_c = \frac{Re * \mu}{\rho * V} \tag{3-3}$$

Table 3-2 Estimated transition point with varying flow velocity.

V, kn	x_c, m
1	0.097
2	0.049
3	0.032
4	0.024

Four different locations downstream from the leading edge and along the flat plate (10m, 20m, 30m and 40m) are chosen to perform the systematic simulation. They are all in the turbulent flow regime, as indicated by x_c in Table 3-2. Therefore, a turbulent boundary layer flow is expected and to estimate the boundary layer thickness δ, equation 3-4 is used. In the 3-4, L, is the distance between the attachment location and the leading edge of the flat plate [128].

$$\delta = \frac{0.37 * L}{Re^{\frac{1}{5}}} \tag{3-4}$$

It can be seen in Table 3-3 that with the varying velocities and the attachment locations, the developed boundary layer thickness varies. We note that the ratio between the boundary layer thickness and the height of the remora fish (δ/H) ranges from 127.58% to 510%, and that slower velocities provide thicker boundary layers.

Table 3-3 Thickness of flat-plate boundary layer.

L, m	V, kn	δ, m	H, m
10	1	0.168	168.35%
	2	0.147	146.55%
	3	0.135	135.14%
	4	0.128	127.58%
20	1	0.293	293.11%
	2	0.255	255.16%
	3	0.235	235.29%
	4	0.222	222.13%
30	1	0.405	405.41%
	2	0.353	352.93%
	3	0.325	325.44%
	4	0.307	307.25%
40	1	0.510	510.33%
	2	0.444	444.27%
	3	0.410	409.66%
	4	0.387	386.76%

3.2.2 Numerical Methodology

Building on the prior analysis, this section focuses on simulating the remora swimming within the varying boundary layer thicknesses previously determined. The objective is to obtain the drag on the remora when subjected to the effects of a flat plate boundary layer flow. A comprehensive set of 16 simulations was executed. These simulations varied the remora's attachment points downstream from the flat plate's leading edge—specifically at distances of 10m, 20m, 30m, and 40m. Moreover, the simulations encompassed four different velocities: 1kn, 2kn, 3kn, and 4kn. The definition of the simulation cases is shown in Table 3-4.

Table 3-4 The definition of simulation cases.

Case	1-1	1-2	1-3	1-4	2-1	2-2	2-3	2-4
Velocity	1kn	2kn	3kn	4kn	1kn	2kn	3kn	4kn
Distances	10m	10m	10m	10m	20m	20m	20m	20m
Case	3-1	3-2	3-3	3-4	4-1	4-2	4-3	4-4
Velocity	1kn	2kn	3kn	4kn	1kn	2kn	3kn	4kn
Distances	30m	30m	30m	30m	40m	40m	40m	40m

In this case, the computational domain adopts a cuboid domain, with the specific boundary conditions delineated in Figure 3-12. The pressure outlet boundary is positioned 4L downstream of the remora model. The upstream boundary is defined as velocity inlet, with its positioning varying—specifically set at distances of 10m, 20m, 30m, and 40m upstream from the remora fish (see Figure 3-12a). This variation is instrumental in introducing different the boundary layer thicknesses. The remora model and the flat plate are set as non-slip wall conditions. The height of the domain is 2L and the distance between the two side planes is 2L. The top and sides planes are specified as symmetry planes. The boundary conditions and the full length of the flat plate are shown in Figure 3-12b. In the figure, the velocity inlet boundary is at 10 m and the remora is attached to the bottom plane.

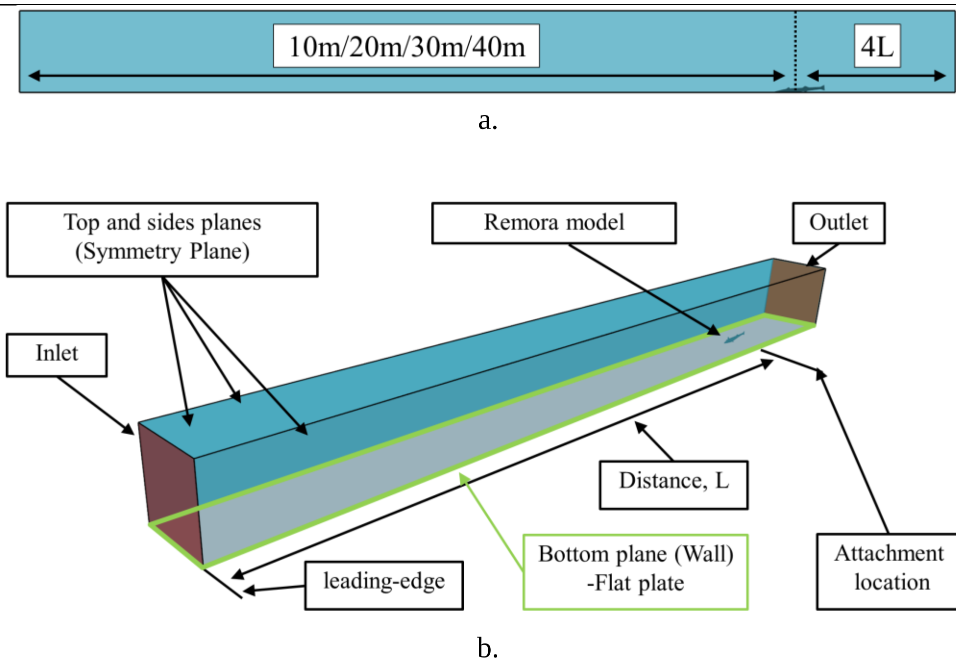

Figure 3-12 Domain and boundary conditions of the flat plate simulation, a) side view and b) three-dimensional view of the domain.

The size of the domain was defined according to the ITTC Practical Guidelines for Ship CFD Applications [121]. The surrounding boundaries are located between 1 to 2 full lengths away from the model. The blockage ratio is very low as well, 0.25% in this simulation. The downstream boundary is positioned 4 full lengths away from the model and it was also elongated 3 times to verify the results, which showed a negligible effect on the computed drag.

The mesh of the remora model is generated by the trimmer mesh in STAR-CCM+. As shown in Figure 3-13, volumetric refinement has been applied in the vicinity of the remora fish. Meanwhile, to capture the boundary layer development of the bottom plane, 80 layers of prism mesh are used on the bottom plane. We note that the y+ is kept below 5 in all of the simulations, and for the generation of boundary layer flows, in the flat plate y+ is below 1.

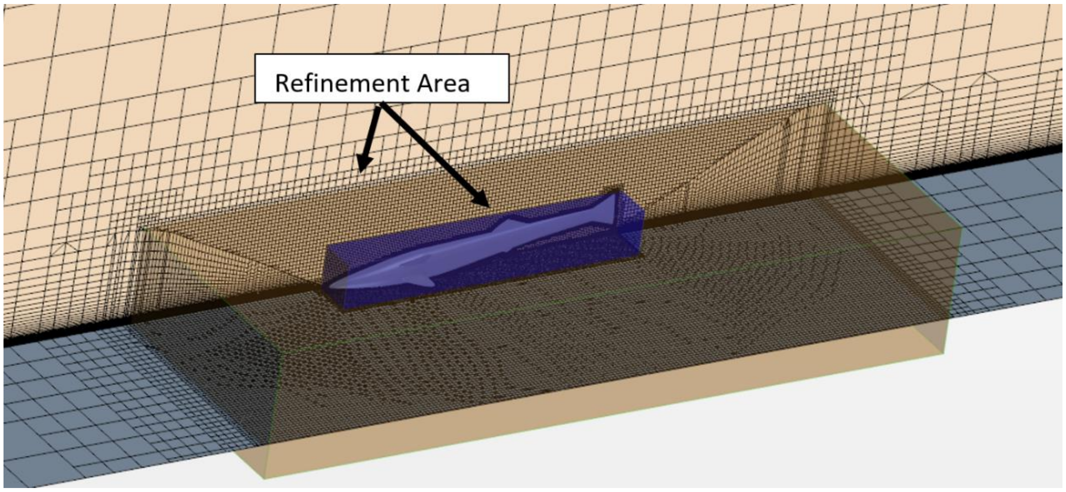

Figure 3-13 The mesh around the remora fish when attached onto the flat plate.

3.2.3 Effect of the Developed Boundary Layer on Remora Fish Swimming

With the above setup, the drag characteristics can be achieved over varying boundary layer thicknesses. As indicated in Figure 3-14, it can be seen that when the remora fish is swimming in the boundary layer a drag reduction can be achieved, ranging between 27% to 42%. This drag reduction shows direct relationship with the boundary layer thickness which is maximum at the lowest speed (V=1kn) with the longest distance (L=40 m). Therefore, from a drag reduction point of view, the remora fish tends to choose areas with a developed boundary layer to minimise the resistance on its body.

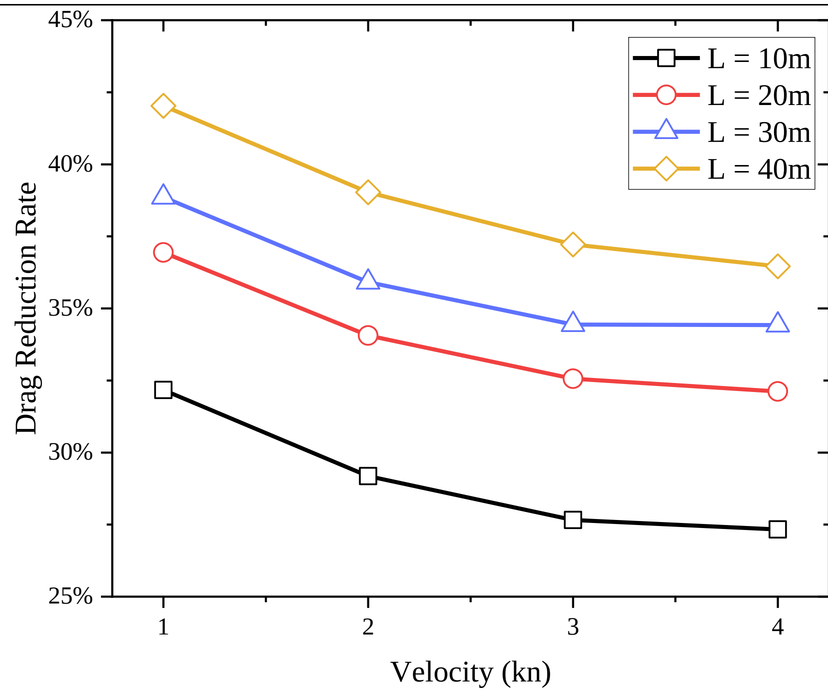

Figure 3-14 The drag reduction rate vs. the incoming velocity as attached on different locations from the leading edge of the flat plate.

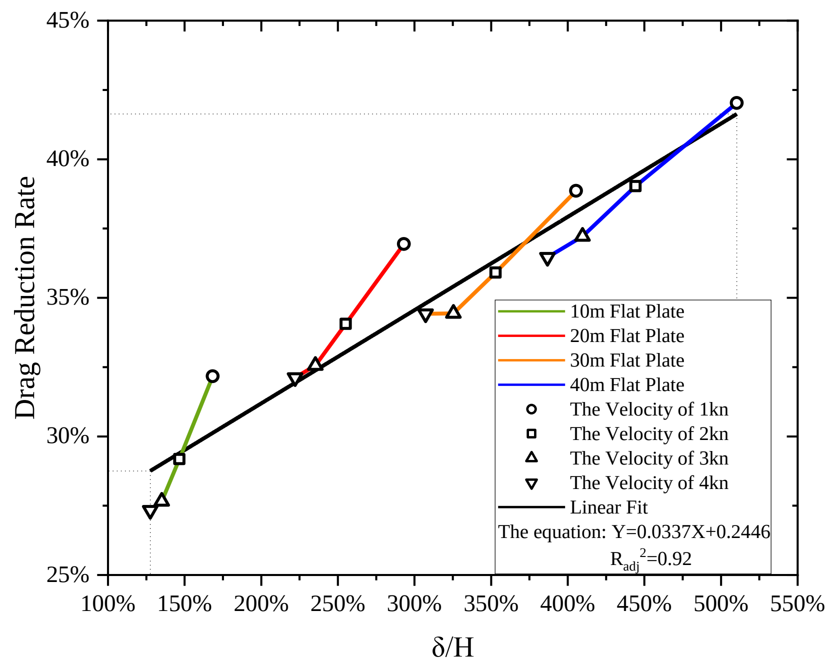

Figure 3-15 Linear fitting for the drag reduction rate versus boundary layer thickness to remora height ratio.

Figure 3-15 shows the drag reduction rate (D_r) versus δ/H. The relationship is roughly linear. Hence the drag reduction rate can be estimated with the following equation 3-5:

$$D_r = 0.0337\frac{\delta}{H} + 0.2446 \tag{3-5}$$

We utilised the adjusted coefficient of determination (${R_{adj}}^2$) as an indicator to measure the linearity of the data. A high value indicates a linear relationship. The adjusted coefficient of determination ${R_{adj}}^2$ restrains the effect of the number of independent variables and its definition is given by:

$${R_{adj}}^2 = 1 - (1 - R^2)\frac{n-1}{n-p-1} \tag{3-6}$$

where R is the coefficient of determination, n is the sample size, and p is the number of independent variables. Here, we computed ${R_{adj}}^2$ to be 0.92.

On the other hand, as shown in Figure 3-16, the velocity distribution and pressure contours are summarised and it can be seen that the boundary layer thickness increases with increasing L and decreases with increasing V. For a detailed comparison, Figure 3-17 shows a summary of the boundary layer profiles of the tested cases at the different flow velocities. From this figure, the average velocity of the boundary layer within the height of remora (H) can be extracted. By averaging the flow velocity of the boundary layers ($V_{average}$) and considering the incoming velocity upstream of the remora ($V_{incoming}$), the estimated drag reduction rate (D_r^e) is shown below in equation 3-7:

$$D_r^e = \frac{v_{average}^2 - v_{incoming}^2}{v_{incoming}^2} \tag{3-7}$$

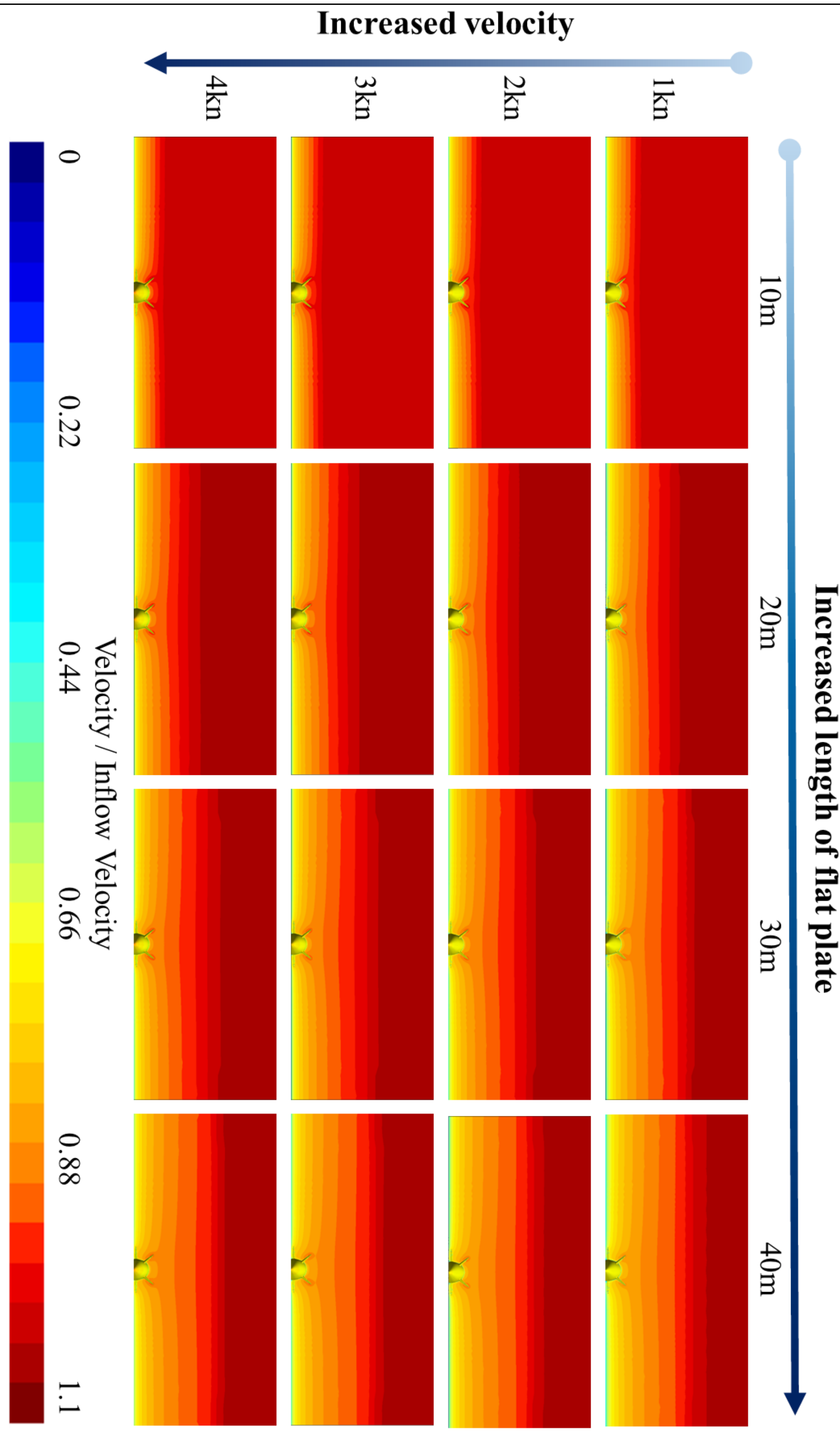

Figure 3-16 The velocity contour on the cross section.

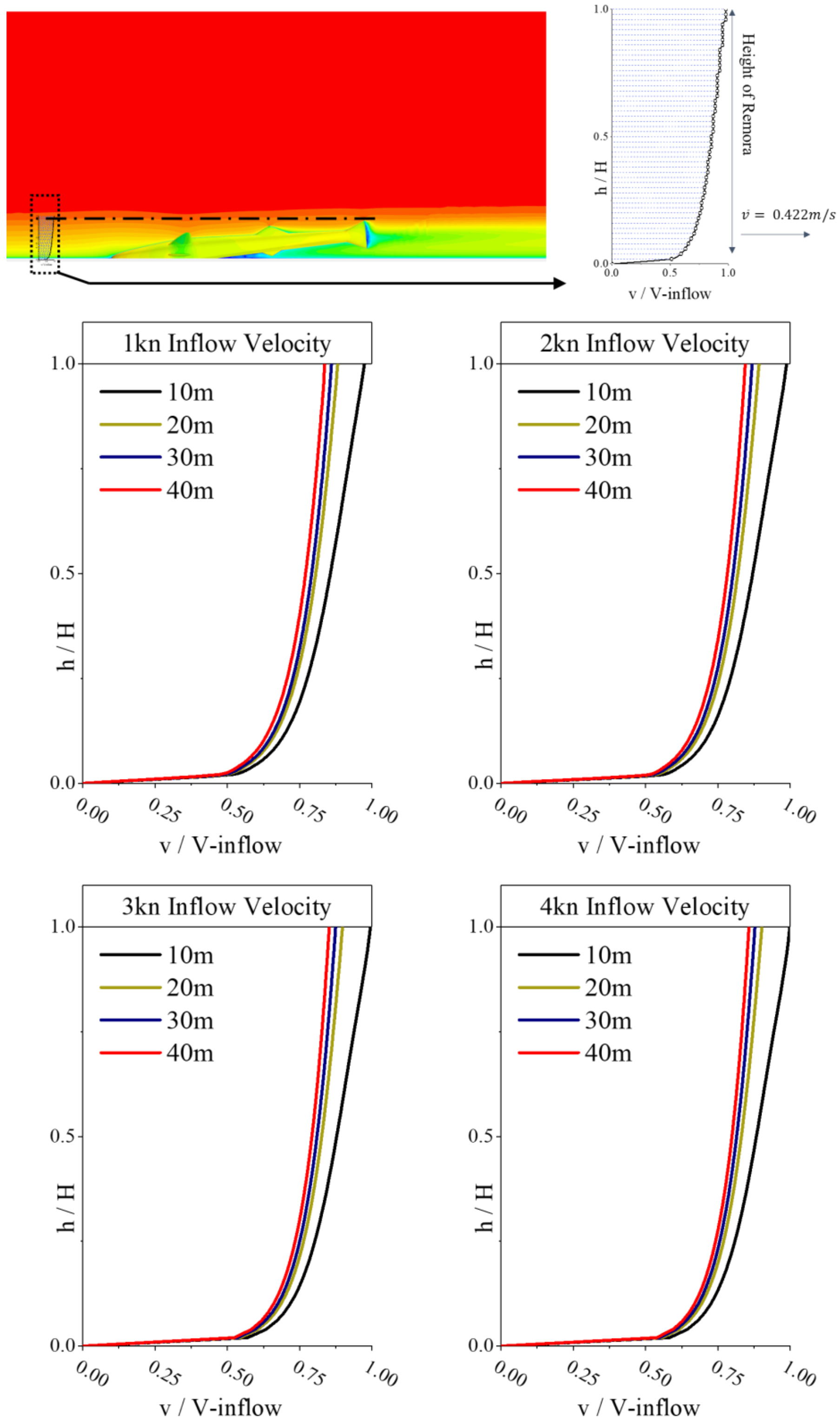

Figure 3-17 Summary of the velocity distributions in boundary layer at different velocities within the height of the remora (H).

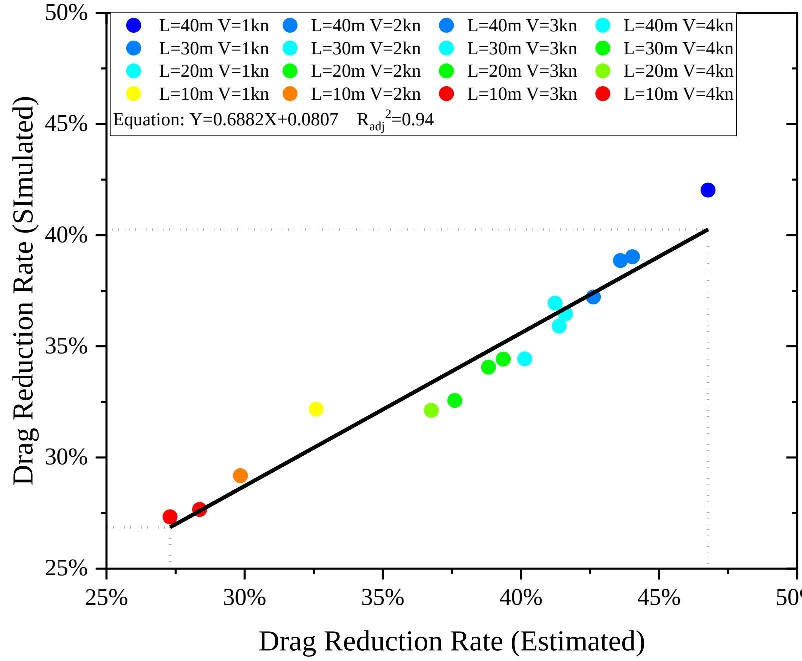

Figure 3-18 The linear fitting equation for the drag reduction rate between the simulated one and the estimated one using the average velocity.

As shown in Figure 3-18, a linear relationship between the simulated drag reduction rate and the estimated one using the average velocity can be derived with the following 3-8 with ${R_{adj}}^2$=0.94:

$$Y = 0.6882X + 0.0807 \tag{3-8}$$

3-8 is derived from the linear relationship of Figure 3-18. In the figure, *X* is the estimated drag reduction rate, which is computed by 3-7, while *Y* is the drag reduction rate resulting from our simulations. We believe that 3-5 and 3-8 are helpful as a reference to estimate the drag reduction rate in the boundary layer for future designs.

A cross validation is presented versus the law of the wall of the flat plate boundary layer. Through the results of the flat plate boundary layer simulation, the relationship between dimensionless velocity, u^+, and wall coordinate, y^+, can be extracted and compared with the law of the wall of the flat plate boundary layer. Moreover, the dimensionless velocity, u^+, and wall coordinate, y^+, can be calculated by the following 3-9, 3-10 and 3-11[129]:

$$u_\tau = \sqrt{\frac{\tau_w}{\rho}}, \tag{3-9}$$

$$y^+ = \frac{y * u_\tau}{v}, \tag{3-10}$$

$$u^+ = \frac{u}{u_\tau}, \tag{3-11}$$

Where, u_τ is the friction velocity, m/s; τ_w is the wall shear stress, Pa; ρ is the density of the water; y is the distance from the wall, m; v, is the kinematic viscosity, m^2/s; u is the velocity, m/s.

The results are plotted in Figure 3-19. The simulation results show good agreement with the law of the wall of the flat plate boundary layer.

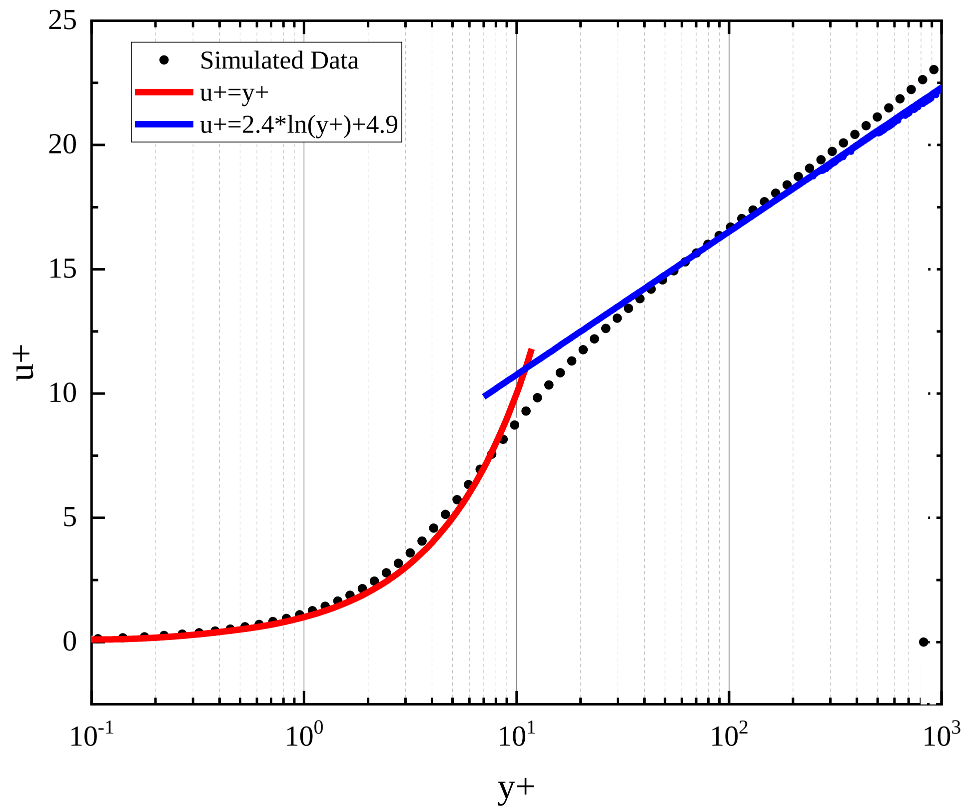

Figure 3-19 Dimensionless velocity, u+, vs. wall coordinate, y+.

3.3 Remora-Shark Attachment Analysis

Based on the previous section, it is found that taking the advantage of the developed boundary layer the drag experienced by the remora fish is significantly reduced. The following section explores the effect of the attachment locations of the remora fish on the body of the shark.

3.3.1 Numerical Methodology

Brunnschweiler [34] conducted a study examining the attachment positions of remoras on blacktip sharks over 345 sequences (Figure 3-20). The study identified three favourable attachment locations: the belly, the back, and the pectoral fin. These locations were further investigated in this study. The models were developed to simulate the remora attached to the shark at each of these positions, as depicted in Figure 3-21.

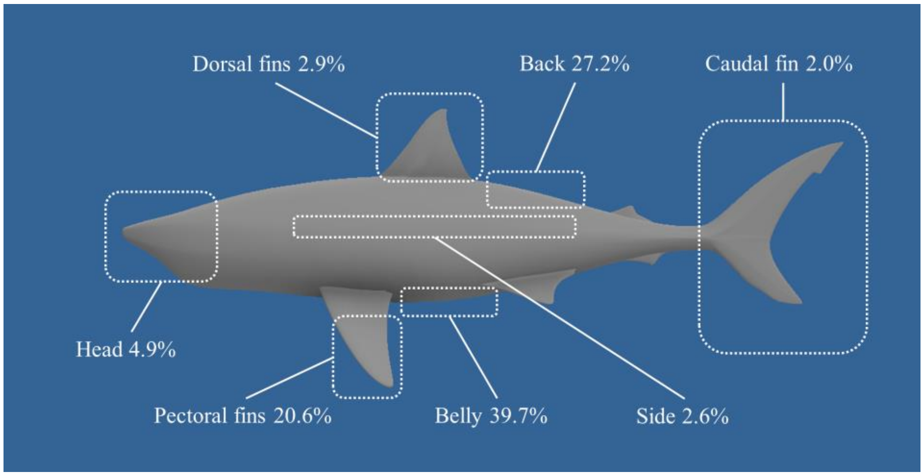

Figure 3-20 The probability of remora attachment to the shark surface at various locations.

The boundary conditions of the computational domain and mesh setup for the belly, back and pectoral fin attachment cases, are specified in the same manner as those of Section 3.1. Nine different speeds are examined. First, speeds over the range between 1 to 8 knots, in intervals of 1knot, and then, the average speed of oceanic whitetip shark (1.3 knots). The mesh details and refinement areas, which are designed to capture the complex flow dynamics around the attachment sites accurately, are shown in Figure 3-22.

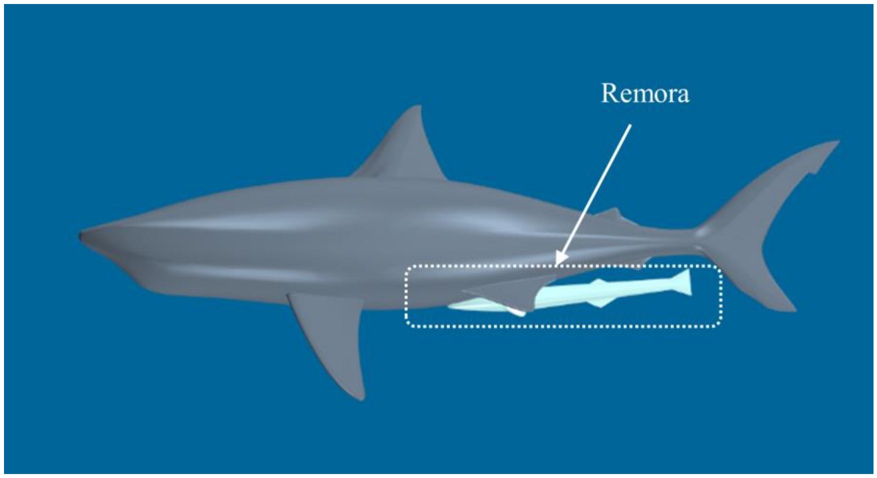

a. Attached on the belly location

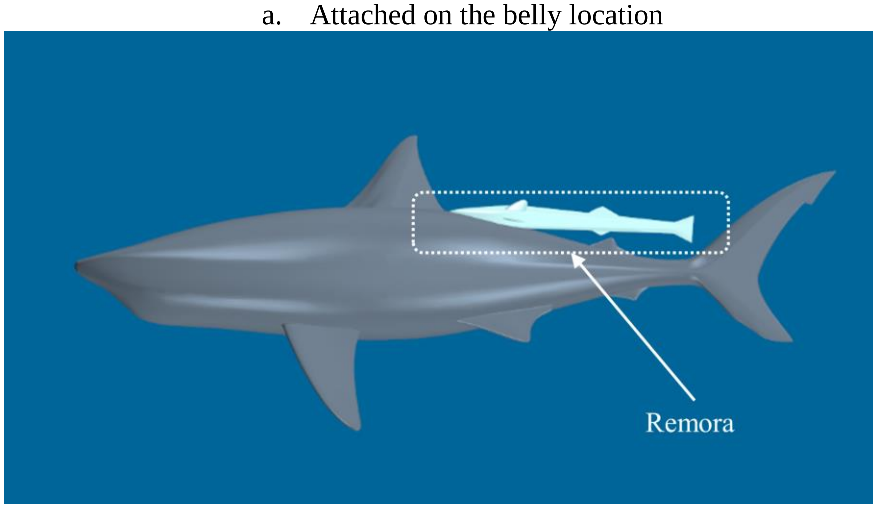

b. Attached on the back location

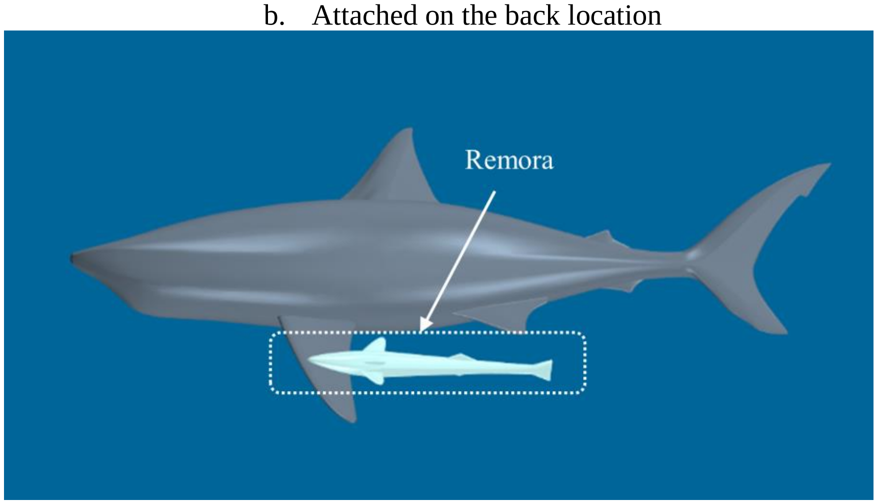

c. Attached on the pectoral fin location

Figure 3-21 Attachment locations of the remora fish in the a) belly, b) back and c) pectoral fin of the shark.

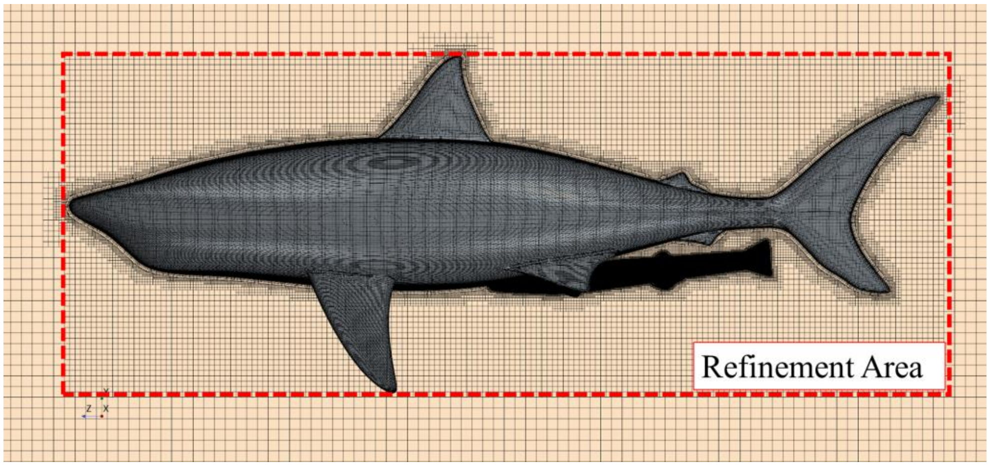

a. Mesh scene for the belly location

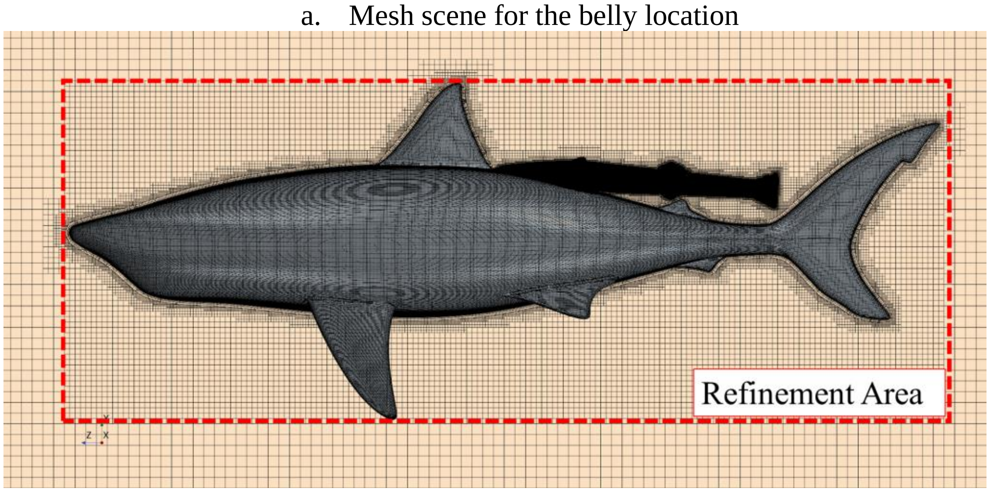

b. Mesh scene for the back location

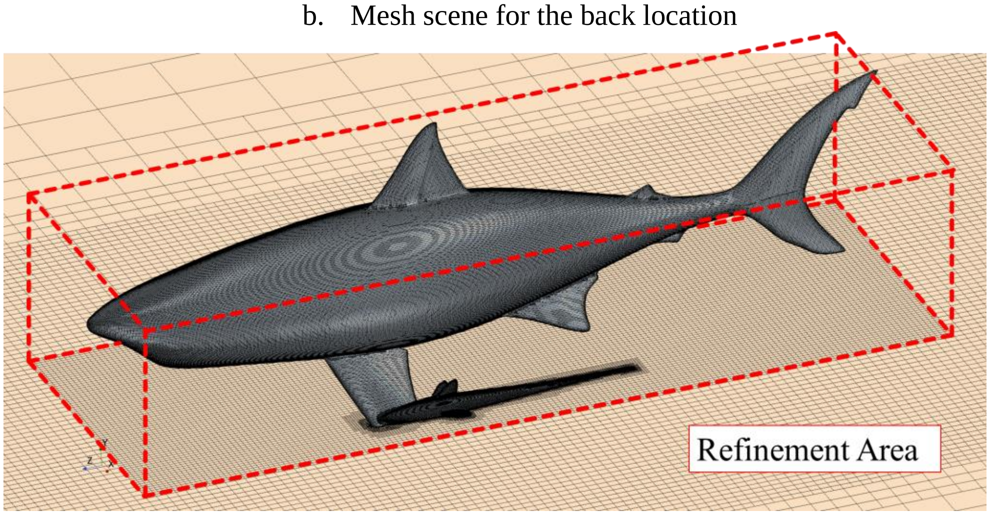

c. Mesh scene for the pectoral fin location

Figure 3-22 Different meshing scenarios with the remora fish attached to the shark a) at the belly, b) at the back and c) at the pectora fin.

3.3.2 Effect of Attachment Locations on Remora Fish Swimming

The drag characteristics of the remora when attached to different locations of the shark are computed. By comparing the results to the equivalent free-swimming conditions, the drag reduction rate for the remora, and the drag increase rate for the shark are determined.

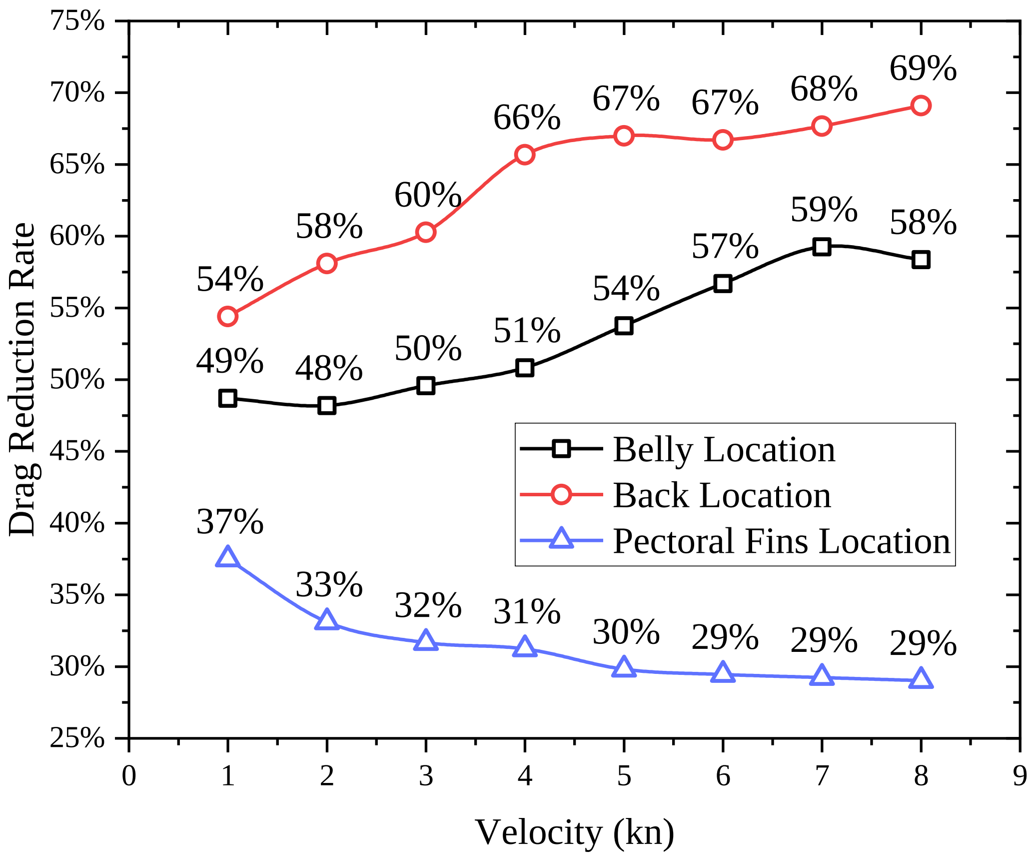

Figure 3-23 The rate of the drag reduction in a range of velocities when the remora attached on different locations.

Figure 3-23 presents the trends of the drag reduction rate of the remora when attached to different locations. It can be noted that for the belly and the back locations, the drag reduction rates of the remora increase with the rise of the velocity, from 49% to 59% and 54% to 69% respectively. On the contrary, for the pectoral fins location, the drag reduction rate decreases from 37% to 29% with increasing velocity, and the drag reduction rate seems to converge towards a constant value after 4kn. In summary, the belly attached case, and the back attached case have higher rate of drag reduction, with the back attached case showing the highest reduction.

The drag components of the remora, pressure drag and shear drag, are shown in Figure 3-24 and Figure 3-25, for the free-swimming condition and the different attachment locations versus different velocities. With increasing velocity, the trends of the shear drag are similar for all four conditions. Regarding to the pressure drag, the free-swimming and pectoral fins-attachment conditions have a similar trend. On the contrary, for the belly and back attachment conditions the pressure drag points to the opposite direction and provide a drag reduction for the remora due to the adverse pressure gradient. It should be noted that at the back location there is a dorsal fin in front of remora and the adverse pressure gradient region appears to be built up behind the dorsal fin, therefore the pressure force become negative pointing opposite to the direction of the shear drag and results in the maximum drag reduction for the remora. Similarly, when the remora attaches to the belly of the shark, the incoming flow is largely blocked by the shark body, and after 4kn the forward thrust provided by pressure force increases. Whereas, when attached onto the pectoral fin, the remora is exposed to the incoming flow, hence creating the lowest drag reduction rate.

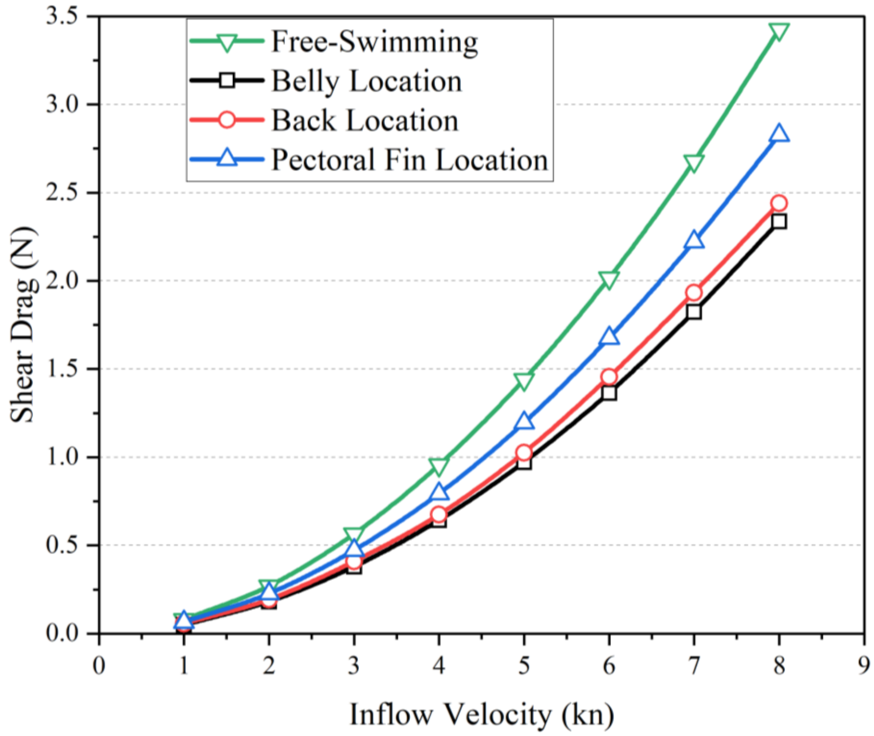

Figure 3-24 Comparations of the pressure forces for remora in different conditions.

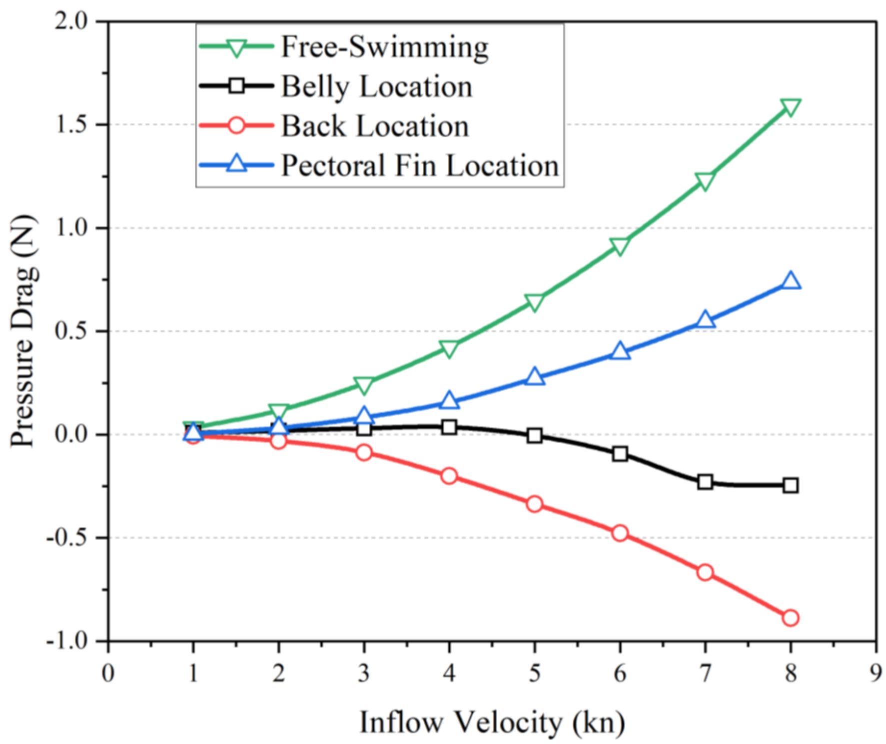

Figure 3-25 Comparations of the shear forces for remora in different conditions.

As for the belly-location, the back-location and the pectoral fin-location cases, the simulated results are plotted with the pressure on the surface and the velocity on the section, as shown in Figure 3-26, Figure 3-27 and Figure 3-28. In the belly location case presented in Figure 3-26, the area around the remora has displayed as a low velocity region, in which remora is hiding in this area. In this area, adverse pressure gradient builds up because of the blockage of the shark body. Therefore, the shear component of the drag presented the highest reduction comparing to other attachment locations. And after 4kn velocity the pressure force provide a forward thrust to remora, which demonstrated the effect by adverse pressure gradient.

Regarding to back attached case, in Figure 3-27, a larger adverse pressure gradient region builds up behind the dorsal fin because of slope of the shark back, thus the pressure force provides a higher forward thrust than the one in the belly attached case. Therefore, it can be confirmed that higher drag reduction rates for remoras are related to the low velocity and the adverse pressure gradient regions. While the simulations indicate that the back location provides the highest energy savings for the remora due to reduced drag and favourable flow conditions, it is important to consider that remora attachment behaviour is influenced by more than just hydrodynamic efficiency. In natural environments, remoras often attach to the belly of the shark, as this position offers several advantages beyond energy conservation. The belly area may provide greater protection from predators, a more stable attachment point, and easier access to food remnants. Moreover, due to the remora’s relatively weaker swimming ability, the belly is more accessible during attachment and detachment, allowing the remora to approach and disengage from the host more easily. Additionally, preference of suction location seems to be related to sex of host sharks [34]. This complex interaction between biological needs and physical forces suggests that the remora's attachment preference is a balance between energy efficiency, safety, and practicality.

However, for the pectoral-fin attached case, although the pectoral fin of shark blocks a part of incoming flow, the most of remora body is exposed to the incoming flow and high-velocity and high-pressure regions can be found around the remora body. Therefore, in this attachment location the drag reduction rate is the lowest. Meanwhile from the trends of pressure force in Figure 3-24 the pressure force increases with the flow speed showing similar trend with the free-swimming condition, which proofs that no adverse pressure gradient has acted on the remora during this condition.

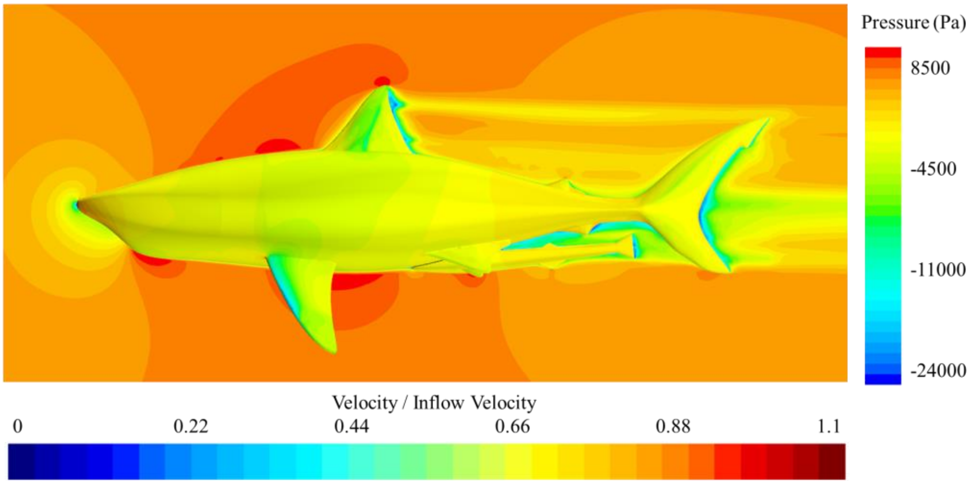

Figure 3-26 Velocity and pressure contours of the remora attached to the belly of the shark.

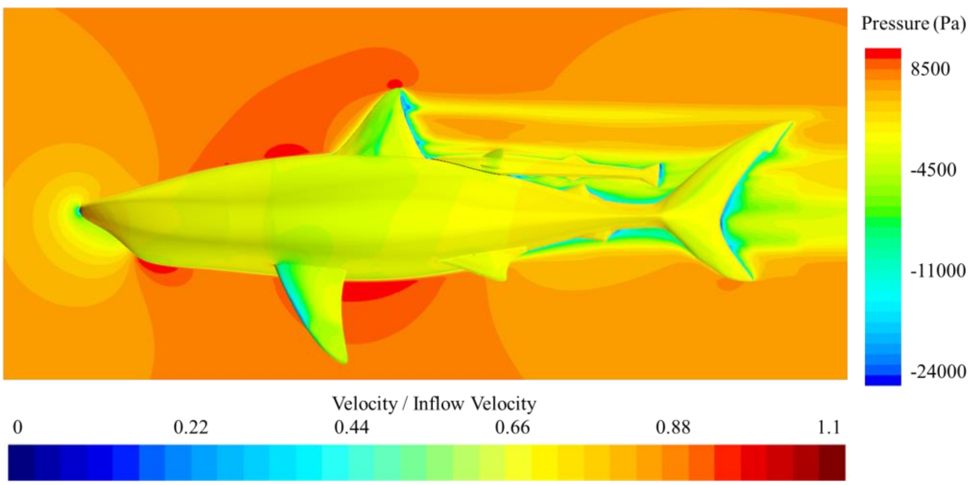

Figure 3-27 Velocity and pressure contours of the remora attached to the back of the shark.

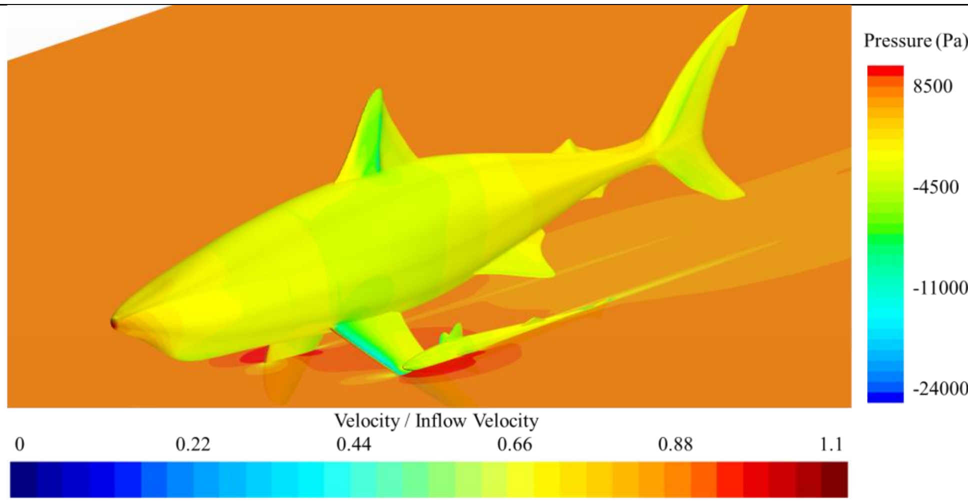

Figure 3-28 Velocity and pressure contours of the remora attached to the shark pectoral fin.

Figure 3-29 shows the total drag increase rate of the shark and the remora together for the different attachment locations. These three locations have a similar trend from 1kn to 8kn velocity particularly for belly attachment and back attachment. However, attaching to the pectoral fins shows the lowest total drag increase rate.

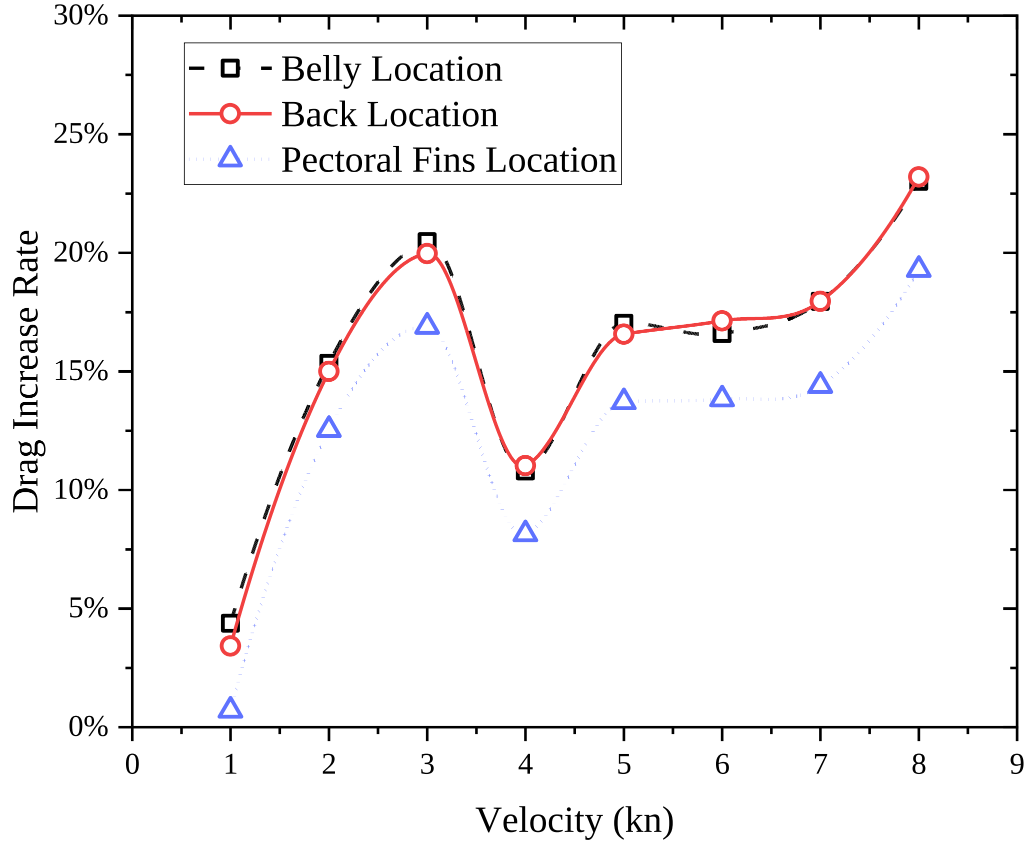

Figure 3-29 The increase rate of the total drag on the shark plus remora in different velocities.

3.4 Concluding Remarks

In this chapter, an investigation has been conducted to study the hydrodynamic characteristics of the remora fish in attached swimming conditions. This research has primarily focused on the investigations of the effect of the boundary layer flow and the attachment locations of the remora to the body of a shark. By using computational fluid dynamics tools, the following detailed conclusions can be drawn:

1) Regarding the effect of boundary layer flow on the remora fish, a systematic study with parametrically developed boundary layer flow was conducted and found that the drag reduction rate is directly related to the boundary layer thickness. Up to 42% of drag reduction rate can be

achieved at the lowest velocity (V=1kn) with the thickest boundary layer, therefore explaining the remora fish tends to seek a developed boundary layer when attaching to the body shark.

2) In terms of the attachment locations, the most frequent locations are the belly, the back and the pectoral fin of the shark. It is found that the belly and the back locations are the regions with the lowest velocities and adverse pressure gradient regions. Therefore, not only the boundary layer, but also the flow characteristics in the attachment locations are determining factors in the drag reduction rate of the remora.

3) The drag reductions of the belly attachment case and the back attachment case reached 61% and 59% respectively. The drag reduction rate increases with the speed for these two locations, whereas the pectoral fin location showed the opposite trend, dropping and converging to a 29% drag reduction rate. Despite the higher drag reductions observed in both the belly and back attachment cases, remoras often prefer attaching to the belly in natural environments. This preference is likely driven by factors beyond hydrodynamics, such as ease of attachment due to their weaker swimming ability and the increased protection offered by the belly area, particularly during detachment.

4) When remora attaches to the shark, it can be noted that the total drags increase, and the increase rate rises with the speed. At the highest tested velocity (8 kn) and at the belly and the back, the drag increase rate reaches 23%. Contrarily, when the remora is attached to the pectoral fin, the increase of the total drag is 18%.

Chapter 4

The Remora-Inspired AUV

The findings of a prior hydrodynamics study of the remora provided both the inspiration and confidence to apply the remora's unique behaviours on the development of an underwater dynamic AUV recovery strategy. Consequently, a design study is conducted to hydrodynamically design a remora fish inspired AUV, and this chapter presents an investigation into the hydrodynamic performance of the remora-inspired AUVs. Two types of simulations were conducted in this chapter. The first type of simulation, the AUV free-stream analysis simulations, was performed as a benchmark to understand the individual hydrodynamic performances of the remora-inspired AUV. The second type was the AUV-flat plate attachment analysis simulations, which were conducted to investigate the hydrodynamic characteristics of the remora-inspired AUV under the developed boundary layer.

Under this framework, this section 4.1 presents a remora-inspired biomimetic design approach, followed by the numerical methodology for the improvement of the AUV hull design in Section 4.2. Then, the Section 4.3 shows an analysis of the simulation results, and the overall conclusions of the chapter are presented in Section 4.4.

4.1 Remora-inspired Biomimetic Design

Remoras have evolved specialized adaptations that enable them to attach securely to hosts, even under dynamic flow conditions. This ability offers valuable insights for the design of Autonomous Underwater Vehicles (AUVs), particularly in scenarios involving underwater docking and recovery operations where stable attachment is essential. This study focuses on developing a remora-inspired AUV design, aiming to incorporate the remora’s unique attachment mechanism into a novel dynamic recovery strategy for AUVs.

In this study, the AUV design was modified from the traditional torpedo-shaped AUV prototype. The dimensions of existing AUVs, such as the REMUS series [48], Slocum [49], Spray [50], and Seaglider [51], were referenced to determine the key parameters. For the AUV hull design, inspiration was drawn from the remora fish, incorporating a flat surface on the body to facilitate docking operations. Additionally, a blended wing-body design was incorporated, with the nose elongated and pointed to reduce drag. It is important to note that, at this stage, the primary focus was on designing the AUV hull for the subsequent docking path research, without the addition of large wings. The wings that are integrated with the AUV hull remain relatively small, serving mainly to raise the centre of lift and enhance AUV stability. Further optimization of the AUV body will require more simulations and experiments, which will be conducted in future studies.

In the current research phase, the hydrodynamic improvements were focused on the AUV's stern. Two versions of the AUV hull (the initial design and the improved design) have been developed for comparison, as shown in Figure 4-1, with the main specifications listed in Table 4-1. The improvements were aimed at minimizing resistance when the AUV was attached to a flat plate. The initial AUV design, when attached, exhibited a low-pressure area near the stern, causing flow separation and vortices. Based on observations of the remora fish's docking posture on a shark, where the body often forms a sharp angle of approximately 5 degrees with the surface, the AUV's stern design was adjusted accordingly. In the meantime, although the remora's head has evolved into a wider suction disk, its body quickly tapers into a streamlined, flat shape. Thus, the stern of the AUV was improved by forming a sharp angle at the transition point, and the sides of the stern were modified into a 'V' shape. After these modifications, the low-pressure area at the stern disappeared, and no flow separation or vortices were observed. Further details of this improvement will be discussed in the following sections.

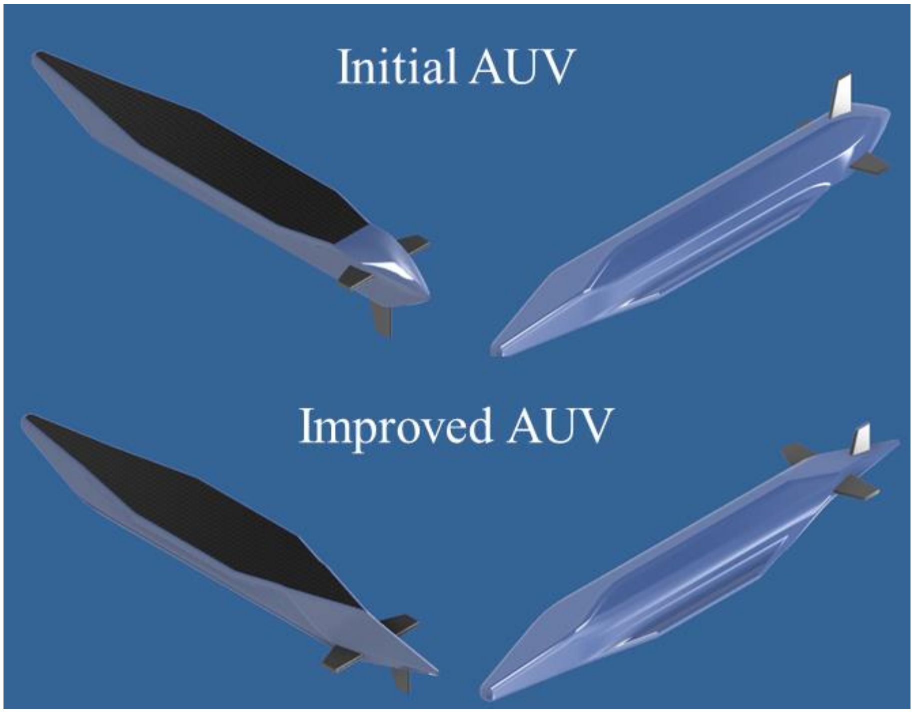

Figure 4-1 The remora-inspired AUV models.

Table 4-1 Main particulars of remora-inspired AUV model.

Main Particular	AUV
Hull Length (m)	2.000
Hull Width (m)	0.320
Hull Height (m)	0.210

The goal of this bio-inspired study is not to replicate the remora's body shape but to leverage its unique attachment mechanism, providing valuable insights for enhancing AUV docking capabilities. Using equation 3-2, the simulation results indicate that the AUV’s resistance coefficient is approximately 0.17 at a speed of 1.769 m/s, demonstrating excellent hydrodynamic performance in freestream conditions. This suggests that the remora-inspired design did not introduce significant disadvantages to the AUV's overall hydrodynamic efficiency, preserving its performance while improving docking functionality.

4.2 Numerical Methodology

Numerical simulations were conducted using the CFD software STAR-CCM+ to explore and improve the hydrodynamic performance of the remora-inspired AUV. A Reynolds-Averaged Navier–Stokes (RANS) model along with a K-ω Shear Stress Transport (K-ω SST) turbulence model also is employed.

a) Computational Domain

A cuboid domain was employed to carry out a resistance analysis under free stream conditions, which shows in Figure 4-2. The recommended dimensions for the computational domain were used [121]. The no-slip wall was used on the full surface, located 3L (length of the model) from the inlet and the sides, which were defined as the velocity inlet and the symmetry respectively. The outlet was defined as a pressure outlet and located 5L away from the model.

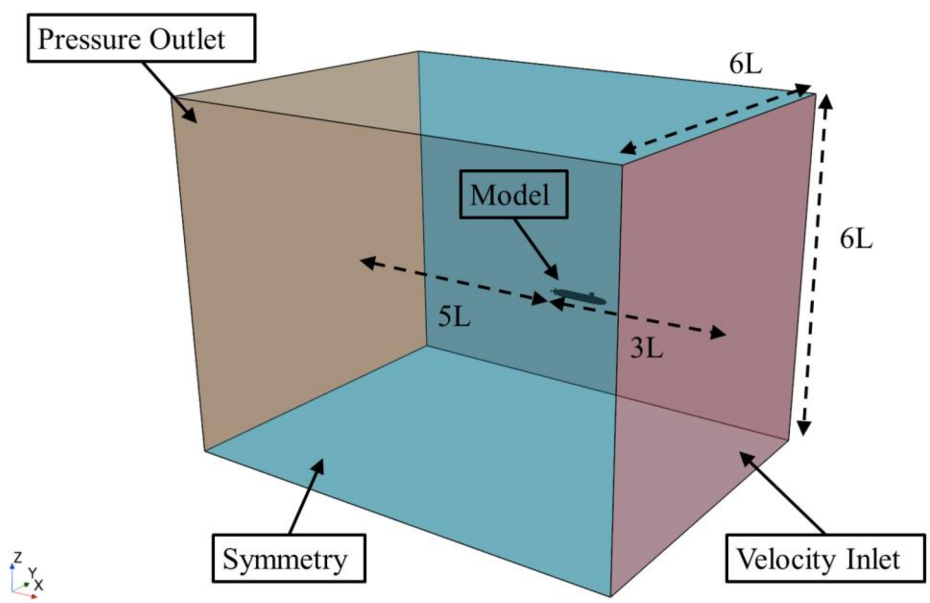

Figure 4-2 Domain and boundary condition of AUV free-stream simulations.

To improve the AUV hull, a set of simulations with the AUV docked onto a flat plate with fully developed boundary layer flow are conducted. The cuboid domain also was used, the bottom surfaces were defined as a non-slip wall to generate a range of boundary layer flow, as shown in Figure 4-3. The outlet boundary condition was a pressure outlet and is 5L downstream from the model. The upstream boundary was set as velocity inlet, and the distance between inlet and model was 30m/ 50m/ 70m/ 90m which introduced variable the thickness of the boundary layer. The symmetric top and sides surface were positioned 3L from the model.

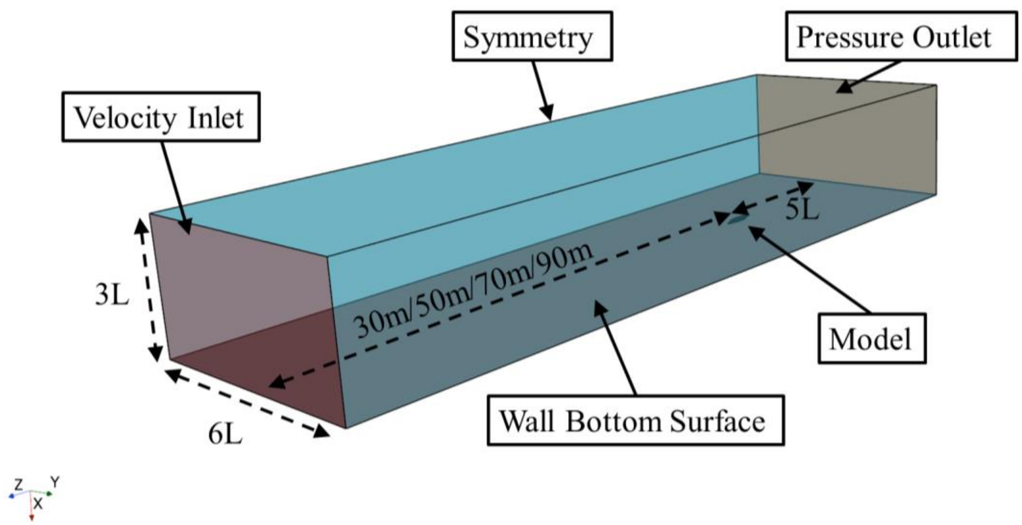

Figure 4-3 Domain and boundary condition of AUV-flat plate attachment simulations.

b) Mesh Generation

Regarding the mesh generation, the same setting was applied as previous simulations. The mesh view was shown in Figure 4-4, and in AUV free-stream simulations the cell count was 2.53 million and y+ was kept below 1. For the AUV-flat plate attachment simulations, the cell counts were 2.26~2.32 million, and the y+ was kept below 1 for the AUV model and the domain bottom.

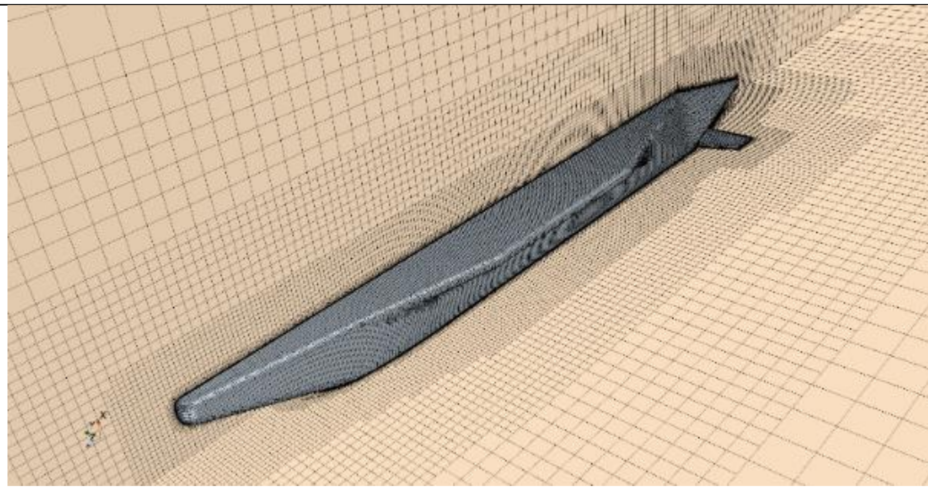

Figure 4-4 Mesh view of the remora-inspired AUV model.

A grid independence study was conducted to verify the simulation setup [125, 126]. Three different grid groups were used, including a coarse grid, a medium grid, and a fine grid, with a grid refinement ratio R of approximately 1.3. The grid parameters were kept fixed as percentages of the base size, while the grid size for the surface and volume mesh was varied by modifying the base size, except for the prism layer mesh. The numerical uncertainty values for the resistance were approximately 0.4425% for the AUV, as presented in Table 4-2. Based on the computational cost and accuracy, the medium grid was chosen for subsequent analyses.

Table 4-2 Grid independence study-AUV.

Parameter	
Fine Grid	4633230
Medium Grid	2528192
Coarse Grid	1662301
Resistance-Fine Grid	180.564N
Resistance-Medium Grid	186.325N
Resistance-Coarse Grid	211.498N
GCI_{fine}	0.442 %

4.3 Improved AUV Hull Design

A higher inflow velocity of 8.107 m/s was applied to the velocity inlet in this study. This velocity value was determined based on the results of the full-scale submarine self-propulsion analysis simulation (in Chapter 4), which showed that the thickness of the boundary layer around the submarine could fully envelop the AUV model at a forward speed of 8.107 m/s. Table 4-3 gives the results of the initial AUV resistance simulation results in the free stream condition.

Table 4-3 The resistance of initial remora-inspired AUV in free stream condition.

Total Resistance (N)	Pressure Resistance (N)	Shear Resistance (N)
226.358	95.505	127.855

Before conducting the AUV-flat plate docking simulations, with previous work conducted evaluating the remora fish in attached swimming, it can be expected that the total resistance of the AUV would reduce as the thickness of the boundary layer increased with the increased distance between the AUV and front end of the flat plate. This is because the AUV was docked on the flat plate sheltered by the developed boundary layer flow. However, the results do not conform to expectations as shown in Figure 4-5. Comparing the free-stream condition, the total resistance has a slight change and there is a significant increase of the pressure resistance. In addition, as the thickness of the boundary layer increases, the increase of resistance reduction rate decreases.

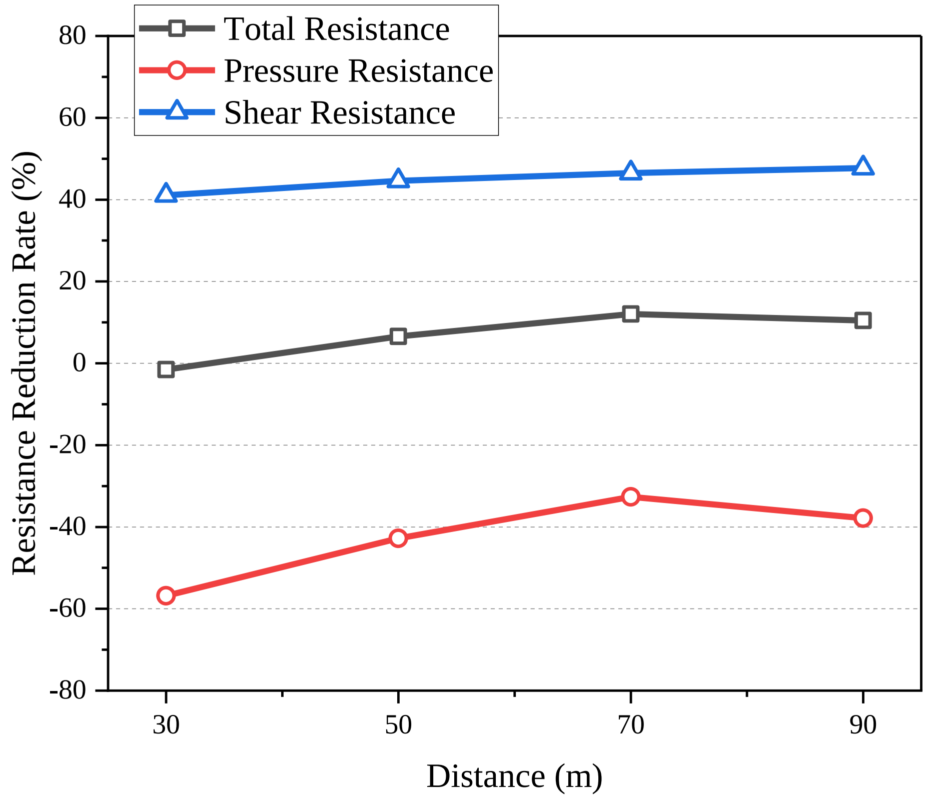

Figure 4-5 Resistance reduction rate of the resistance in flat plate docking condition compared to the free-stream condition for initial AUV at different distances between the AUV and the upstream inlet.

Figure 4-6 shows the velocity contour of AUV the flat plate from 30m to 90m with the initial AUV model. As observed, the boundary layer thickness increases with the distance which fully covers the AUV hull. But there is also a low-pressure region occurring after the stern of the initial AUV design for all distances which indicates flow separation and does not seem to be affected by the thickness of the boundary layer. In the low-pressure region, further analysis shows the flow separation and vortices generated, as can be seen in Figure 4-7, which increases pressure resistance of the AUV.

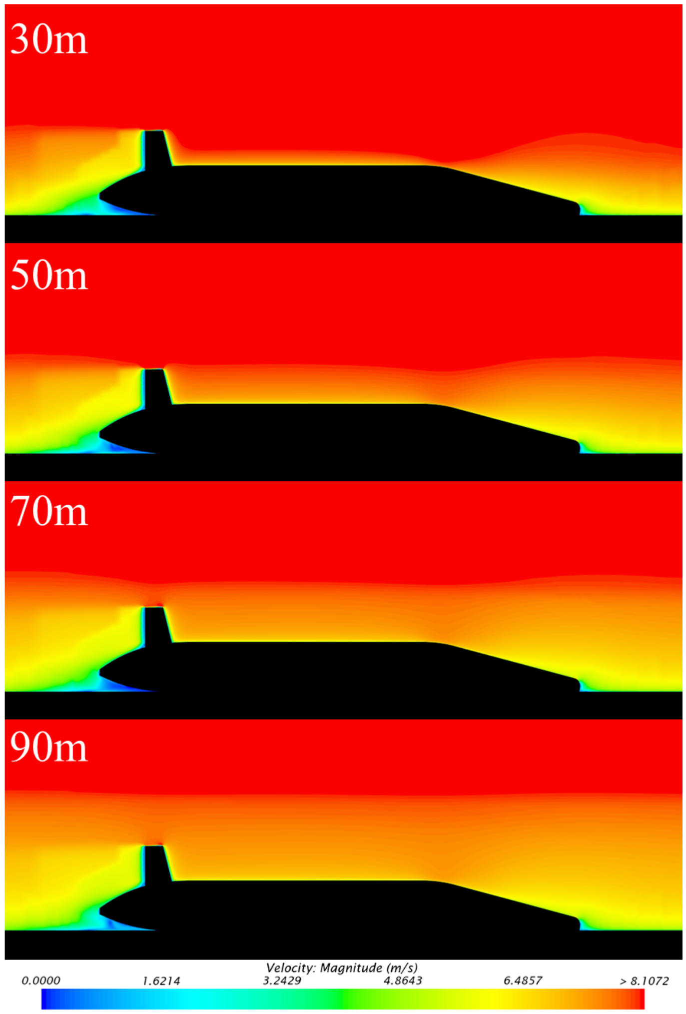

Figure 4-6 The velocity contours of initial AUV docking on the flat plate.

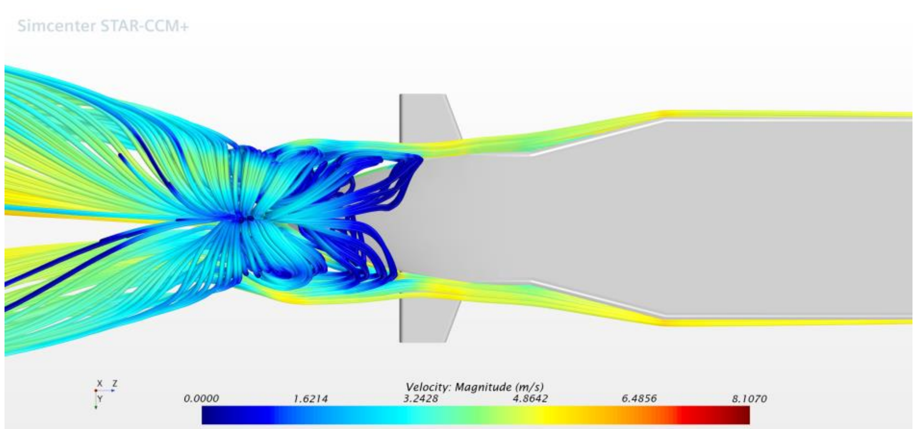

Figure 4-7 The streamline at the stern of initial AUV.

After that, it can be confirmed that the low-pressure region is the reason why the AUV-flat plate analysis results differed from the initial expectation. Since pressure resistance mainly comes from the influence of shape, the design of AUV was improved to eliminate the low-pressure region at the stern of AUV. The comparison of the initial AUV and the improved AUV is shown in Figure 4-8. The improvement was inspired by the posture of remora fish docking on the shark. The transition between the stern and body of the AUV was set at an angle, and the bottom of the stern was modified to prevent the occurrence of flow separation and vortices.

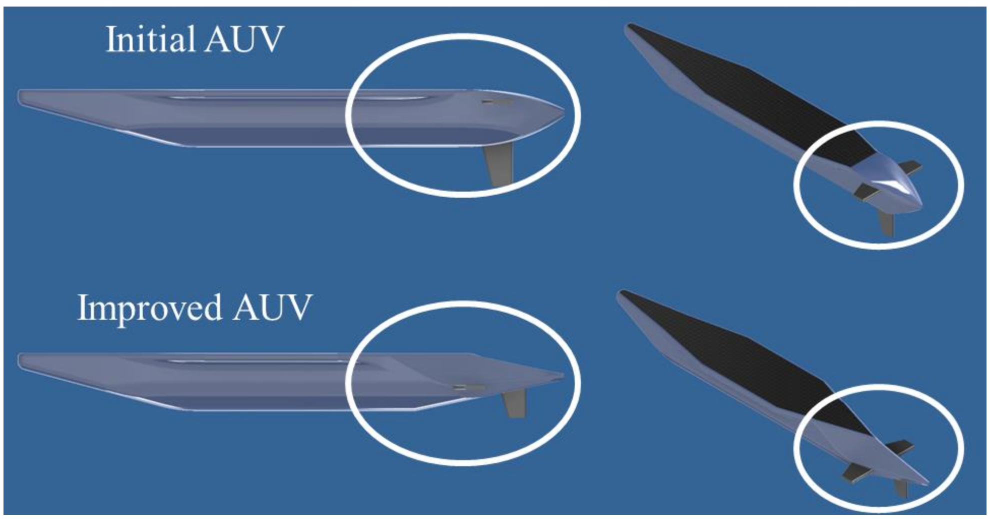

Figure 4-8 The comparison of the initial AUV and the improved AUV.

Comparing the initial AUV, there are lower resistances in free stream condition for the improved AUV which can be seen in Table 4-4, and the total resistance reduction rate achieves 17.69%. A significant increase in total resistance and pressure resistance reduction rate can be seen in Figure 4-9, all resistance reduction rates increase with increased thickness of the boundary layer. As Figure 4-10 and Figure 4-11 show, the low-pressure regions almost disappear, and around the stern of AUV, there are no flow separation and vortices. Furthermore, additional simulations at various velocities were conducted serve as benchmark references for subsequent studies, as illustrated in Figure 4-12.

Table 4-4 The resistance of improved remora-inspired AUV in free stream condition.

Total Resistance (N)	Pressure Resistance (N)	Shear Resistance (N)
186.325	72.949	113.376

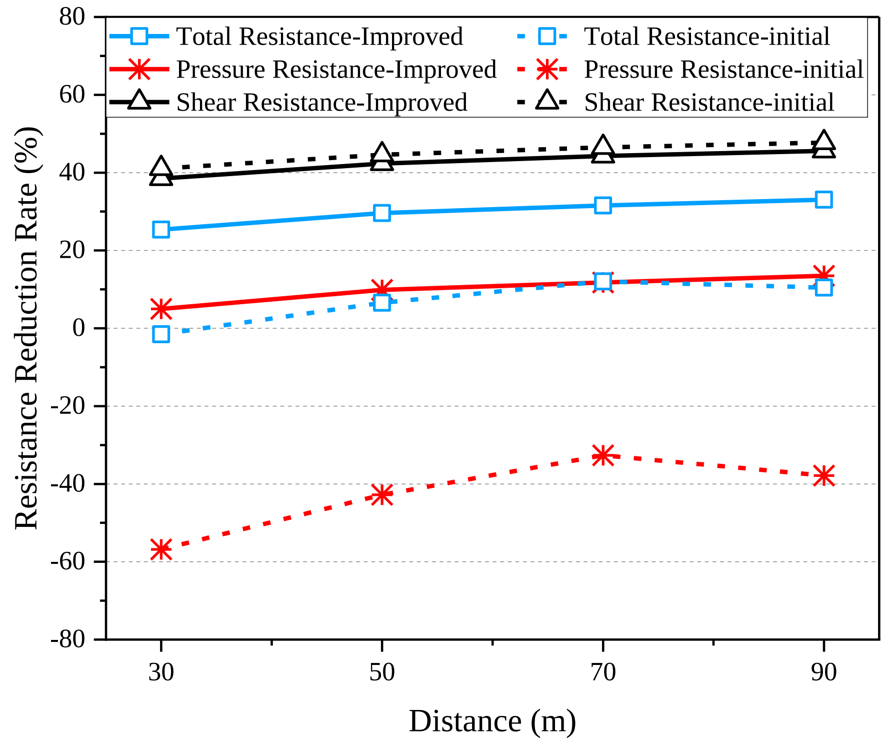

Figure 4-9 The resistance reduction rate of the resistances for improved and initial AUV.

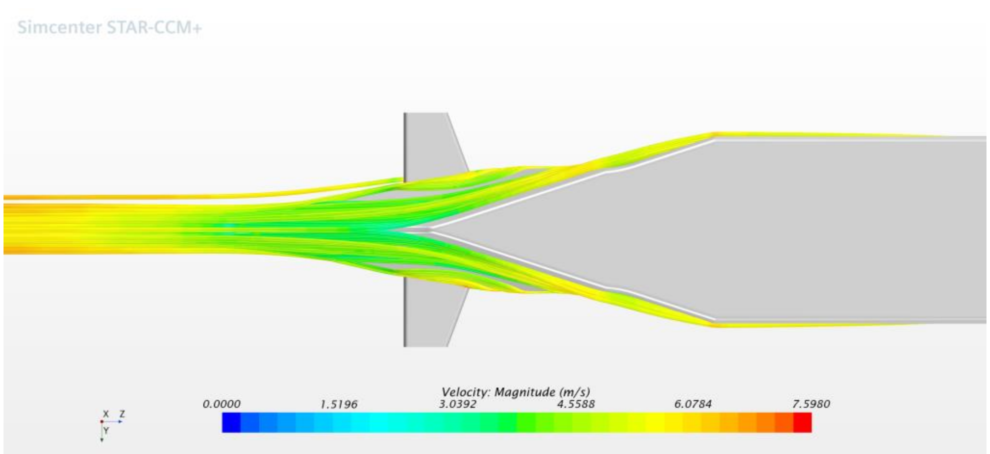

Figure 4-10 The streamline at the stern of Improved AUV.

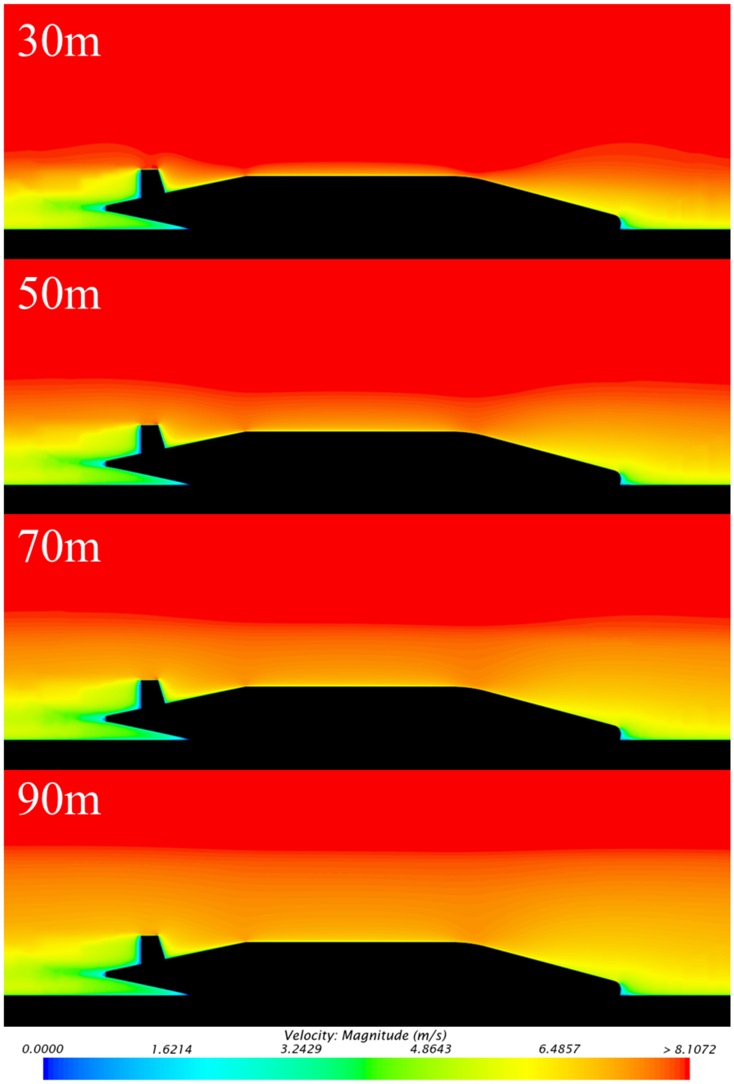

Figure 4-11 The velocity contours of initial AUV docking on the flat plate.

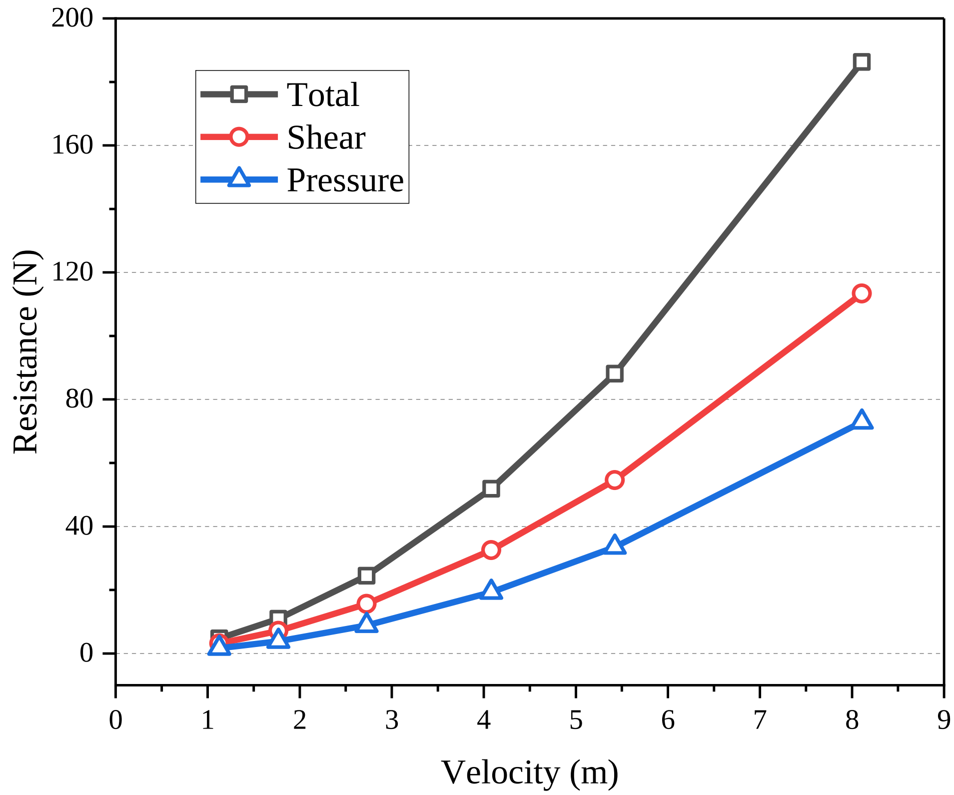

Figure 4-12 The resistance of the remora-inspired AUV in the free stream.

4.4 Concluding Remarks

This chapter introduces a newly designed AUV inspired by the remora fish. This model will serve as the basis for examining AUV docking operations in the subsequent chapter. The following conclusions have been drawn:

1) The remora-inspired AUV hull form is first time developed and evaluated using computational fluid dynamics.

2) The hull design of the AUV inspired by the remora fish has been developed and assessed using computational fluid dynamics for the first time. An improvement, inspired by the posture of remora fish docking on the shark, was implemented. Compared to the initial design, the improvement resulted in a 17.69% reduction in resistance.

3) By improving the design of the remora-inspired AUV, the low-pressure regions behind the stern of the AUV almost disappear, and there is no longer flow separation and vortices generated.

4) Through the investigation of the hydrodynamics characteristics of the remora-inspired AUV, the AUV-flat plate attachment analysis reveals a significant reduction in resistance, ranging from 25.36% to 33.03% as the thickness of the boundary layer increases, which is in line with the previous research and the expectations.

Chapter 5

Hydrodynamics of the Remora-inspired AUV in Attachment Conditions

In Chapter 3, an investigation has been conducted to determine the hydrodynamic characteristics of a remora in the unique docking behaviours with a shark. In the meantime, inspired by the study in remora, a new designed AUV hull model has been prepared for this chapter.

Based on the above analysis, the following chapters will explore the feasibility of a underwater dynamic AUV recovery strategy. In this conceptual strategy, when the remora-inspired AUV requires recharging or data transfer, it will approach the larger underwater mother vehicle. Utilizing the low-velocity region surrounding the mother vehicle, the docking operation will be executed. This chapter emphasizes the validation of the CFD simulation methodology for the following chapters, examining the influence of different attachment location for the remora-inspired AUV, as well as the impact of the mother vehicle's forward velocity.

Within this framework, Section 5.1 presents the CFD setup and all models utilized in subsequent analyses, including Chapter 6. Section 5.2, 5.3, and 5.4 outline the CFD simulation methodology and its validations for resistance analysis, open water propeller analysis and self-propulsion analysis, respectively. In Section 5.5, a comprehensive study examines the influence of various docking locations on a submarine surface for the remora-inspired AUV. The chapter concludes with a summary of findings in Section 5.6.

5.1 CFD Simulation Preparations

Prior to the research of the remora inspired AUV, the CFD simulation methodology was established and several validation studies using the benchmark submarine model were conducted to gain confidence for the used numerical methodology. Numerical simulations were conducted using the CFD software STAR-CCM+ to investigate the hydrodynamic characteristics. A Reynolds-Averaged Navier–Stokes (RANS) model along with a K-ω Shear Stress Transport (K-ω SST) turbulence model which has been extensively utilised in industrial applications [115, 116] is employed in this study. In all simulations, the reference altitude was set at the centre of domain, and the density of water was 997.561 kg/m3 with the dynamic viscosity of 8.8871E-4 Pa-s.

A detailed description of the simulated models used in the study is provided below. The benchmark submarine model is the open-source DARPA Suboff AFF-8 submarine model with the INSEAN E1619 propeller model. Full-scale models were applied in this study to investigate the hydrodynamic behaviour, while model-scale versions were used in the validation study. These model-scale versions were identical to those employed in experimental tests, ensuring consistency in the validation process. The remora-inspired AUV model is in-house developed inspired by the remora.

a) DARPA Suboff AFF-8 Submarine Model

DAPRA Suboff submarine model is a widely recognized benchmark model with the available research on its performances in both model and full-scale conditions [127, 130-132]. It is used as the mother vehicle for this investigation. In this study, considering that the presence of appendages such as the sail and rudders can significantly affect the flow around the submarine, the fully appended model, called AFF-8, was utilized. Figure 5-1 illustrates the 3D geometry of the DARPA Suboff AFF-8 submarine model, while the key parameters are provided in Table 5-1.

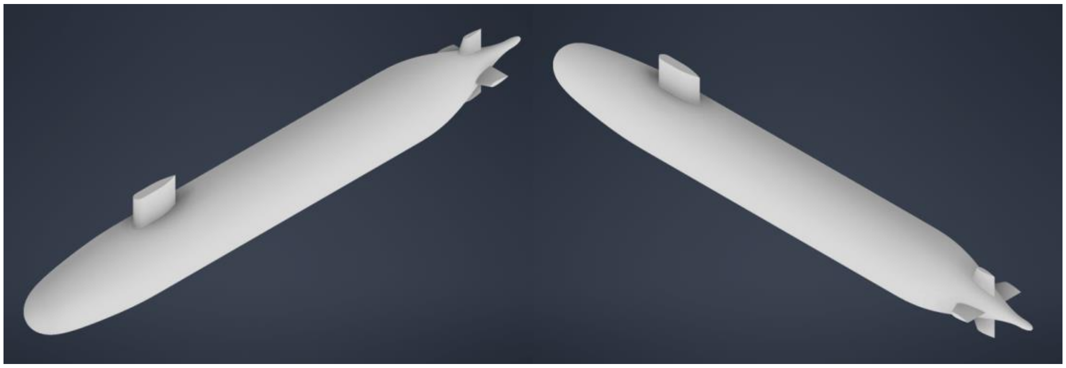

Figure 5-1 The 3D geometry of the DARPA Suboff AFF-8 submarine model.

Table 5-1 The basic parameters of the DARPA Suboff AFF-8 submarine models.

Main Particular	Model Scale	Full Scale
Scale	24	1
Length (m)	4.356	104.544
Maximum Diameter (m)	0.508	12.192

b) INSEAN E1619 Propeller Model

Chase and Carrica [132] and Sezen, et al. [131] have previously conducted studies using the INSEAN E1619 propeller with the DARPA Suboff AFF-8 submarine model at full-scale and model-scale conditions. This study continued to use the same propeller for the self-propulsion simulations. The propeller was mounted at the stern of the submarine. Figure 5-2 shows the 3D geometry of the INSEAN E1619 propeller model, while Table 5-2 lists its fundamental parameters.

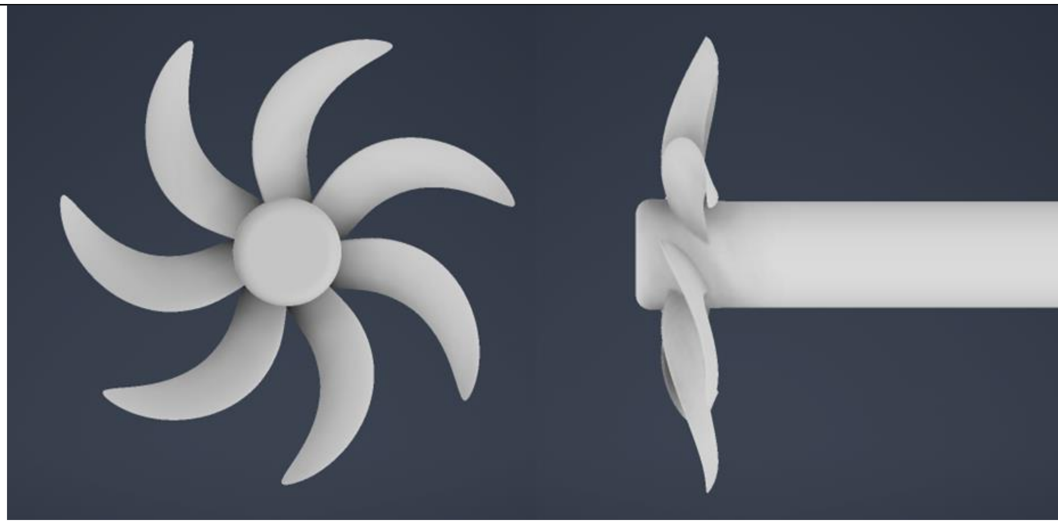

Figure 5-2 The 3D geometry of the INSEAN E1619 propeller model.

Table 5-2 The basic parameters of the INSEAN E1619 propeller models.

Main Particular	Model Scale	Full Scale
Scale	13	1
Diameter (m)	0.485	6.288
Number of Blades	7	

c) Remora-Inspired AUV Model

Inspired by the remora fish, the AUV used in this study feature a suction disk on one side of its hull to perform the docking operations. The remora-inspired AUV model is presented in Figure 5-3, and the basic parameters are shown in Table 5-3.

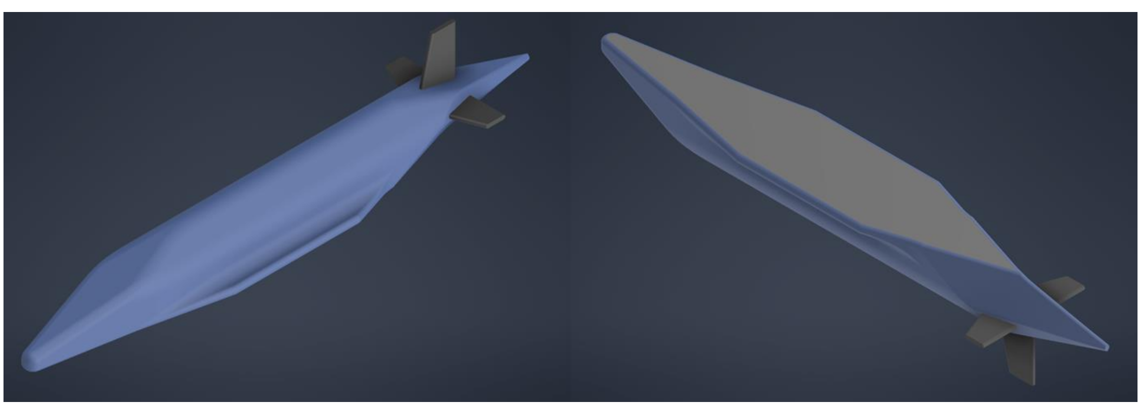

Figure 5-3 The 3D geometry of the remora-inspired AUV models.

Table 5-3 The basic parameters of the remora-inspired AUV models.

Main Particular	
Hull Length (m)	2.000
Hull Width (m)	0.320
Hull Height (m)	0.210

5.2 Methodology & Validation study I: Resistance Analysis

First, a resistance analysis for the benchmark submarine was conducted to validate the used CFD simulation methodology. The experimental data of the model-scale DARPA Suboff AFF-8 submarine resistance was provided by Liu and Huang [127]. To perform this analysis, a cuboid computational domain was created as shown in Figure 5-4. The recommended dimensions for the computational domain were used [121]. The no-slip wall was used on the full surface, located 3L (length of the model) from the inlet and the sides, which were defined as the velocity inlet and the symmetry respectively. The outlet was defined as a pressure outlet and located 5L away from the model.

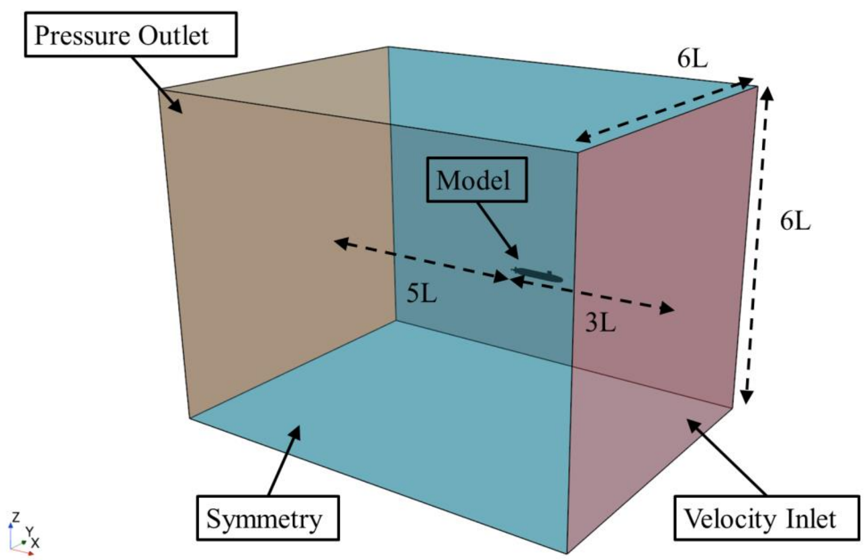

Figure 5-4 Domain and boundary conditions of the submarine resistance analysis.

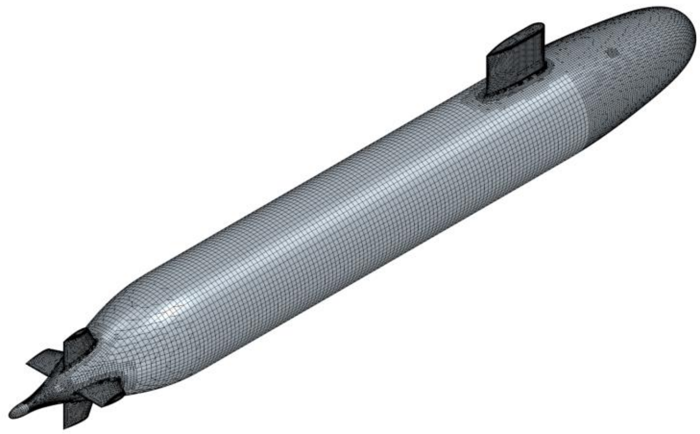

Figure 5-5 Mesh view of the model-scale DARPA Suboff AFF-8 submarine model.

A volumetric control automatic meshing tool was utilized to generate the mesh for the simulations. The mesh was refined near the models, particularly in the areas of the sail, rudders, stern, and propeller. The detailed mesh scenes can be viewed in Figure 5-5, and the cell count was 1.8 million. The wall treatment used in all simulations was the all y+ treatment setting in STAR-CCM+. The approach is a hybrid one that employs a high-y+ treatment (y+ > 30) for coarse meshes and a low-y+ treatment (y+ < 1) for fine meshes [116]. For the submarine simulations, the average y+ was kept below 1. The fine prism layer mesh, which was 0.2 m thick with 14 layers on the submarine surface was used to resolve the boundary layer.

The inflow velocities used in numerical simulations ranged from 3.051 m/s to 9.152 m/s, which were the same as those used in experimental data. Figure 5-6 shows good agreement between the numerical and experimental results, with differences ranging from 0.20% to 1.90% as summarized in Table 5-4.

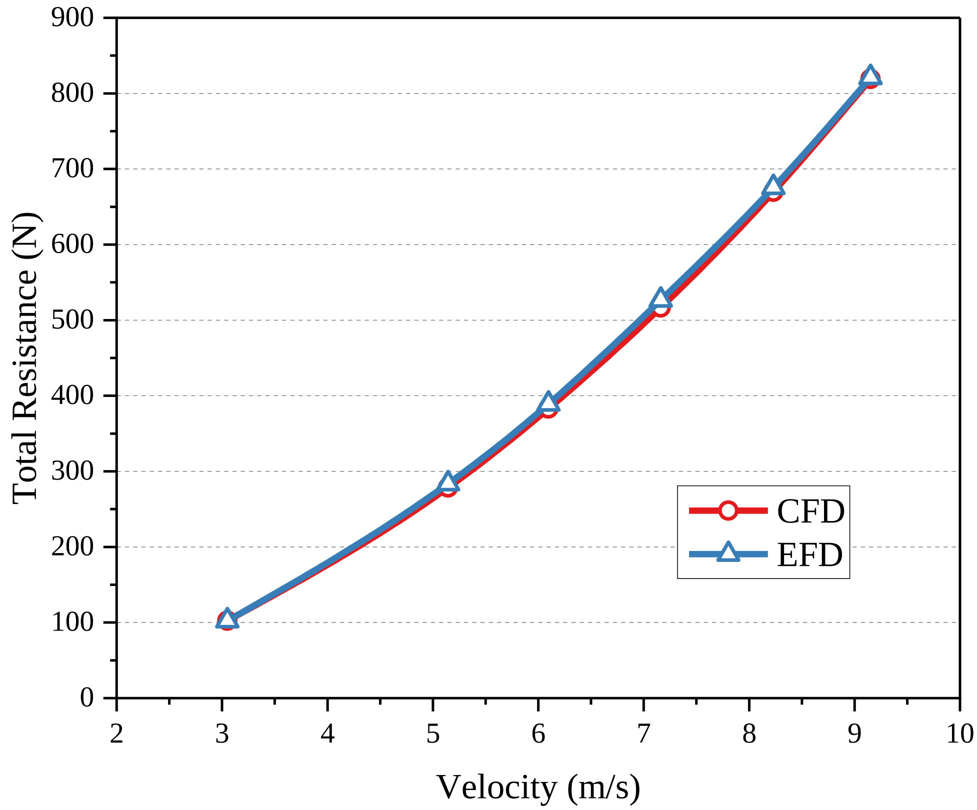

Figure 5-6 The comparison of the model-scale DARPA Suboff AFF-8 submarine resistances between the numerical and experimental results.

Table 5-4 The basic parameters of the DARPA Suboff AFF-8 submarine models.

Velocity (m/s)	Resistance – CFD (N)	Resistance – EFD (N)	Difference
3.051	102.5	102.3	0.20%
5.144	278.5	283.8	1.87%
6.096	383.0	389.2	1.59%
7.161	516.6	526.6	1.90%
8.231	669.9	675.6	0.84%
9.152	819.1	821.1	0.24%

5.3 Methodology & Validation study II: Open Water Propeller Analysis

With the confidence obtained from the resistance simulation, to validate the propeller simulation, the analysis of the open water propeller is conducted and compared against the experimental data [131, 133]. A cylindrical computational domain with stationery and rotatory regions was created, as shown in Figure 5-7. The no-slip wall condition was applied to the propeller model, while the diameter of the domain was set to 10 times the diameter of the propeller (10D). The inlet was defined as a velocity inlet, positioned 4D upstream from the model. A pressure outlet was applied to the outlet, which was 11D downstream from the propeller model. The circumferential face was defined as a symmetry plane. To properly capture the rotation of the propeller, 200 time-steps per revolution were used, as recommended by the ITTC Practical Guidelines for Ship CFD Applications guidelines [121].

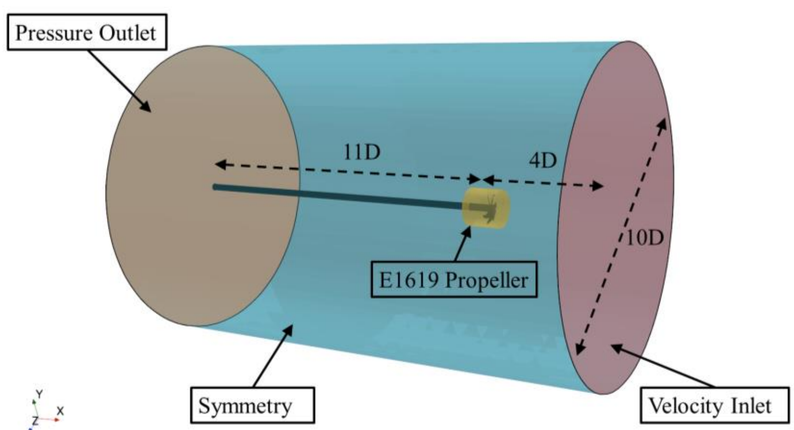

Figure 5-7 Domain and boundary conditions of the model-scale and full-scale open water propeller analyses.

The volumetric control automatic meshing tool and all y+ treatment setting also used for these simulations. The mesh scene is proved in Figure 5-8. The cell count was 0.59 million and the average y+ was kept above 30.

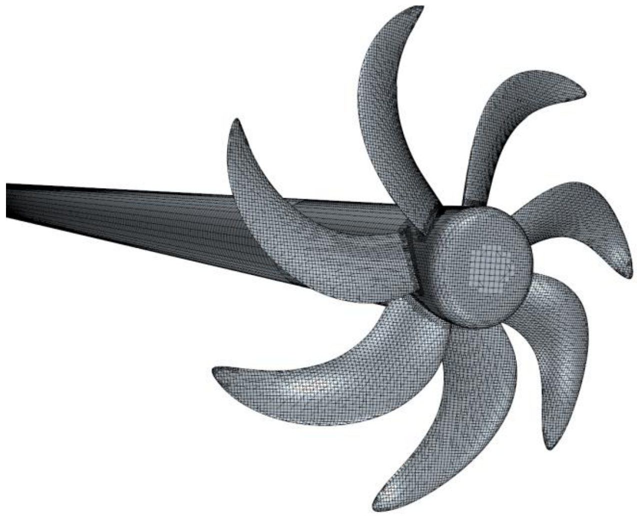

Figure 5-8 Mesh view of the INSEAN E1619 propeller model analyses.

The numerical results of the open-water analyses for model-scale INSEAN E1619 propellers, which were compared with experimental data provided by INSEAN[131, 133]. Nondimensional numbers were utilized to assess the accuracy of the numerical simulation. The advance ratio, J, was calculated with the following 5-1 [134]:

$$J = \frac{V_a}{n * D}, \tag{5-1}$$

where, V_a is the velocity of the inflow, m/s; n is the rotational speed of the propeller in revolutions per second; D is the propeller diameter, m.

The non-dimensional torque coefficients, K_Q, was calculated with the following 5-2 [134]:

$$K_Q = \frac{Q}{\rho * n^2 * D^5}, \tag{5-2}$$

where, Q is the torque, N*m; ρ is the density of the inflow, kg/m^3;

And the non-dimensional thrust coefficients, K_T, was calculated with the following 5-3 [134]:

$$K_T = \frac{T}{\rho * n^2 * D^4}, \tag{5-3}$$

where, T is the thrust, N*m.

The performance curves of the INSEAN E1619 propeller obtained from the numerical and experimental data are compared in Figure 5-9. The results indicate a good agreement for model-scale propeller open-water analysis.

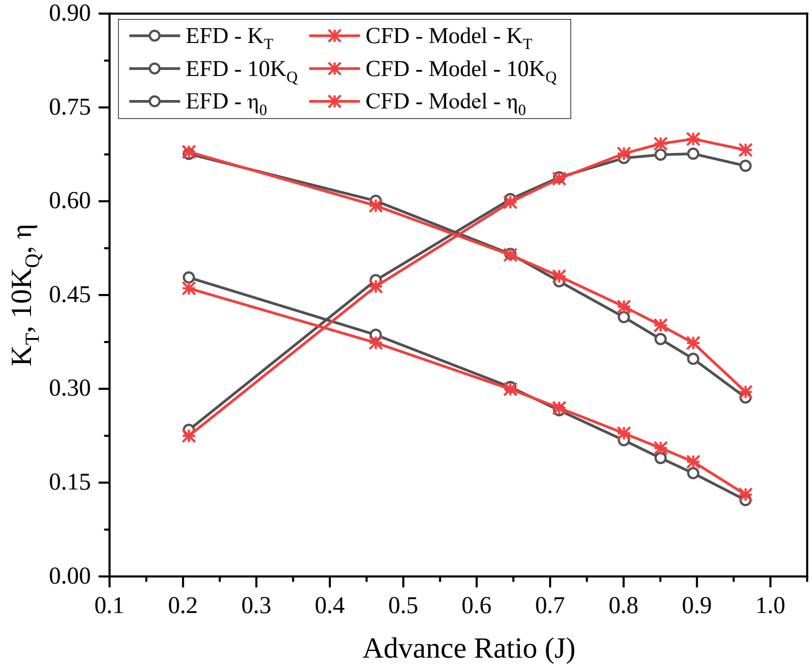

Figure 5-9 The Open water performance comparison of the INSEAN E1619 propeller between the numerical and experimental results.

5.4 Methodology & Validation study III: Self-propulsion Analysis

With both hull resistance simulation and propeller simulation, to understand the fully developed flow around the submarine hull with propeller action, a full-scale self-propulsion simulation was conducted. Due to the lack of full-scale measurement data, the simulation results were compared with another numerical simulation results by Sezen, et al. [135]. The same settings as the previous simulations, regarding the computational domain, the boundary conditions and the mesh generation, have been adopted. The detailed mesh scenes can be viewed in Figure 5-10 and the cell count was 6.30 million.

The Dynamic Fluid Body Interaction (DFBI) module of CFD software STAR-CCM+ was employed to perform this self-propulsion simulation. In the DFBI model, a propeller speed was predetermined, and the propeller generates the thrust to propel the submarine. The computational domain moves together with the submarine model referring to the submarine local coordinate system. As the submarine moved, the resistance increased with the increased velocity of the submarine until the net horizontal force of thrust and resistance became zero, at which the self-propulsion point could be found.

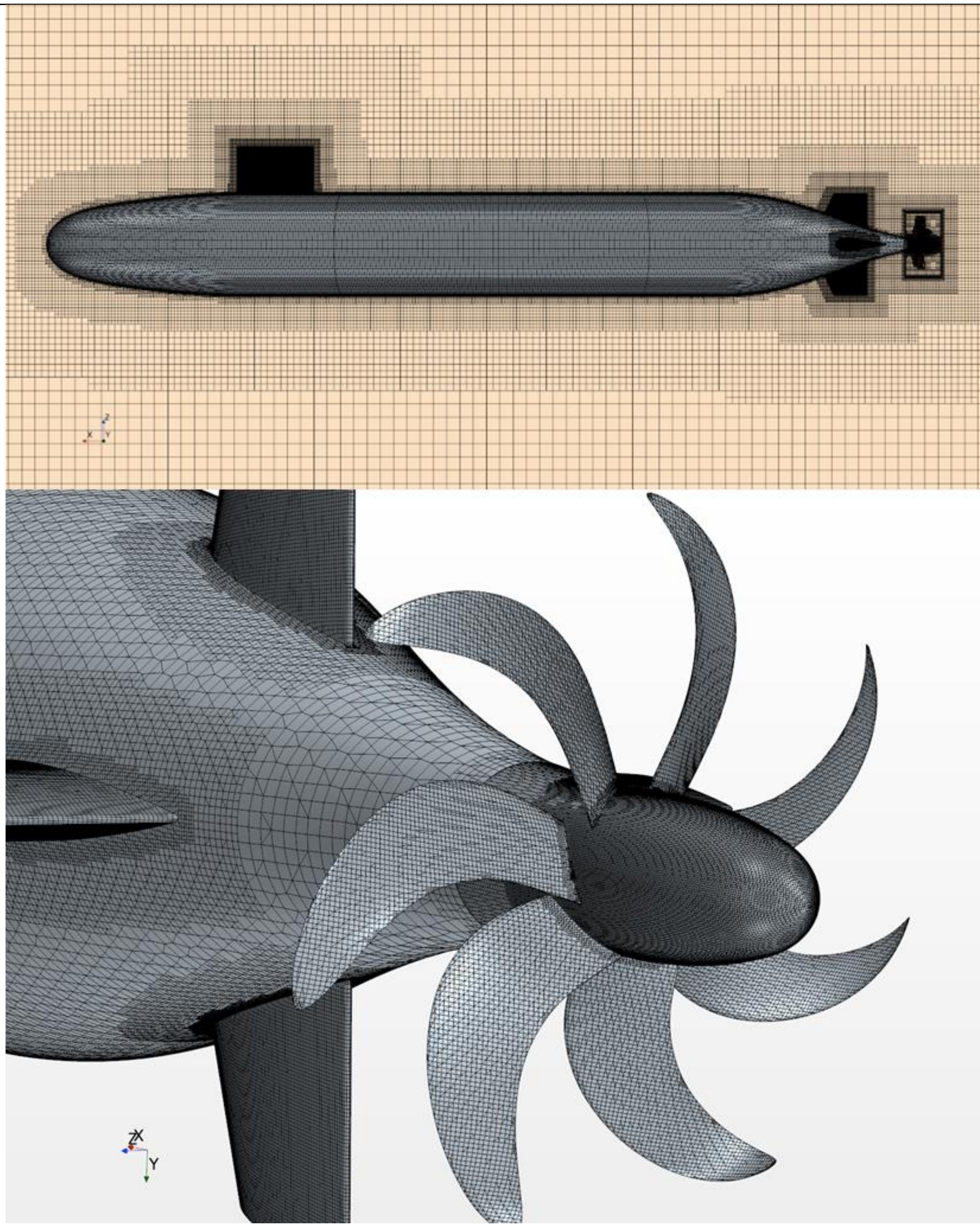

Figure 5-10 Mesh view of the Full-scale DARPA Suboff AFF-8 submarine model with the INSEAN E1619 propeller model.

Comparing the numerical results obtained using the DFBI method with the other numerical simulation result, good agreement is observed, as shown in Figure 5-11. The differences between the numerical and experimental results were approximately 5%, as shown in Table 5-5.

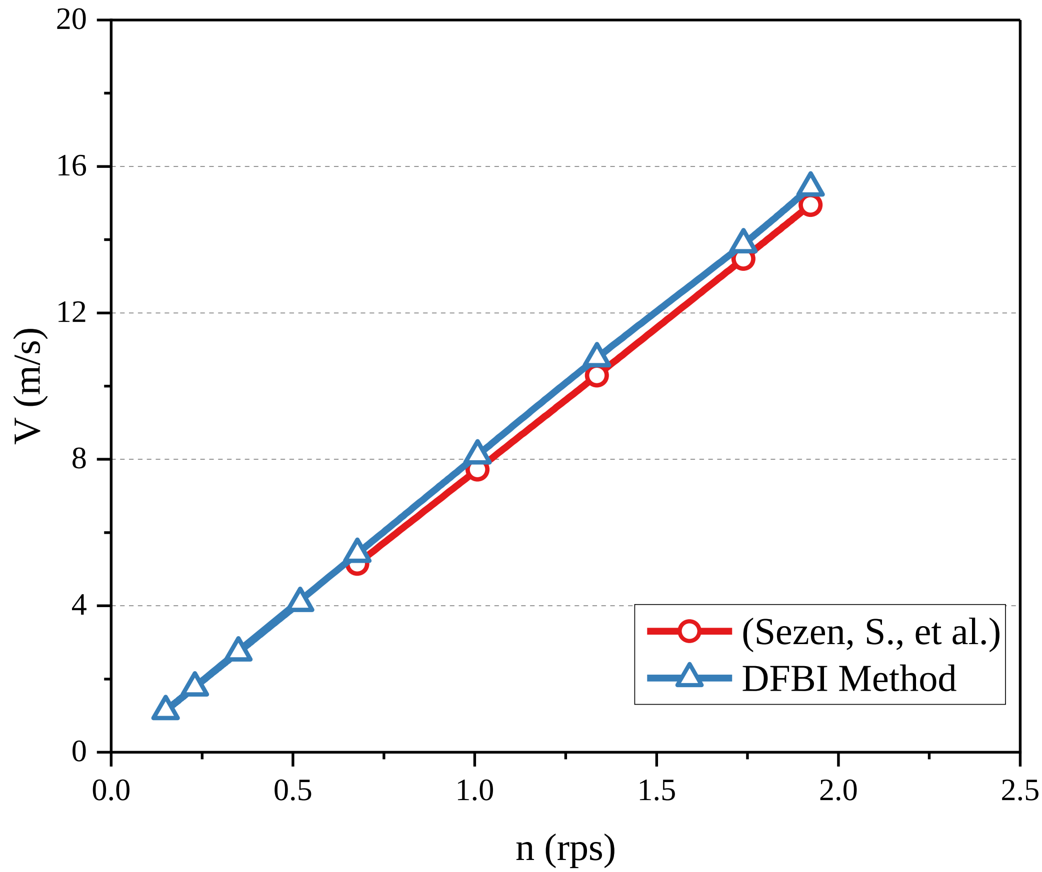

Figure 5-11 The comparison of the full-scale DARPA Suboff AFF-8submarine self-propulsion points.

Table 5-5 The difference between the common method and DFBI method results for the full-scale DARPA Suboff AFF-8 submarine self-propulsion analysis.

Propeller Speed (rps)	Common Method – Advance Velocity (m/s) (Sezen, et al.)	DFBI Method – Advance Velocity (m/s)	Difference
0.677	5.144	5.423	5.42%
1.008	7.717	8.107	5.06%
1.336	10.289	10.760	4.61%
1.739	13.473	13.878	3.02%
1.924	14.948	15.425	3.19%

5.5 AUV-Submarine Attachment Analysis

With the above CFD simulation validations, the AUV-submarine attachment simulations were performed to investigate the hydrodynamic characteristics of the AUV attached to various locations of the submarine. Then, the Reynolds number affect has been investigated with the AUV docked to the identified optimal docking locations.

a) Optimum Attachment Locations

According to the previous research in Chapter 3, remora-inspired AUV would favour fully developed boundary layer flow and adverse pressure gradient to achieve maximum resistance reduction to save energy. So to identify the best docking location for the developed AUV, this simulation has been conducted.

During these simulations, the inflow velocity was set to 8.107m/s, which is the design speed of the submarine and is consistent with the previous study. Velocity contours of low-velocity regions were extracted from the full-scale self-propulsion simulation, as shown in Figure 5-12. The boundary layer gradually develops along the hull. The thickness of the boundary layer increases first, but near the stern region the boundary layer thickness reduces due to the suction generated by the propeller. In addition, a large area of low velocity is developed behind the submarine sail.

Nine potential docking locations on the submarine surface were identified using the self-propulsion simulation in Section 5.4. In the longitudinal direction, three cross-sections (designated as A, B, and C in Figure 5-12) were chosen at the distances of 65 m, 45 m, and 27 m upstream of the stern of the submarine, respectively. In each cross section, three positions were selected which were on the top, side, and bottom of the submarine. Table 5-6 presents the thickness of the low-velocity regions and the ratio between its thickness and the height of the AUV for various attachment locations. The B section exhibited a thicker boundary layer than other positions.

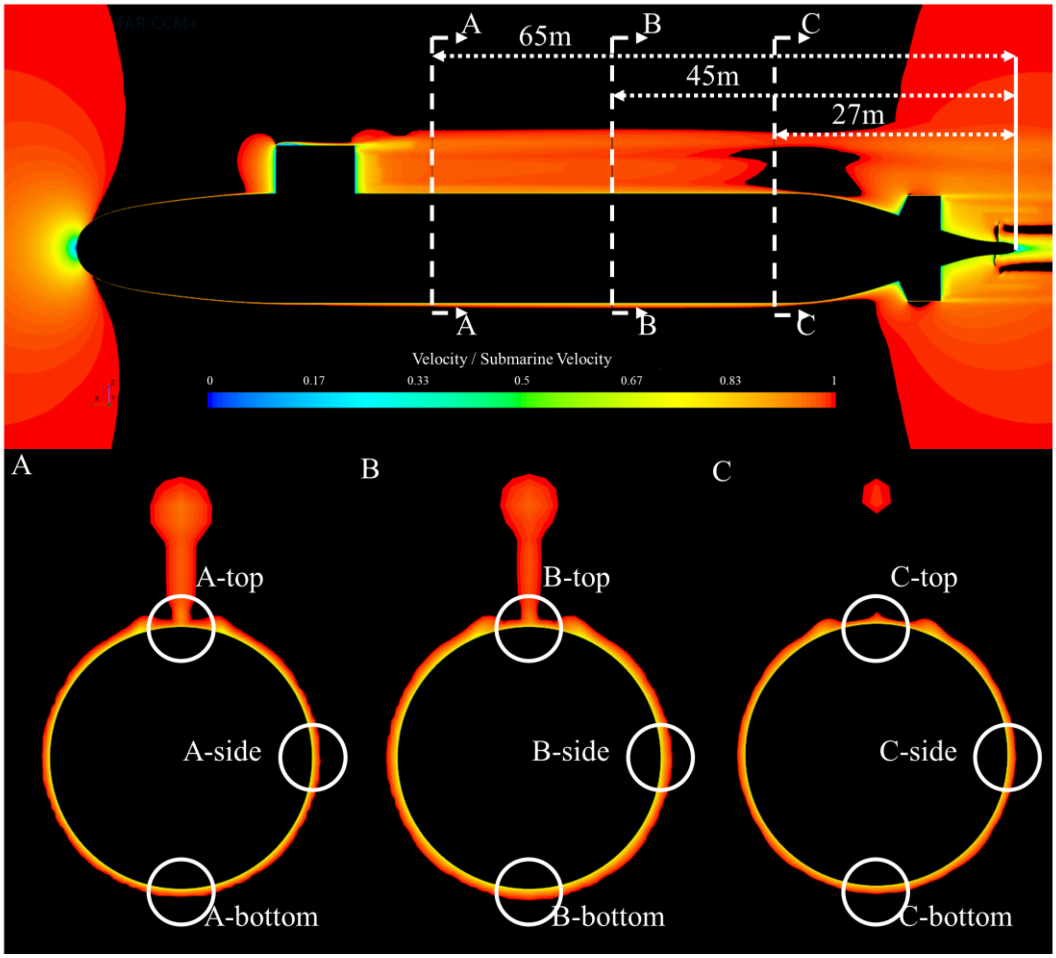

Figure 5-12 The low-velocity regions in the vicinity of a full-scale DARPA Suboff AFF-8 submarine model in self-propulsion condition.

Table 5-6 The thickness of the low-velocity regions in different attachment locations in the self-propulsion of the submarine.

	A	B	C
Top	6.984 (3325.76%)	7.116 (3388.76%)	0.539 (256.85%)
Side	0.362 (172.38%)	0.526 (250.67%)	0.392 (186.57%)
Bottom	0.370 (176.22%)	0.525 (250.03%)	0.385 (183.20%)

Figure 5-13 and Figure 5-14 presents the results of the total resistances and resistance reduction rates when the developed AUV docks to the above identified locations. The B-side achieves the highest total resistance reduction rate of 35.23%. Furthermore, all attachment locations in the B section exhibits a slightly lower total resistance compared to other sections. Combining to the comparison of boundary layer thickness shown in Table 5-6, it is consistent with the previous finding that the resistance reduction is caused by the thicker boundary layers.

Regarding the top locations of section A and B, despite their location within a large low-velocity region generated by the sail of the submarine, they do not show any significant advantage. For the C section, it doesn't show any significant resistance reduction.

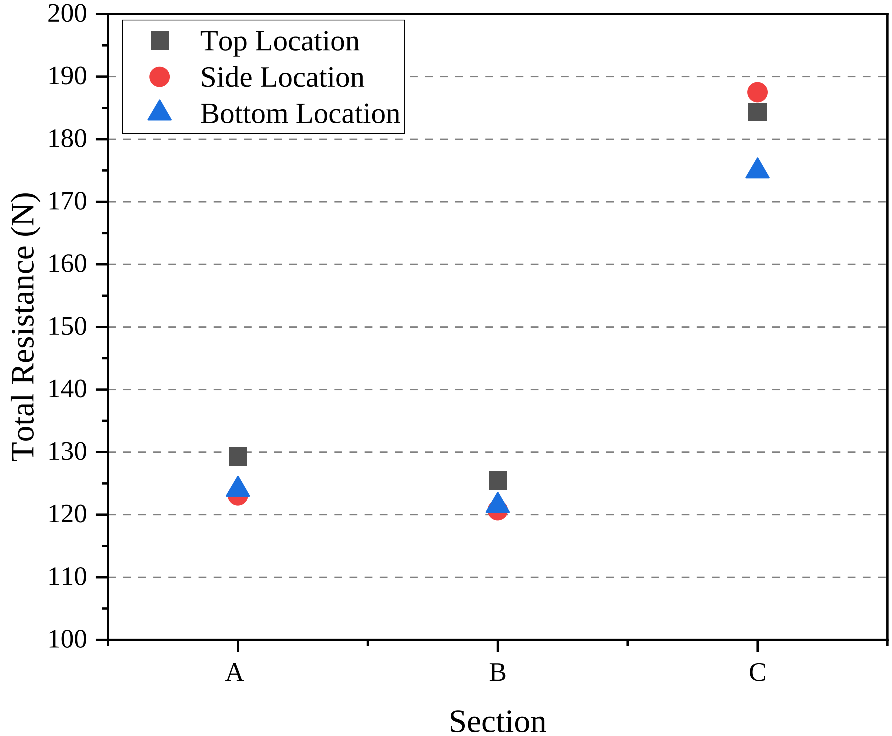

Figure 5-13 The comparison of the total resistances for different attachment locations.

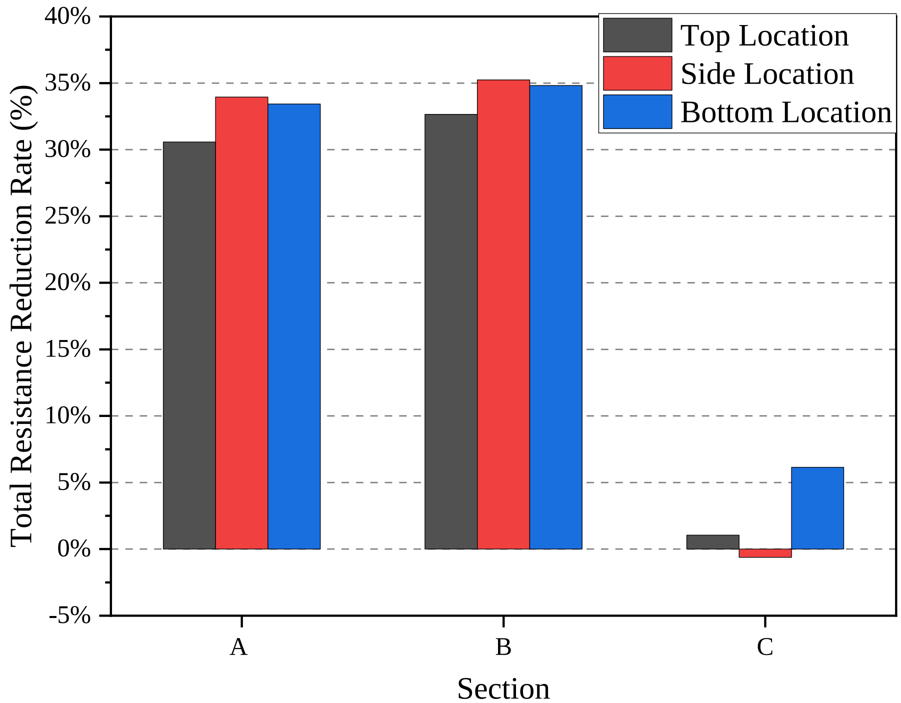

Figure 5-14 The comparison of the total resistance reduction for different attachment locations.

Furthermore, to understand the rationale of the resistance reduction, as shown in Figure 5-15 and Figure 5-16, shear and pressure components of resistance have been extracted and compared. The attachment location has less impact on the shear resistance but significant effect on the pressure resistance. The pressure resistance in the C section increased significantly due to its proximity to the stern of the submarine, where a non-negligible suction force was generated by the motion of the propeller behind the stern. Concerning the A and B sections, the reduction effects in the pressure resistance are similar, while the side and bottom locations have higher reduction than the top location.

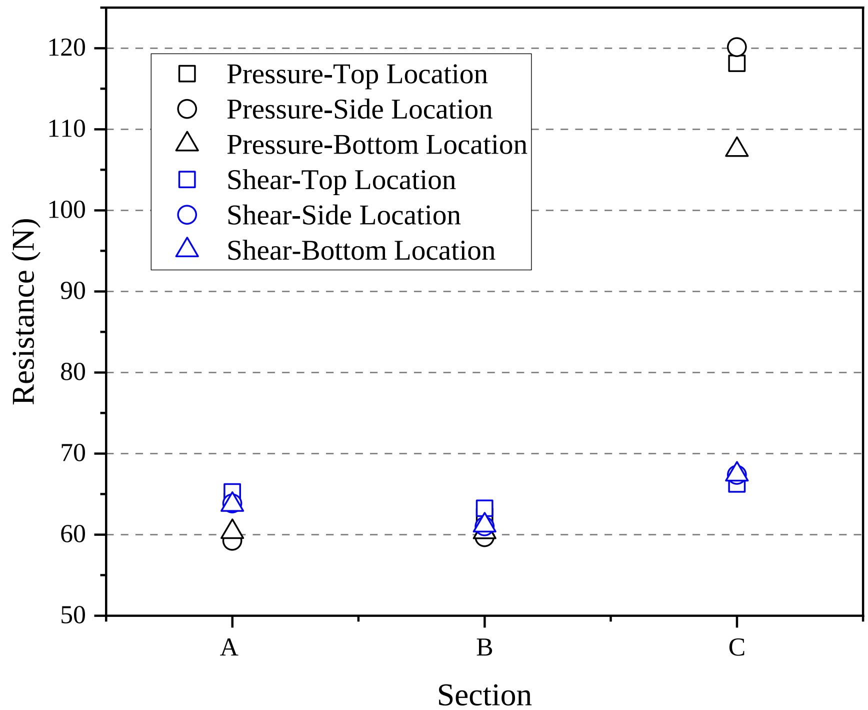

Figure 5-15 The comparison of pressure and shear resistances for different attachment locations.

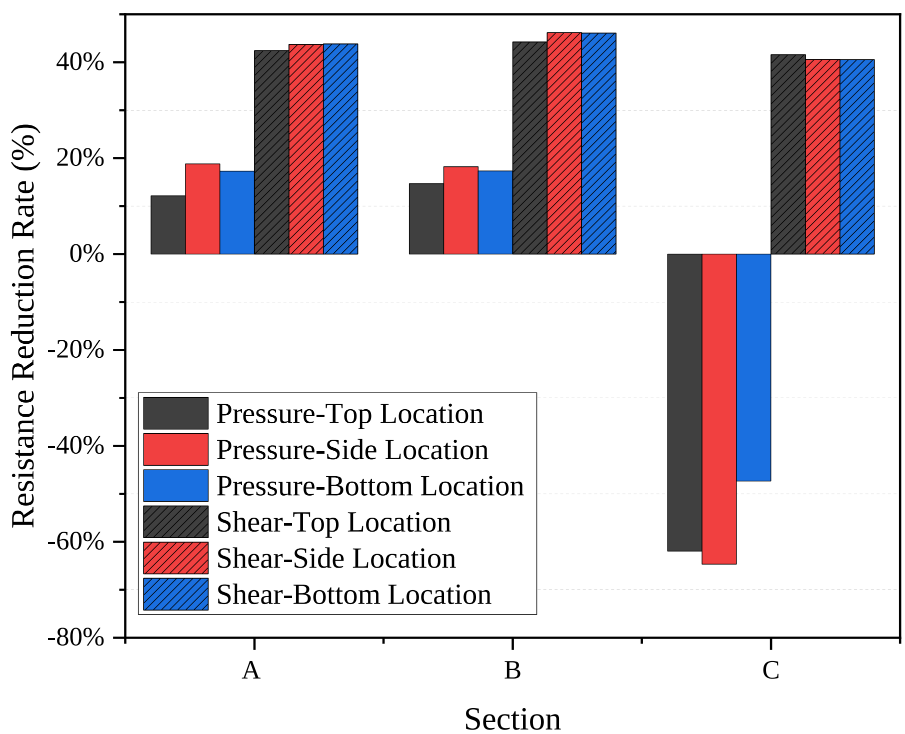

Figure 5-16 The comparison of pressure and shear resistance reduction rate.

In order to understand the resistance reduction mechanism, further detailed flow analysis has been conducted. Figure 5-17, Figure 5-18 and Figure 5-19 show the velocity contours around the remora-inspired AUV at different docking locations in sections A, B and C. As shown in Figure 5-17, at the top position, a thinner boundary layer is observed on two sides of the AUV (area 1) due to the effect of main sail. And two high-pressure regions are present on the top of the AUV hull (area 2 in Figure 5-17, with this phenomenon being more pronounced in the proximity of the sail (A section). The thickness of the boundary layer is the greatest in the B section shown in Figure 5-18, which is in agreement with the results of the submarine self-propulsion analysis. Additionally, the velocity distributions around the AUV at the side location were similar to those at the bottom locations in all sections. Furthermore, the velocity contours in the C section (Figure 5-19) demonstrate that the boundary layer is influenced as expected by the propeller, gradually thinning at all attachment locations in the C section.

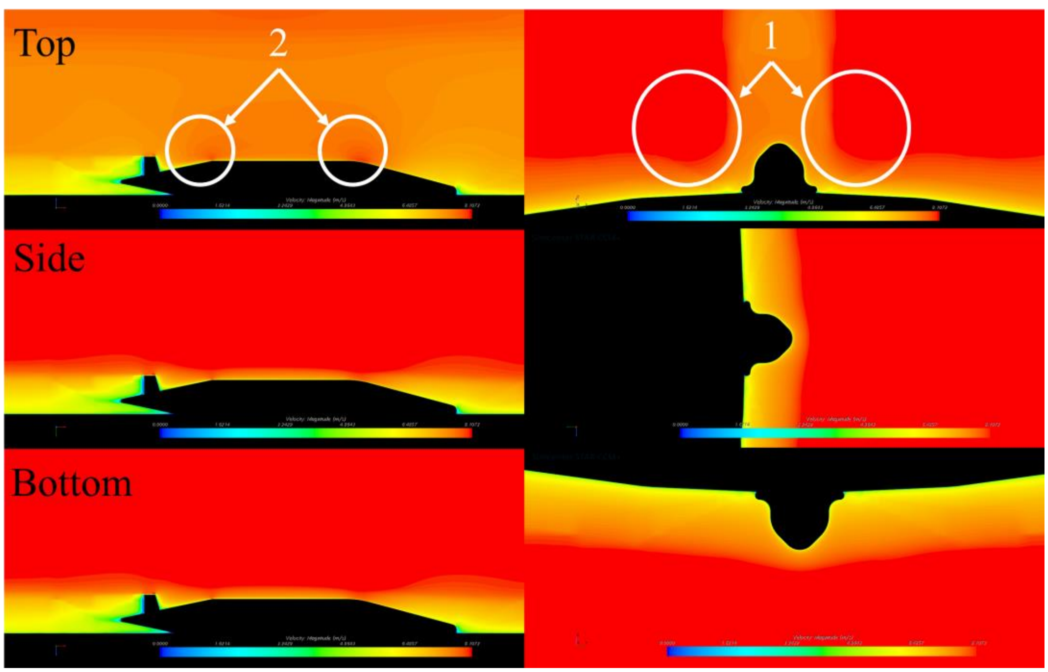

Figure 5-17 The velocity contours at three attachment locations of the A section in AUV-submarine attachment analysis simulations.

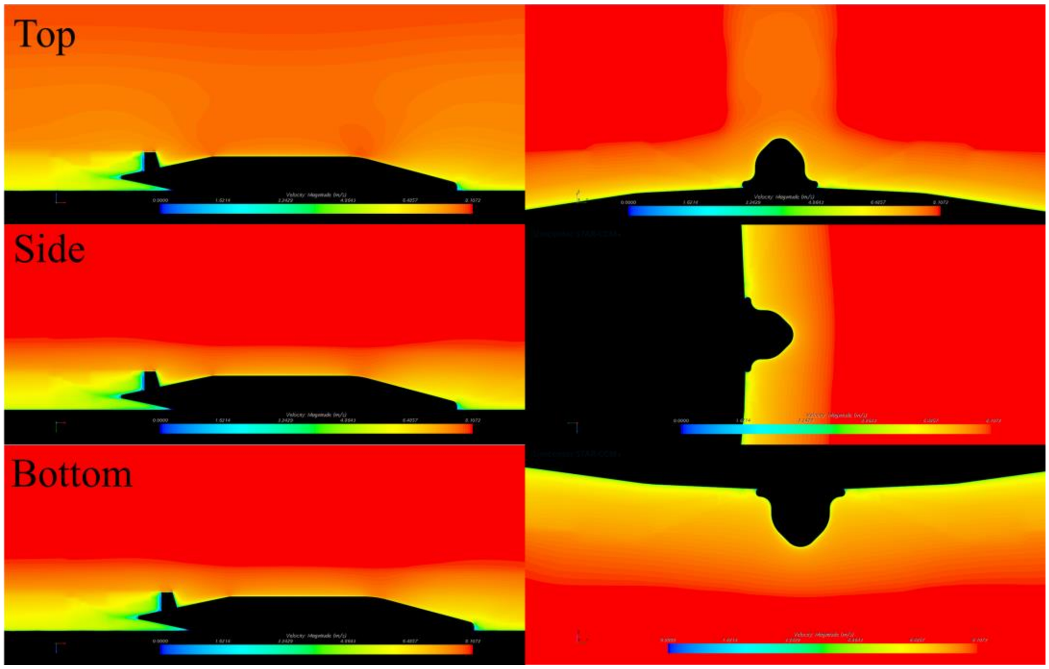

Figure 5-18 The velocity contours at three attachment locations of the B section in AUV-submarine attachment analysis simulations.

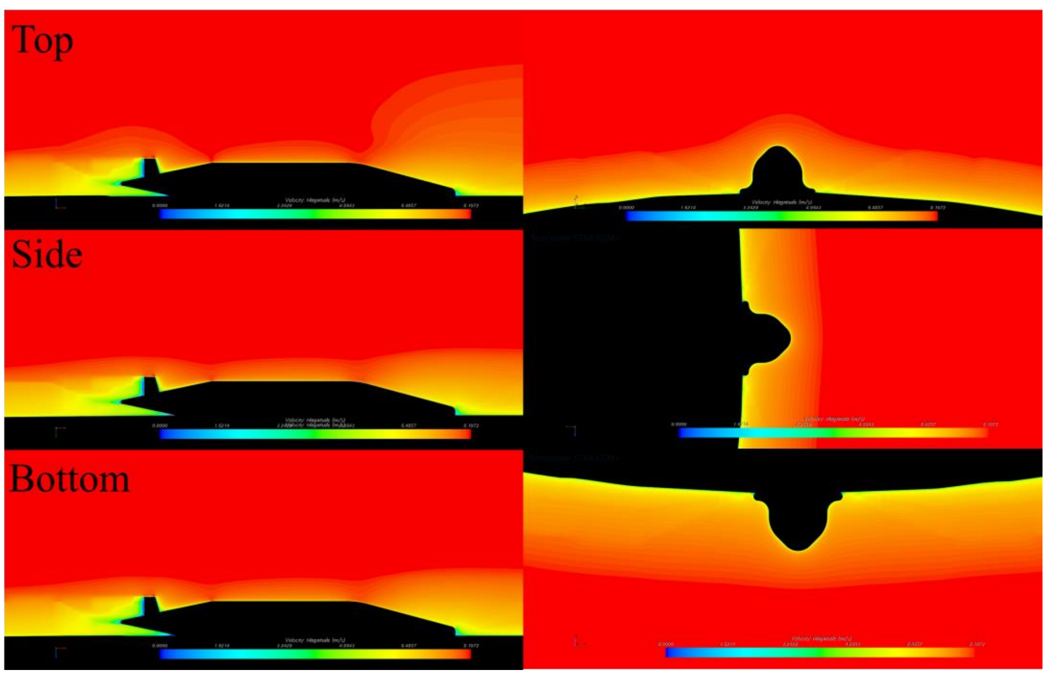

Figure 5-19 The velocity contours at three attachment locations of the C section in AUV-submarine attachment analysis simulations.

According to the above investigations, it is evident that all attachment locations in the C section are unsuitable for the AUV docking operation. This is due to the suction force generated by the motion of the propeller, which significantly increases the pressure resistance on the AUV, resulting in almost no reduction in resistance. In addition, due to the complex structure of the submarine's stern and the proximity of this docking area to the propeller, the risk of the AUV docking operation will increase.

In terms of the attachment location in the A section, a lower total resistance reduction is observed compared to the B section. It is noteworthy that although the A-top and B-top attachment locations are both located in the low-velocity region, they provide a lower total resistance reduction than the side and bottom attachment locations. There seems to be no effective adverse pressure gradient region generated behind the sail of the submarine for a remora-inspired AUV of this size. In addition, the wake behind the sail will increase the difficulty of controlling the AUV.

For the attachment locations in the B section of the submarine's middle hull, the highest total resistance reduction can be achieved at the B-side attachment location, with a reduction rate of up to 35.23%. However, the B-bottom attachment location also provides a resistance reduction effect close to that of the B-side attachment location, at 34.81%. Additionally, the B-side attachment location requires the AUV to be rotated 90 degrees for the docking operation, which increases the energy consumption and control difficulty of the AUV. Therefore, the B-bottom attachment location is considered more advantageous than other attachment locations. However, it should be noted that certain submarines can rest on the seabed conducting surveillance missions. In such operations, it is not allowed for the AUV to attach onto the submarine bottom. This specific condition must be carefully considered during the design and operation of the dynamic underwater recovery mechanism for the AUV.

b) Effect of Forward Velocity

Based on the above analysis of the attachment locations, the B-bottom attachment location is selected to investigate the effect of the advance velocity of the submarine. Five velocities were simulated in this study, namely 5.423 m/s, 4.081 m/s, 2.727 m/s, 1.769 m/s, and 1.126 m/s.

It can be seen from Figure 5-20 that the thicknesses of the boundary layers are nearly identical across this range of velocities. In addition, Figure 5-21 shows the resistance reduction rates for the AUV attached to the submarine at different velocities. As the velocity reduces, the resistance reduction of the AUV attached to the submarine increases slightly from 34.79% to 38.52%. Therefore, in terms of the resistance reduction, the effect of Reynolds number is not significant.

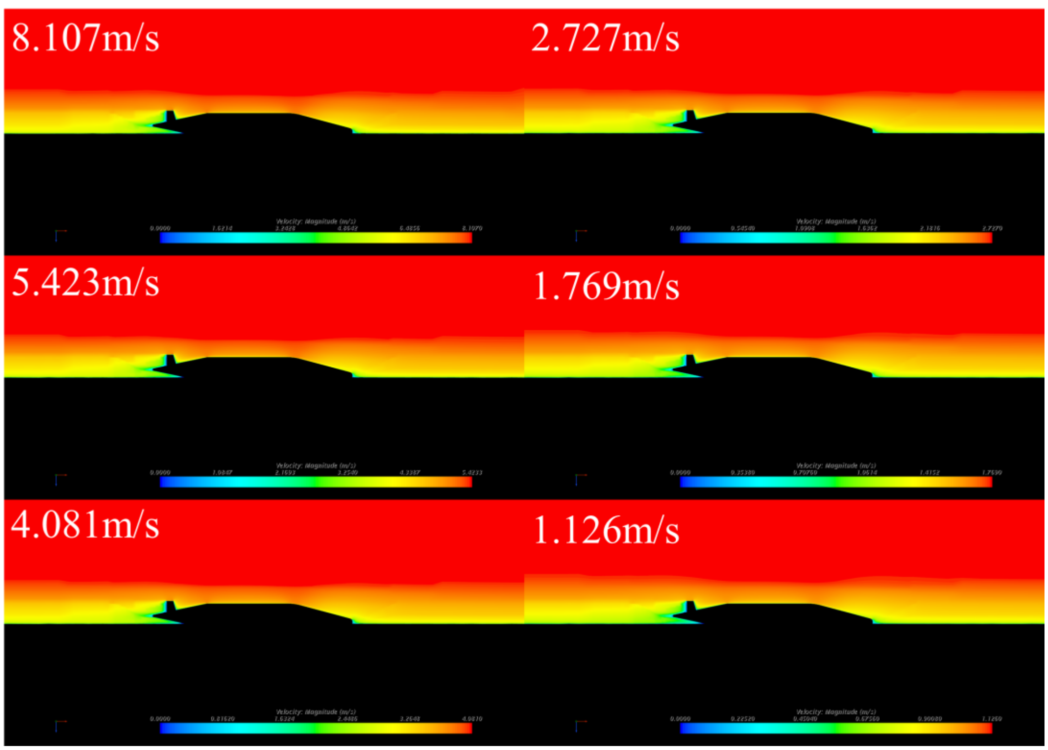

Figure 5-20 The velocity contours of AUV-submarine attachment analysis simulations when the AUV attached to the B-bottom location at various velocities.

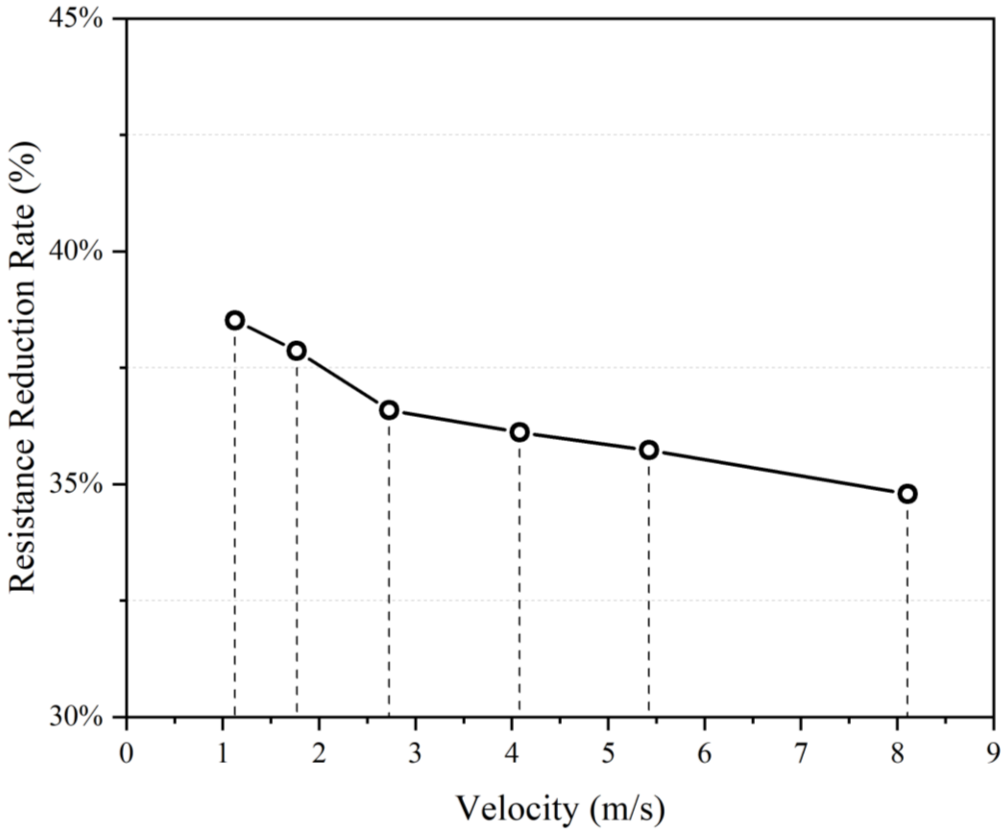

Figure 5-21 The total resistance reduction rates when the remora-inspired AUV attached to the B-bottom attachment location at different velocities.

Based on Figure 5-21, a linear relationship between the drag reduction rate and δ/H can be derived with the following 5-4 with ${R_{adj}}^2$=0.94:

$$Y = 0.3995X - 0.6016 \quad \text{5-4}$$

5-4 is derived from the linear relationship of Figure 5-22. In the figure, where X represents δ/H, which is the ratio of the height of the AUV to the thickness of the boundary layer, and Y indicates the drag reduction rate obtained from simulations. This linear relationship, alongside 3-5 and 3-8, will serve as a valuable reference for estimating the drag reduction rate in the boundary layer for future AUV designs. By leveraging these relationships, it is possible to predict how modifications to the AUV's dimensions relative to the boundary layer will affect its hydrodynamic performance and drag reduction potential.

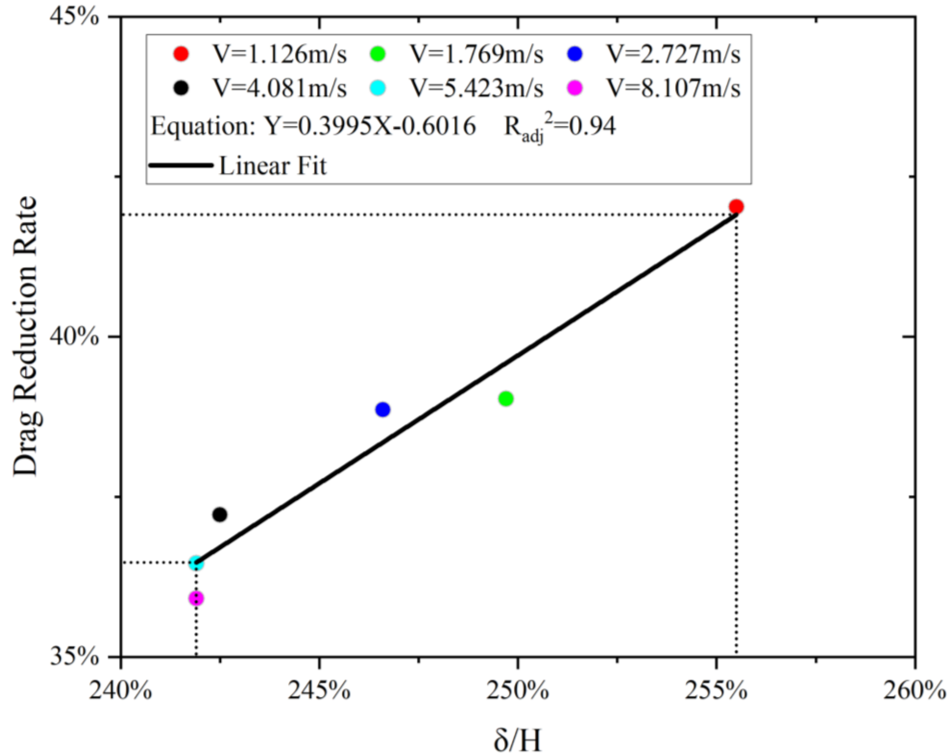

Figure 5-22 Linear fitting for the drag reduction rate versus boundary layer thickness of submarine (B-bottom location) to remora-inspired AUV height ratio.

5.6 Concluding Remarks

This chapter presents an investigation into the hydrodynamic characteristics of a remora-inspired AUV as it attaches to various locations on a full-scale self-propulsion submarine surface. Nine potential locations are examined, and the impact of the submarine’s forward velocity is also assessed. These finding provide a foundation for the subsequent chapter's analysis on the AUV docking process. The following concluding remarks can be drawn:

1) To identify the optimum docking location to the submarine, a full-scale self-propulsion submarine is simulated using CFD. 3 potential longitudinal positions with 3 potential circumferential locations have been evaluated.

2) AUV docking onto the above nine potential locations has evaluated. Combining the resistance reduction effect and the practical operational feasibility, the location at the bottom of the middle section is recommended.

3) In terms of the attachment location in the A section, lower total resistance reduction rates are observed at the side and bottom attachment locations compared to the B section. On other hand, the wake behind the sail will make the AUV more difficult to control.

4) It should be noted that while the A-top attachment locations are located in a low-velocity region, no effective adverse pressure gradian region is generated behind the sail of the submarine for the remora-inspired AUV of this design size.

5) In the C section, all of the attachment locations are impacted by the motion of the propeller. The suction force generated by the motion of the propeller significantly increases the pressure resistance on the AUV. Moreover, the complex structure of the submarine's stern and the proximity of this area to the propeller increase the risk of the AUV docking operation.

6) The remora-inspired AUV design achieves the highest total resistance reduction at the B-side attachment location, but the B-bottom attachment location offers a similar reduction in total resistance. Furthermore, the B-side attachment location requires the AUV to rotate 90 degrees during the docking operation, which increases energy consumption and control difficulty.

7) The resistance reduction of the AUV remains almost constant for velocities ranging between 1.126 m/s and 8.107 m/s, ranging from 38.52% to 34.79%.

Chapter 6

Hydrodynamics of the Remora-Inspired AUV in Approaching & Docking Process

Based on the above study, the potential docking locations have been explored for the selected self-propulsion submarine hull. After considering factors such as resistance reduction, operational complexity, and energy consumption, the B-bottom location (located on the middle of the submarine hull) can be identified as an optimal docking location. This location can provide a significant resistance reduction effect on the remora-inspired AUV due to the low-velocity around the submarine. Additionally, there's no need to adjust the AUV's attitude, and the area itself lacks intricate structures. Furthermore, simulations conducted at varying velocities indicate that the reduction rate in resistance for the remora-inspired AUV almost remains consistent regardless of the submarine's forward speed.

To further investigate the challenge when docking an AUV to the submarine, further analysis has been conducted to research the process of the docking and the forces experienced in the docking process, and an illustrative example of one such docking path is depicted in Figure 6-1. In this chapter, two types of simulations are conducted to investigate the hydrodynamic characteristics of the remora-inspired AUV during the docking process. Through these simulations, we identify the various stages of the docking process and assess the impact on the AUV when it comes into close proximity with underwater vehicles of significantly different sizes.

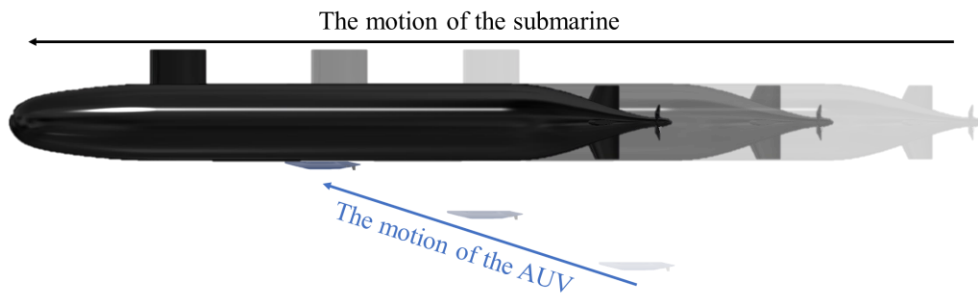

Figure 6-1 An example of the motion of the AUV and the submarine during docking operation.

In this chapter, numerical simulations were implemented using the CFD software STAR-CCM+ to investigate the hydrodynamic behaviours of the remora-inspired AUV during the docking operation. The simulations utilized a Reynolds-Averaged Navier–Stokes (RANS) model in conjunction with a K-ω Shear Stress Transport (K-ω SST) turbulence model. Most of the simulation settings align with those in chapter 5, including the models used, the domain size and the mesh generation. Further specific simulation configurations will be detailed in the subsequent sections.

In this framework, Section 6.1 presents the AUV-submarine docking analysis as the AUV's attitude is fixed. Section 6.2 introduces the AUV-submarine docking analysis with variable AUV attitude and the process when AUV are traveling to the position for starting the docking operation. After that, Section 6.3 provides a summary of the main conclusions of this chapter.

6.1 AUV-Submarine Docking Analysis with Fixed AUV Attitude

In this section, the focus is on the docking process of a remora-inspired AUV with a fixed attitude. The primary aim is to understand the hydrodynamic characteristics as the AUV approaches the submarine, with both vehicles maintaining a constant horizontal velocity. By keeping the AUV's attitude consistent, the hydrodynamic changes typically associated with attitude adjustments are eliminated. This setup provides a clearer observation of the hydrodynamic interactions between the two vehicles as they approach each other during the docking operation.

6.1.1 Numerical Methodology

The study simulates AUV moves from 2L (length of the AUV) away from the submarine to the attachment location. The B-bottom attachment location, as determined in the previous section, was chosen as the docking position. Considering the speed range of the general AUVs, a velocity of 2.727 m/s was selected as the docking velocity. The same horizontal velocity has applied to both the submarine and the AUV and then a constant vertical force presenting the additional thrust needed to dock the AUV was applied to the AUV model to drive the AUV towards the submarine. The Dynamic Fluid Body Interaction (DFBI) module was employed and only the translational motion is enabled to allow the AUV approaching and docking to the submarine while maintaining the course with the submarine illustrated in Figure 6-2. The submarine and the AUV were assumed as rigid body with no deformation when contacting. To avoid zero or negative volume cells the motion was limited to the closest 3 mm to the submarine surface and a dumping length of 1 cm was applied to model the contact.

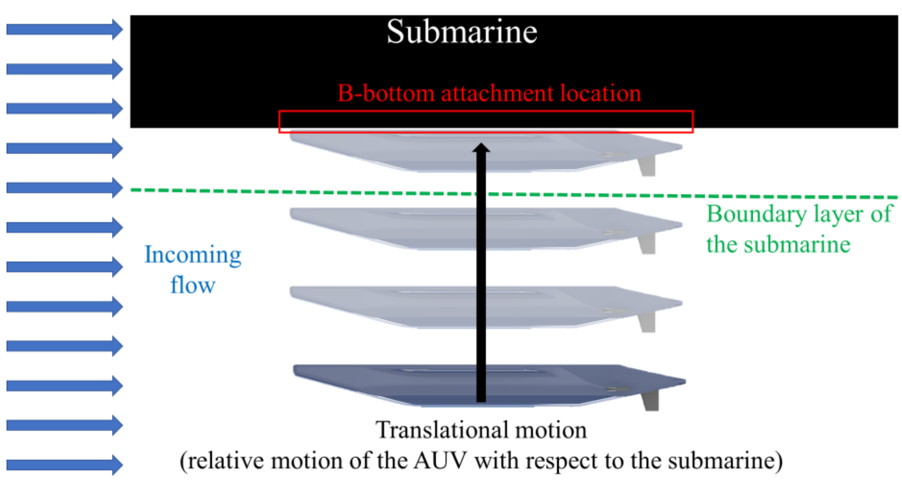

Figure 6-2 The relative motion of the AUV model with respect to the submarine model.

As depicted in Figure 6-3, the mesh surrounding the docking region was refined. An offset surface (Figure 6-4), positioned 0.05 m from the AUV model, was generated serve as an overset mesh region. In the meantime, utilizing the adaptive mesh module, the background mesh around this overset mesh region was automatically refined at each simulation step, as shown in Figure 6-5.

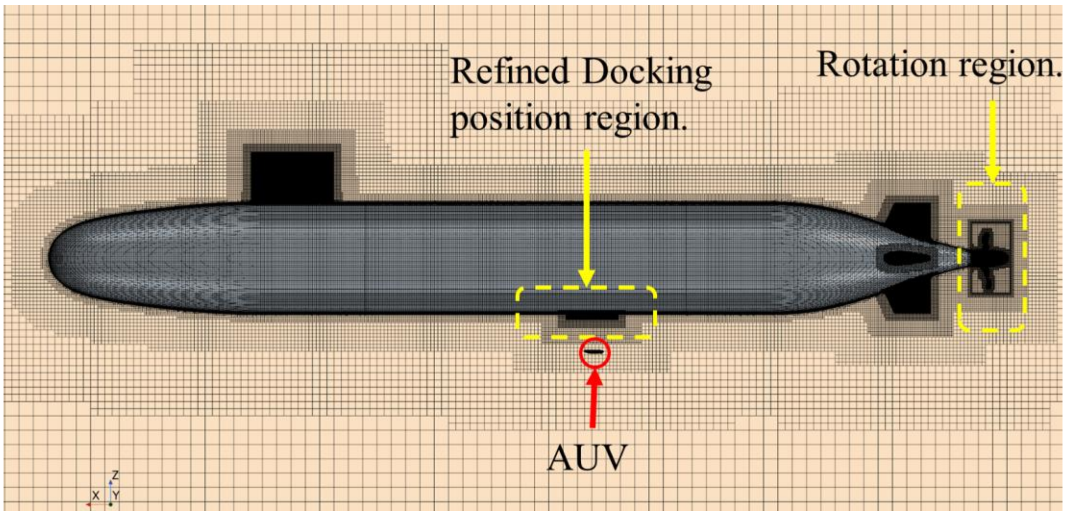

Figure 6-3 Mesh view of the submarine and the AUV.

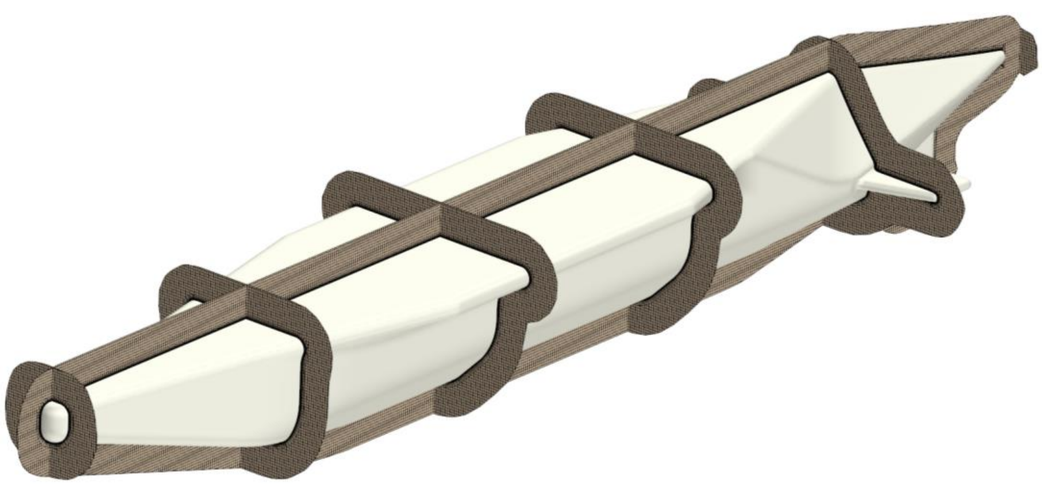

Figure 6-4 The offset surface for overset mesh.

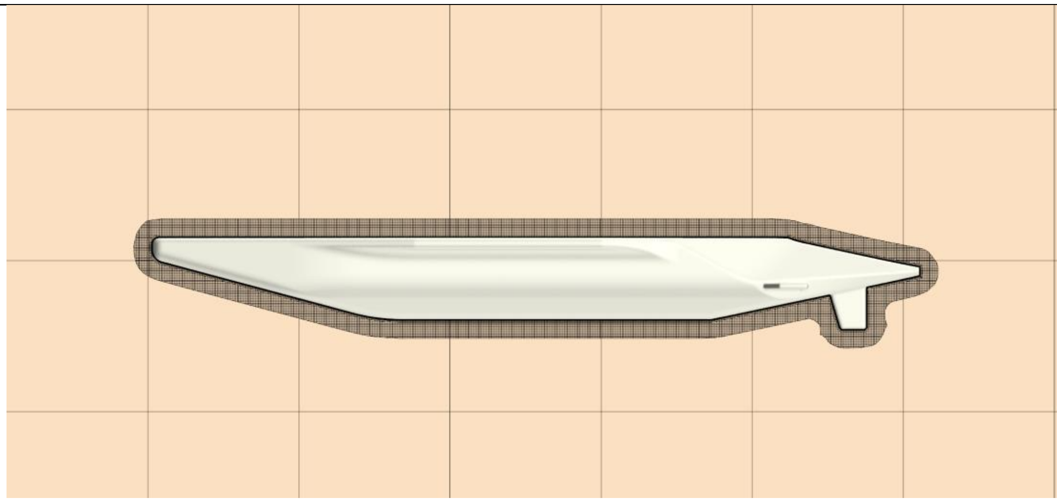

a. Initail mesh configuration without adaptive mesh.

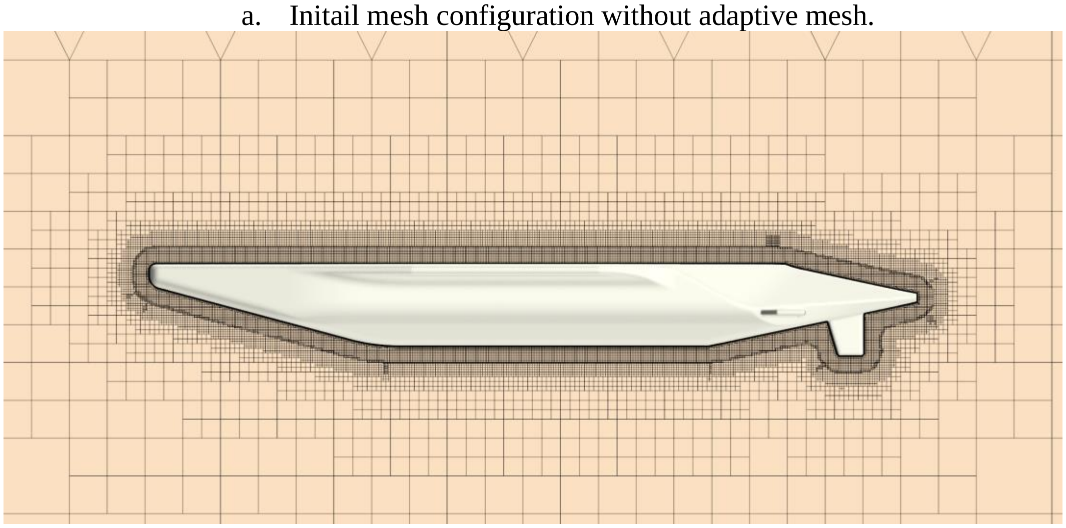

b. Mesh configuration after enabling adaptive meshing

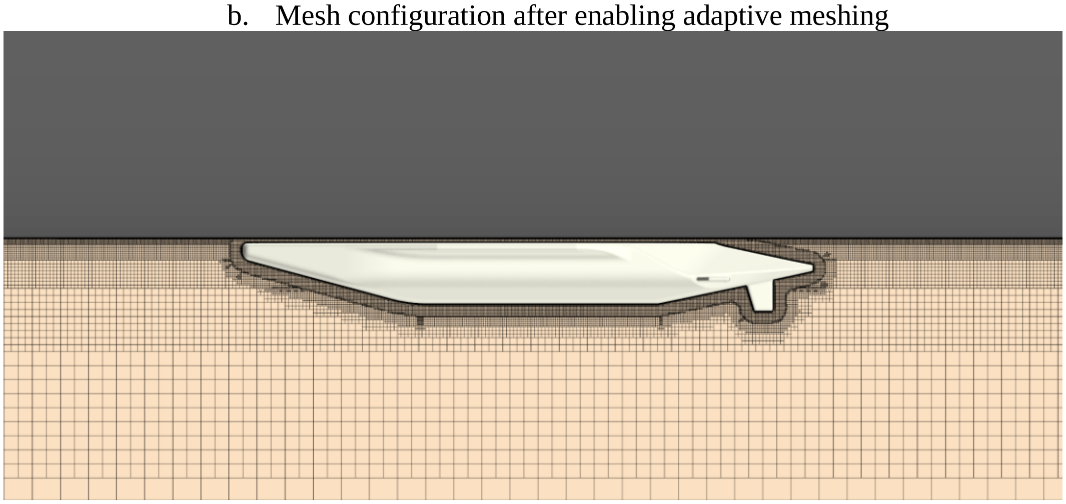

c. Mesh configuration with adaptive meshing activated as the AUV approaches the submarine.

Figure 6-5 The adaptive mesh during the simulation.

6.1.2 Stages of the Docking Operation

In this study, five different and constant vertical forces were applied: 25N, 50N, 75N, 100N and 125N. Through the numerical simulations, the study aimed to understand the variation in the hydrodynamic characteristics of the AUV as it approaches the bottom of the submarine, and the effect of the different velocities during the docking process.

In this numerical simulation, the vertical motion of the AUV model was enabled after 60 seconds, ensuring that the boundary layer of the submarine was fully developed. And Figure 6-6 shows the velocity contours during the docking process, where the flow characteristics around the AUV can be observed. When the AUV reaches the boundary layer of the submarine, the boundary layer flow of the submarine and the flow around the AUV interact. It is very interesting to notice that due to this interaction the boundary layer thickness is reduced after the AUV docks to the submarine.

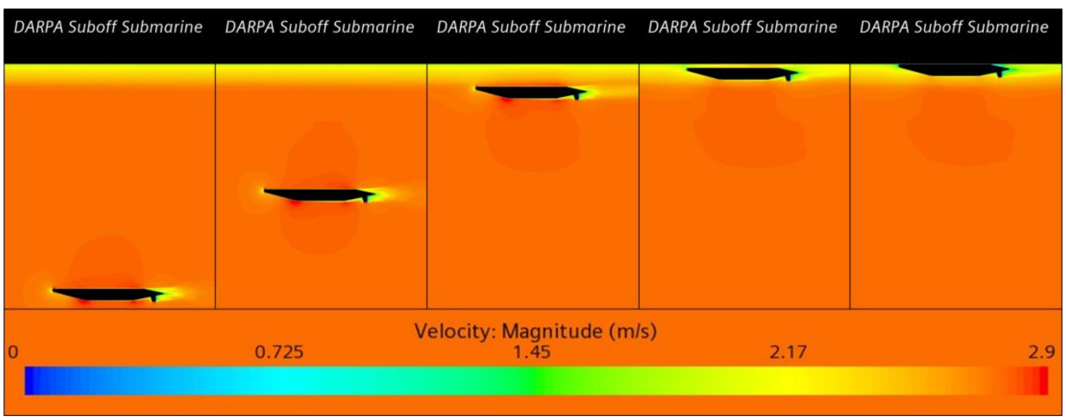

Figure 6-6 The velocity contours during the motion of the AUV.

In Figure 6-7, the resistance of the AUV is monitored through this docking process. As the AUV entered the boundary layer of the submarine, the resistance began to decrease (A in Figure 6-7). This gradual decrease is disrupted, when the AUV approaches very close to the docking position. A significant fluctuation occurred (B in Figure 6-7) with a sudden increase in resistance and a sudden decrease follows. Thereafter, the resistance continues to reduce, and finally, it reduces by 29.09% compared to the resistance in the free stream condition.

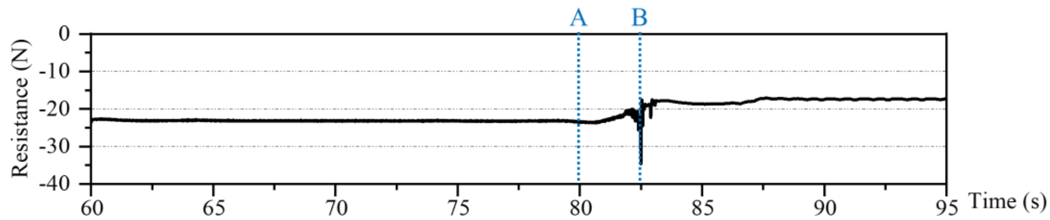

Figure 6-7 The AUV's resistance in the docking process with a constant vertical force applied.

To understand this process in detail, the force, velocity, acceleration and position were monitored in the vertical direction. Figure 6-8 shows the case driving by the constant 50N vertical force. The vertical force resulting from the fluid force, as well as the AUV vertical acceleration, velocity and displacement are illustrated. Six stages involved in the docking process can be seen as follows:

A. **Start:** The AUV started to accelerate due to the constant vertical force applied until the equilibrium state was achieved.

B. **Approach:** The AUV maintained a constant speed towards the submarine until it approached the boundary layer of the submarine.

C. **Enter:** The AUV began to enter the boundary layer of the submarine. The vertical velocity drops.

D. **Contact:** It took approximately 0.5 seconds for the AUV to reach the designated docking position after entering the boundary layer. A sudden acceleration and a contact with the submarine can be observed with velocity zeroing. An impact force can be seen, peaking at 1160.4 N.

E. **Bounce:** After the contact, as shown in the displacement plot, the AUV bounces on the submarine surface but immediately is sucked back to the surface due to the large suction force generated between the AUV and the submarine.

F. **Attach:** The small bouncing phenomenon is soon ceased and the AUV is sucked to the submarine. No more additional vertical force is needed to keep the AUV close to the submarine. A constant suction force can be observed generated by the flow, approximately at 19 N.

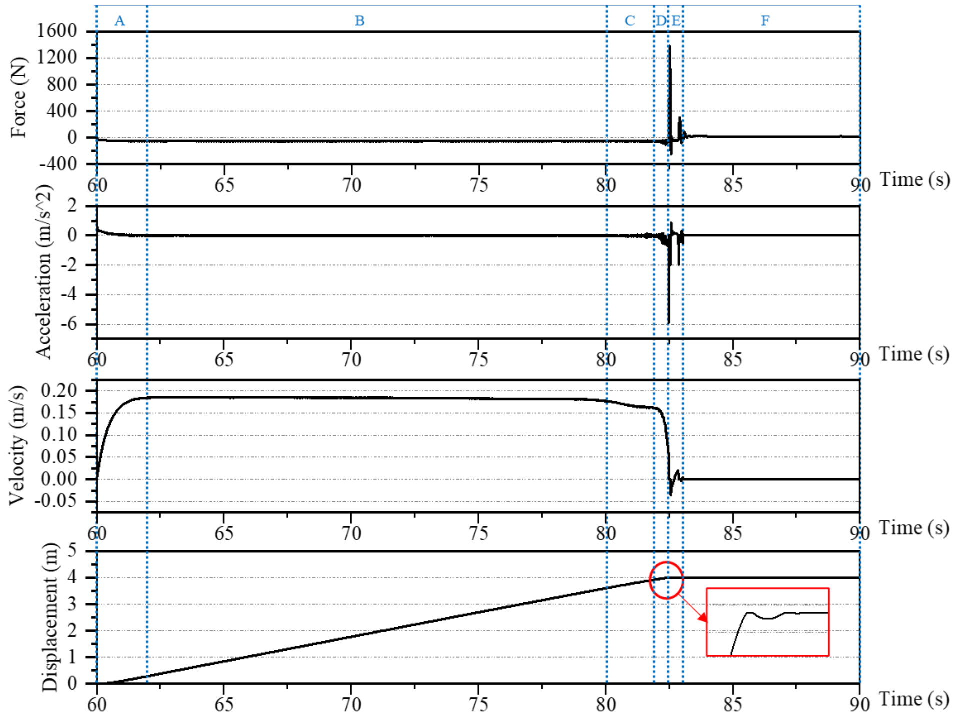

Figure 6-8 The different stages of the docking process with the 50N vertical constant force.

The above simulation shows it is feasible to drive the AUV to the submarine and attach onto the submarine surface. For the impact force, the contact area between the submarine and the AUV is 0.3 m^2, and the maximum pressure is 3868 Pa. The submarine and the AUV are not experiencing an impact force which would cause potential damages [22, 136, 137]. And after the docking, no additional vertical force is required to prevent the AUV from moving away from the submarine, as the suction force can be generated by the fluid flow.

In order to understand the minimum vertical force required, the minimum impact force and also effect of different vertical driving force, simulations were conducted under different constant vertical forces of 25N, 75N, 100N, and 125N, and the results were presented in Figure 6-9. It can be seen that the phenomena are very similar with each other under the various forces applied. The only difference observes in the study is that, during stages C and D under a constant vertical force of 25N, as marked by a blue circle in Figure 6-9 a velocity fluctuation has occurred when the AUV entered the boundary layer of the submarine. But the AUV still manages to dock to the submarine.

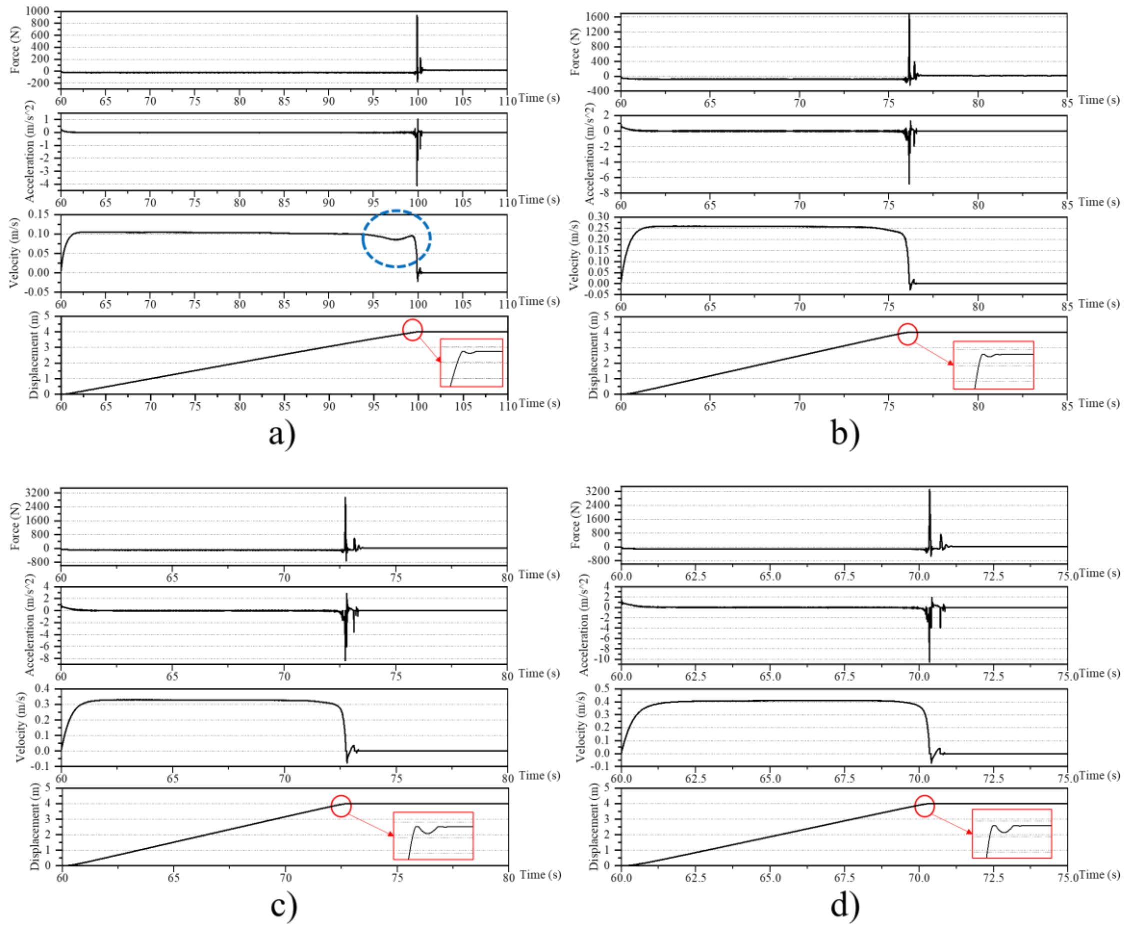

Figure 6-9 The different stages of the docking process of the remora-inspired AUV with the vertical constant forces, a) the case of 25N vertical constant force applied, b) the case of 75N vertical constant force applied, c) the case of 100N vertical constant force applied and d) the case of 125N vertical constant force applied.

As the applied force increased, the time required for docking decreased, and the impact force increased, as shown in Figure 6-10. For all cases, after the AUV reached the docking position, the fluid forces sucking it onto the submarine are all approximately 19N across all the cases.

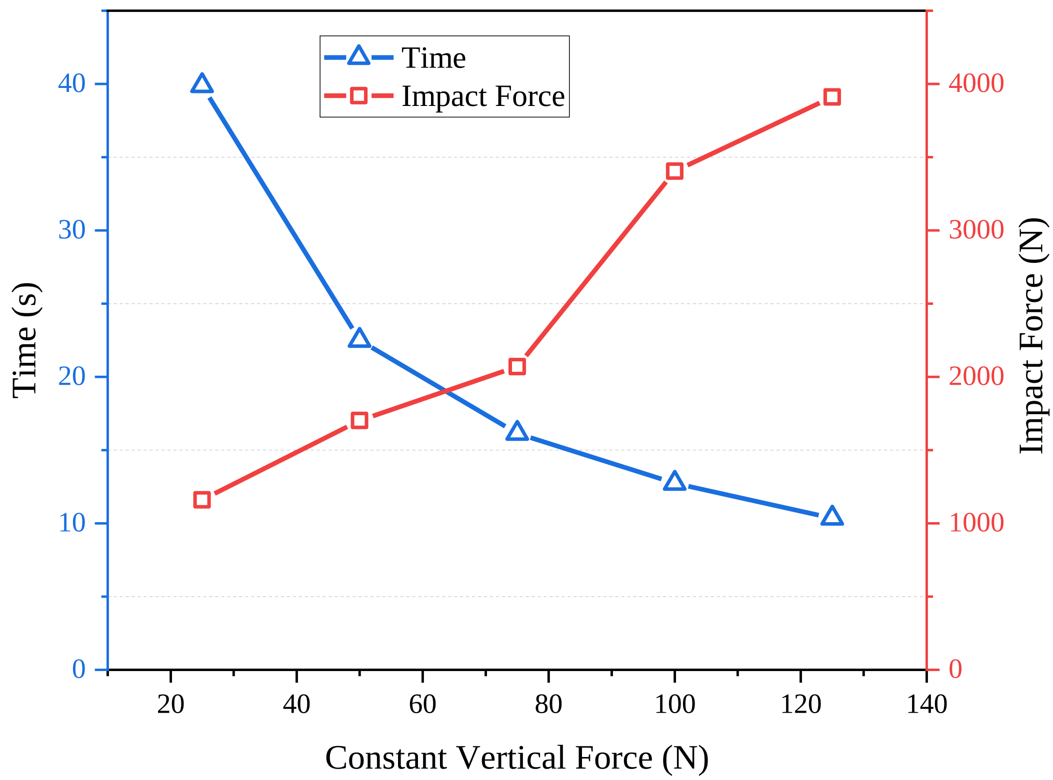

Figure 6-10 The impact forces when the AUV reached the docking position, and the time required under different vertical constant forces.

6.2 AUV-Submarine Docking Analysis with Variable AUV Attitude

Based on above investigation of the remora-inspired AUV docking onto the submarine, it shows the forces needed to dock the AUV onto the submarine. And it is numerically evidenced to be feasible to perform such operation. Following this research, further confidence has been gained.

This section presents a further investigation of three potential docking paths for the remora-inspired AUV, to explore the hydrodynamic features exhibited throughout the docking process with free motion and fully-coupled fluid and body motions. Additionally, other simulations are conducted to investigate the preparatory process when the AUV travels to the position for starting the approach process.

6.2.1 Introduction to the Dynamic Recovery Paths

To investigate the hydrodynamic characteristics when docking an remora-inspired AUV to the submarine, this section conducts simulations to explore the hydrodynamic features of the remora-inspired AUV docking to the submarine through three potential paths as the Figure 6-11, including the capture-type path (blue), the chase-type path (green)and the approaching-type path (red). It is worth noting that the AUV in the figures (Figure 6-11, Figure 6-12, Figure 6-13 and Figure 6-14) has been enlarged for better visualization as the dimensions of the AUV and the submarine are significantly different.

In the capture-type path, the AUV starts in front of the submarine. As the recovery operation begins, the AUV reduces its speed, allowing the submarine to approach from behind. When the submarine reaches a position above the AUV, the AUV initiates its approach operation. In the chase-type path, the AUV begins behind the submarine, chasing it from the rear. Once the AUV reaches the submarine's bottom side, it starts its approach. In the approaching-type path, the AUV approaches the submarine from the bottom side.

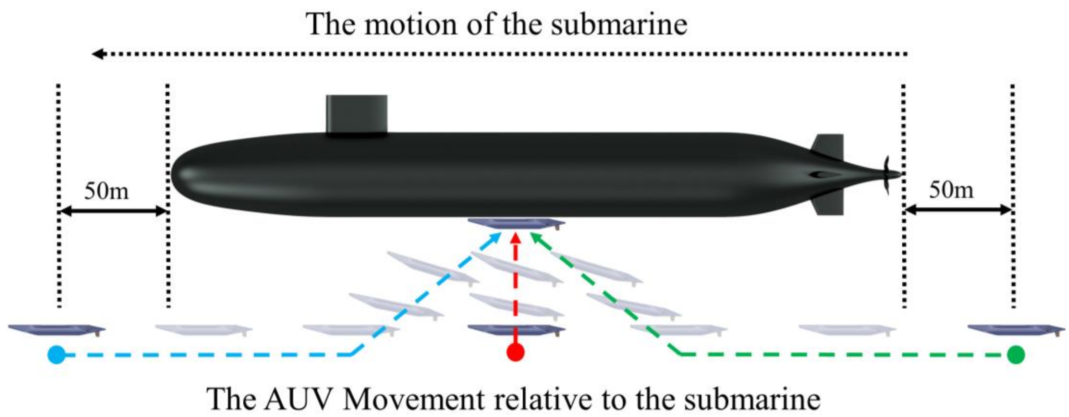

Figure 6-11 Three designed paths of docking operation for a remora-inspired AUV.

For all three paths, the docking operation can be divided into two processes: the preparatory process and the approaching process. Throughout both processes, the submarine maintains its self-propelled state. During the preparatory process, the AUV travels to a predefined position, signalling the initiation of the approaching phase where the AUV begins its approach towards the submarine. The primary difference in these three paths lies in the initial velocity during the approaching process. In the approaching-type path, the initial velocity of the approaching process is set to be the same as the submarine’s velocity. For the capture-type path and chase-type path, the initial velocity of the remora-inspired AUV is higher and lower than the submarine’s velocity, respectively. The subsequent sections detail the procedures for each of the three designed paths. Please note the forces and speeds mentioned below are specific to the performed case study.

a) Approaching-Type Path

In the approaching-type path (Figure 6-12), since the AUV starts positioned alongside the submarine, there's no need for a preparatory process. Initially, both the AUV and the submarine maintain a steady velocity of 1.126 m/s. A constant vertical force of 10N is applied near the AUV's centre of gravity in its local coordinates, guiding the AUV towards the submarine. This force is aligned vertically within the global coordinate system. Concurrently, a thrust of 4.5N is exerted at the AUV's stern, propelling it forward in its local coordinate system.

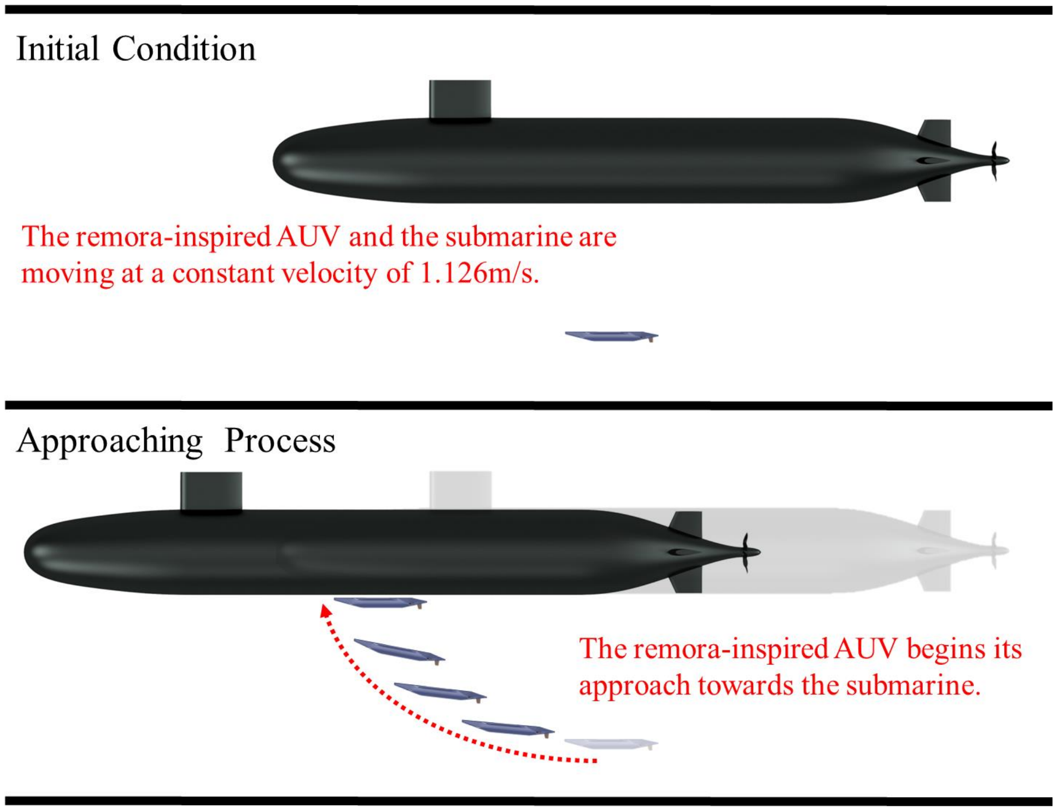

Figure 6-12 The approaching-type path of the docking operation.

b) Capture-Type Path

In the capture-type path, as Figure 6-13 shows, the remora-inspired AUV initially positions itself 50 meters ahead of the submarine at the beginning. Both the AUV and the submarine are travelling at a constant speed of 1.126m/s. In the preparatory process, the AUV ceases its thrust and begins decelerating until it reaches a predetermined location where its velocity nears zero. Concurrently, the submarine continues its course, passing the decelerating AUV. Subsequently, the docking operation transitions into the approaching process. A consistent vertical force of 10N is exerted near the AUV's centre of gravity in local coordinates, guiding the AUV towards the submarine.

This force acts vertically in the global coordinate system. Additionally, a sustained thrust of 4.5N is applied to the AUV's stern, advancing the AUV forward in its local coordinate, and aligning its final velocity with that of the submarine.

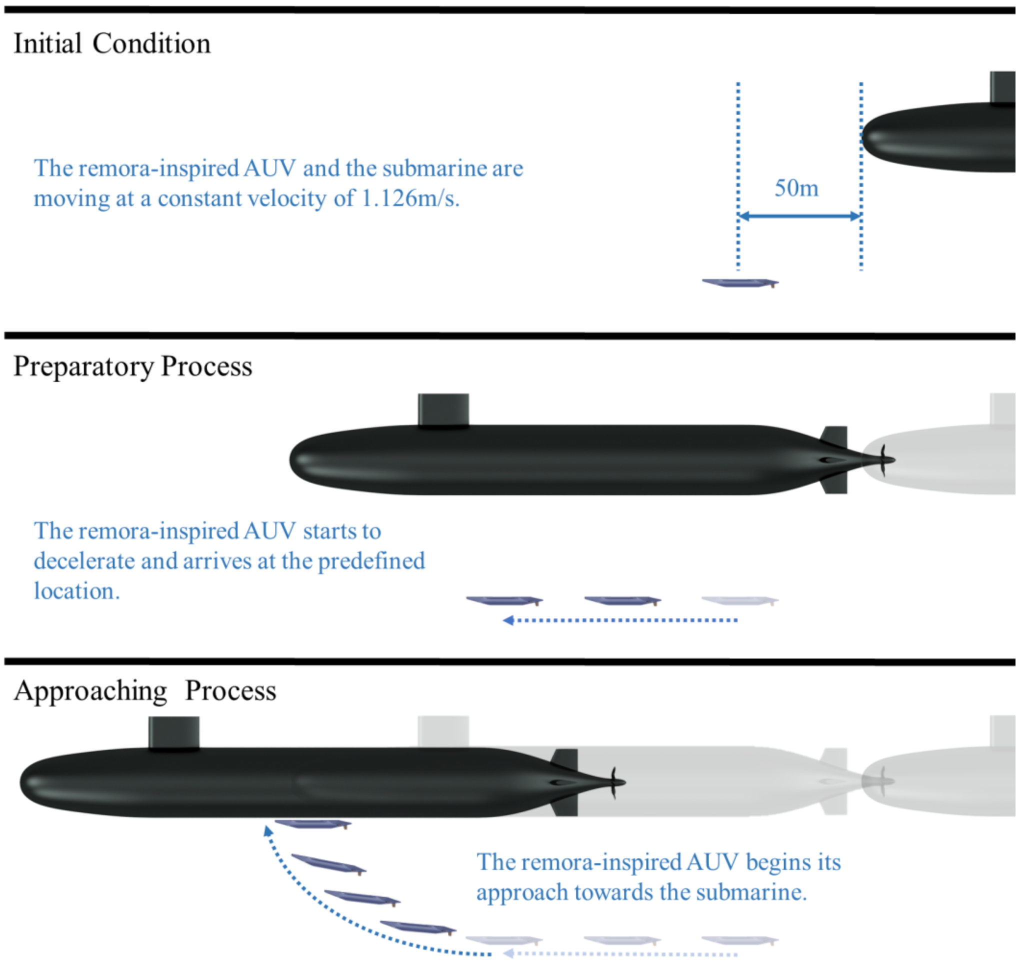

Figure 6-13 The capture-type path of the docking operation.

c) Chase-Type Path

In terms of the chase-type path, illustrated in Figure 6-14, the remora-inspired AUV initially situates itself 50 meters behind the submarine at the beginning. Both the AUV and the submarine maintain a constant speed of 1.126m/s. During the preparatory process, the AUV increases its thrust to 15N, initiating acceleration until it reaches a predetermined location. After that, during the approaching process, a consistent vertical force of 10N is similarly applied near the AUV's centre of gravity in local coordinates, directing the AUV towards the submarine. This force aligns vertically within the global coordinate framework. Meanwhile, the thrust is reduced to 4.5N, consistent with the previous case.

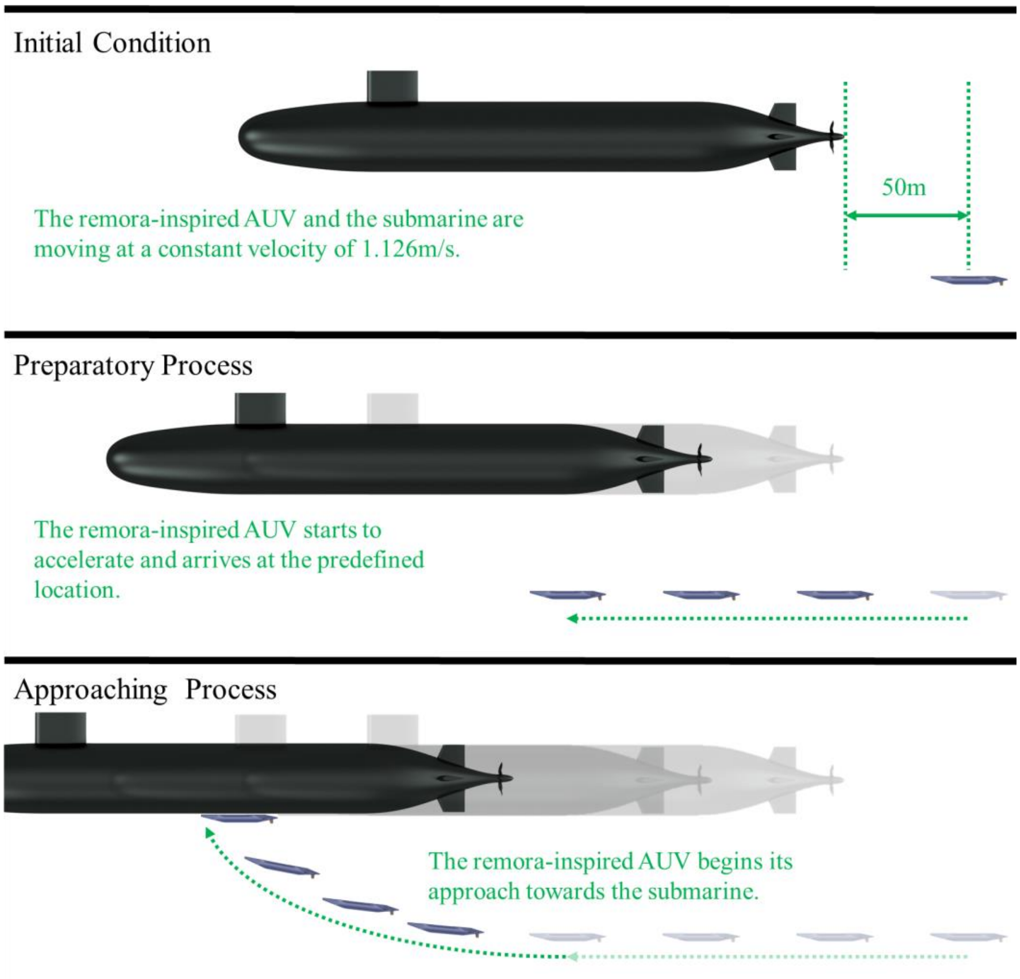

Figure 6-14 The chase-type path of the docking operation.

6.2.2 Motion Condition and Dynamic Fluid Body Interaction Module

In this simulation, the boundary conditions of the computational domain and mesh conditions were mostly consistent with the simulations in section 6.1. An offset surface was utilized to act as an overset mesh region, and the adaptive mesh module was employed to refine the background mesh at each simulation step.

The submarine was set to a self-propulsion condition, moving at a velocity of 1.126 m/s. Similarly, the initial velocities for the AUV were set consistently at 1.126 m/s across various docking paths. This uniformity in initial velocities ensures a consistent starting point for analysing the interactions and dynamics between the AUV and the submarine during the docking process. In all numerical simulations, the motion of the AUV model was enabled after 120 seconds, ensuring that the boundary layer of the submarine was fully developed.

The Dynamic Fluid Body Interaction (DFBI) module was utilized, and three motions were enabled: surge, heave, and pitch, allowing the AUV to approach the submarine and the change of the AUV's attitude, which is shown in Figure 6-15. In all simulations, the initial position of the remora-like AUV is at a vertical distance of 2L (AUV length) from the submarine. The submarine and the AUV were assumed as rigid body with no deformation upon contact. To avoid zero or negative volume cells the contact coupling model available in the STAR-CCM+ software was employed. This model applies a contact force that varies based on the distance between the boundaries of the two rigid bodies. Specifically, if the distance between the AUV and the submarine boundaries is smaller than an effective range, set at 2 cm, a repulsive contact force is initiated. The contact force decreases to zero when the distance is larger than this effective range. In accordance with the STAR-CCM+ guideline [116], the relevant parameters were defined using equation 6-1 and 6-2.

$$k = \frac{m_1 \times m_2}{m_1 + m_2} \times \frac{1}{A} \times \frac{v}{(d_0 - d_{min})^2}, \qquad 6\text{-}1$$

Where k is the estimate elastic coefficient; m_1, m_2 denote the messes of the AUV and submarine; A is the estimated area of contact; v is the normal relative impact velocity of the two coupled objects; d_0 is the effective range; and d_{min} is the minimum distance. The body should stop before this distance is reached.

$$t = \frac{\pi}{2} \sqrt{\frac{m_1 \times m_2}{(m_1 + m_2) \times A \times k}}, \qquad 6\text{-}2$$

Where t is estimated time required for stopping the body by applying the contact force.

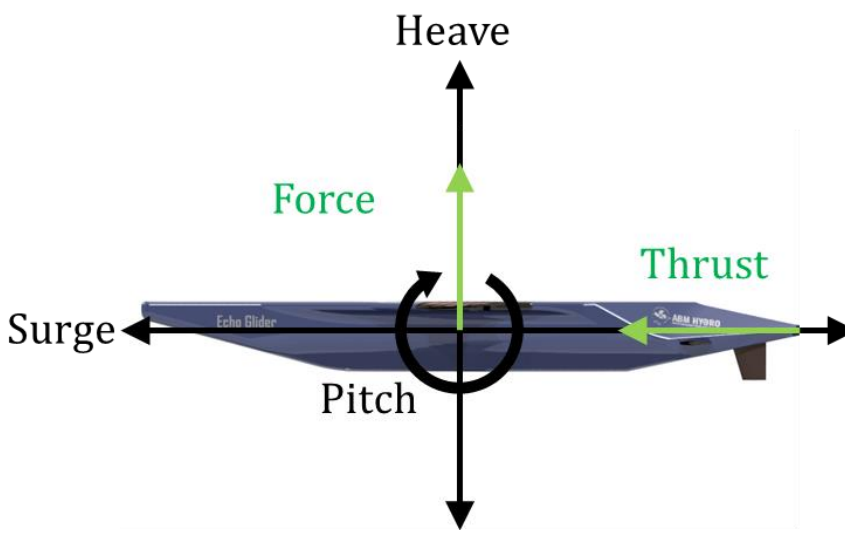

Figure 6-15 The additional force applied on the AUV.

6.2.3 Result Analysis of the Approaching-Type Path

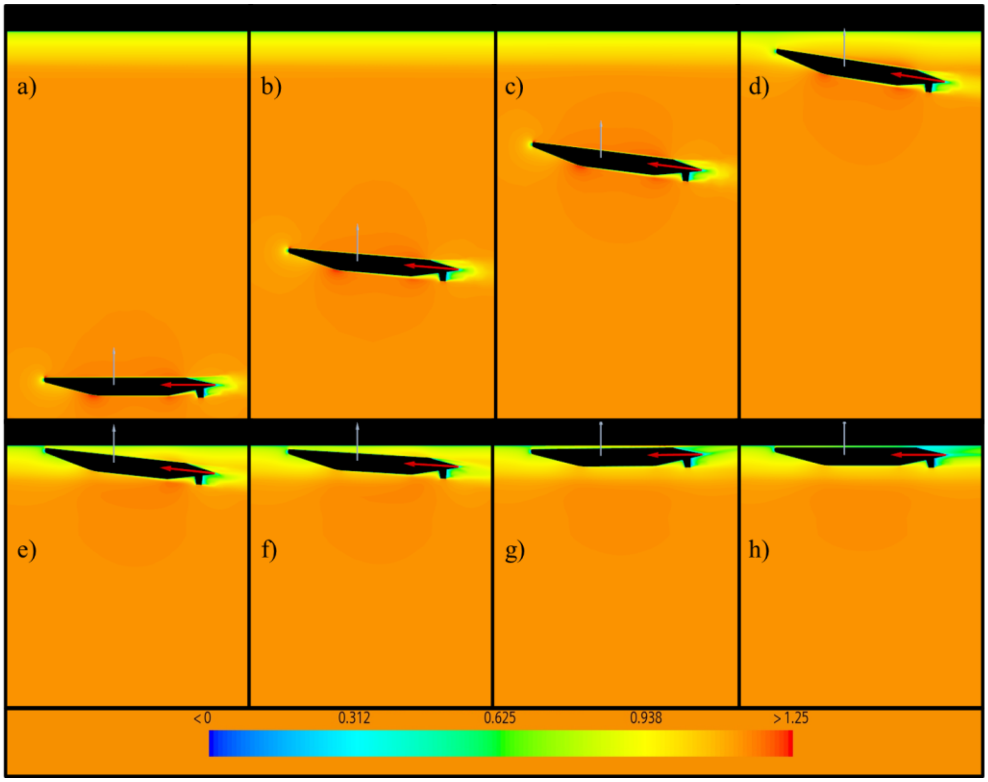

Figure 6-16 The velocity contours during the approaching process of approaching-type path.

The velocity contours during the approaching process of the approaching-type path are depicted in Figure 6-16, allowing observation of the AUV's attitude change and flow characteristics around it. Until the AUV reached the submarine's boundary layer, the pitch angle increased due to the upward force. After the AUV entered the submarine's boundary layer, the pitch angle decreased due to the influence of the boundary layer. As illustrated in the Figure 6-16 e) ~ h), several contacts occurred until the AUV stabilized in the docking region.

To understand the approaching process in detail, the vertical fluid force, pitch angle, resistance, AUV velocity and vertical velocity were monitored. As illustrated in Figure 6-17 and Figure 6-18, until the AUV reaches the boundary layer of the submarine (A-B), both the pitch angle and vertical velocity gradually increase. In the initial 2.5 seconds, there are higher accelerations for both, followed by a reduction. After entering the boundary layer (B-C), it can be observed that both vertical velocity and the pitch angle drop due to the influence of the boundary layer. Once the AUV reaches the designated docking region (C point), the vertical velocity drops rapidly. In the meantime, because the AUV's bow contact the docking region first, a moment generated by it causes the AUV to rotate counterclockwise until the AUV's stern reaches the docking region. Before the AUV become stable, several small bounces occur between the time from D to F.

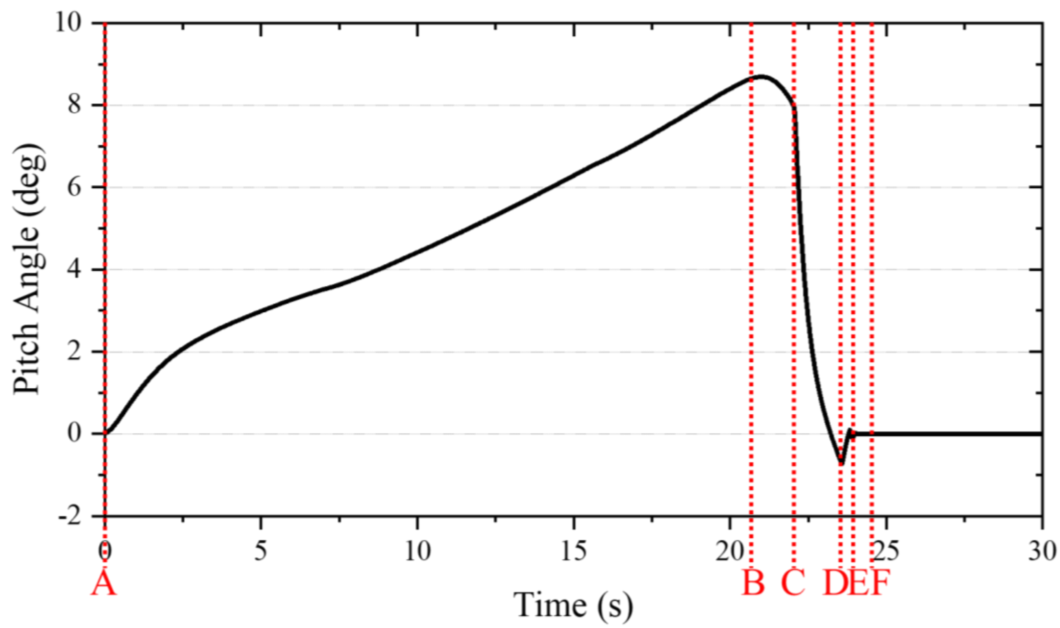

Figure 6-17 The pitch angle of the AUV during the approaching process of the approaching-type path.

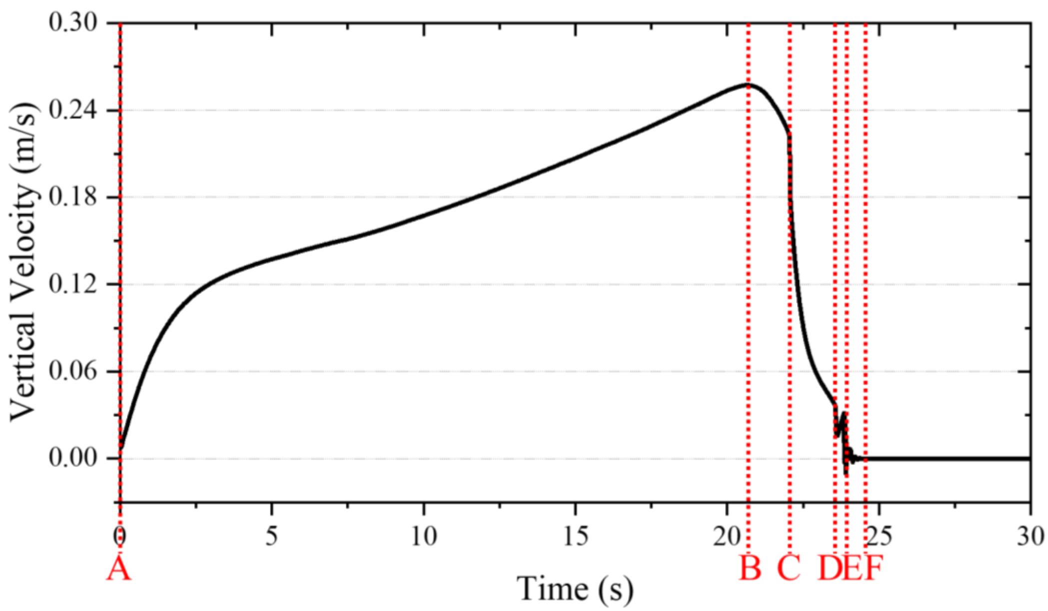

Figure 6-18 The vertical velocity of the AUV during the approaching process of the approaching-type path

To further investigate the collision details during the approaching process, the vertical fluid force on the AUV is extracted in Figure 6-19. It reveals three main contacts between C to F. The first contact (C point) occurs at the AUV's bow, and the second (D point) and third (E point) times are both at the AUV's stern. After these three main contacts, there are several slight collisions on both the bow and stern of the AUV. The impact forces of the three main contacts peak at 239.664N, 141.919N, and 425.538N, respectively. According to other researches [22, 85, 136, 137], those impact forces are not expected to cause potential damages to the AUV, as demonstrated in a collision test conducted by Meng, et al. [85]. The AUV, with a length of 2.695m, experienced maximum collision forces of 279N, 509N, and 790N at collision velocities of 0.15m/s, 0.25m/s, and 0.35m/s, respectively. After docking, a force of 3.081N generated by the fluid flow suction the AUV towards the submarine. The suction force increased with the increased forward velocities of the submarine and the AUV.

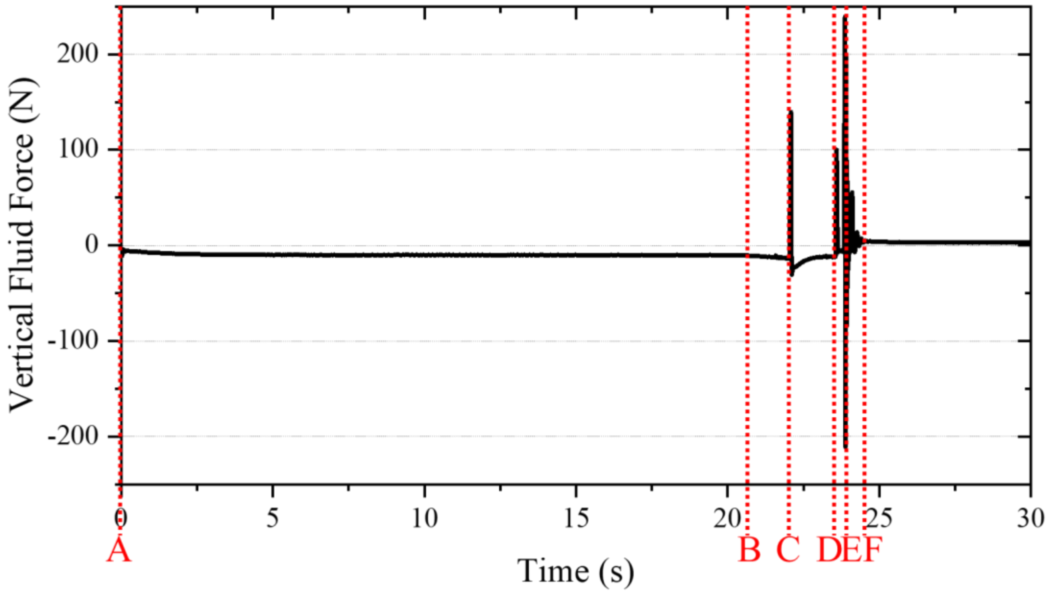

Figure 6-19 The vertical fluid force of the AUV during the approaching process of the approaching-type path

In term of the AUV velocity, as shown in Figure 6-20, during the ascending stage, the velocity increases slowly. When the AUV enters the boundary layer of the submarine, the AUV velocity remain almost unchanged. In the first contact, the AUV velocity is suddenly reduced and then gradually decreases until the AUV attaches to the submarine. In the meantime, as depicted in Figure 6-21, the AUV resistance exhibits a similar trend, with greater fluctuations due to the effects of the three primary contacts. After the AUV attaches to the submarine, the resistance decreased due to the boundary layer effect, and the velocity starts to rise. This phenomenon aligns with expectations, resulting in a 20.062% reduction in resistance.

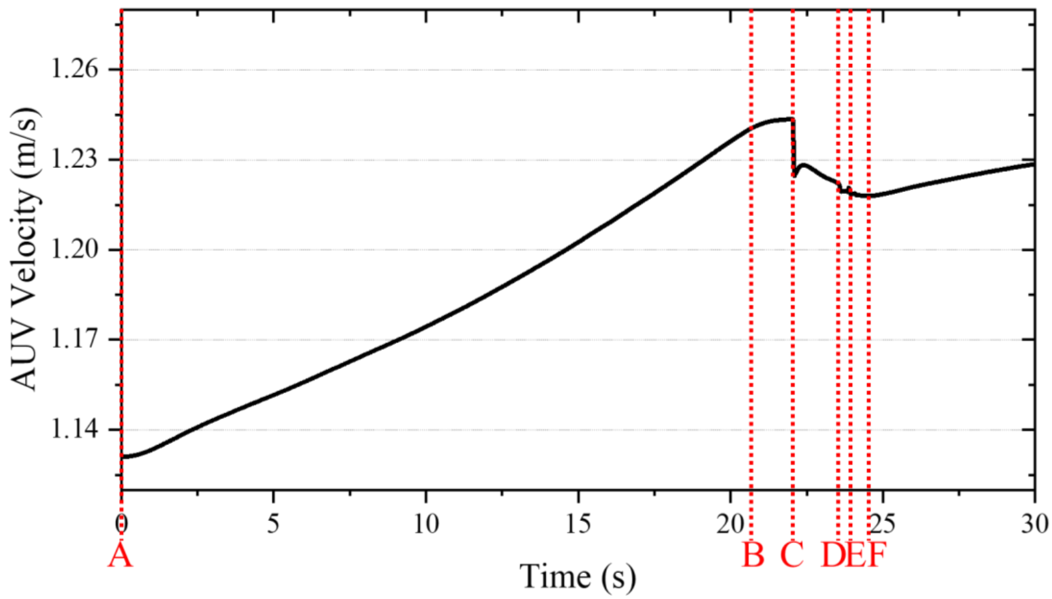

Figure 6-20 The AUV velocity during the approaching process of the approaching-type path

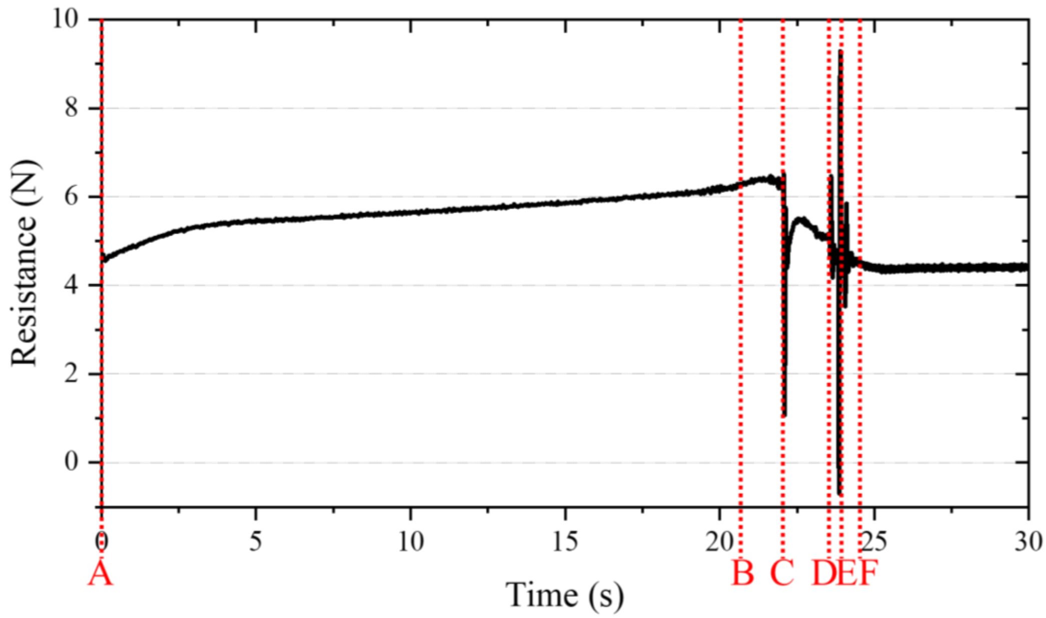

Figure 6-21 The resistance of AUV during the approaching process of approaching-type path

In summary, the approaching process of the approaching-type path can be divided into five stages:

1. **Approach (A~B):** The AUV accelerates toward the submarine due to applied forces and an increase in pitch motion.
2. **Enter (B~C):** The AUV enters the boundary layer of the submarine, experiencing a reduction in both vertical velocity and pitch angle.
3. **Contact (C~E):** Taking approximately 1.5 seconds, the AUV reaches the designated docking position after entering the boundary layer. This stage involves three main contacts: the first on the AUV's bow and the second and third on the AUV's stern. The impact forces peak at 239.664 N, 141.919 N, and 425.538 N, respectively.
4. **Bounces (E~F):** The AUV slightly bounces on the submarine surface several times, and this bouncing phenomenon quickly ceases.
5. **Attach (after F):** The AUV is drawn toward the submarine by a suction force generated by the flow. Additionally, there was a 20% reduction in resistance, further minimizing the force required to capture the AUV.

6.2.4 Result Analysis of the Capture-Type Path

a) Preparatory Process in the Capture-Type Path

Figure 6-22 illustrates the forces acting on the AUV, along with its velocity, during this preparatory phase, while Figure 6-23 displays the velocity contours as the AUV progresses through the preparatory phase in the capture-type path. As depicted in Figure 6-22, the velocity, resistance, and lift of the remora-inspired AUV experience a notable reduction initially during the preparatory process of the capture-type path, following the removal of thrust. This behaviour is influenced by the high-pressure region around the submarine's bow, as illustrated in Figure 6-23. Close to the bow, fluctuations in both velocity and resistance are evident, accompanied by a pronounced reduction in lift. The affected region spans approximately 25m both ahead of and behind the bow.

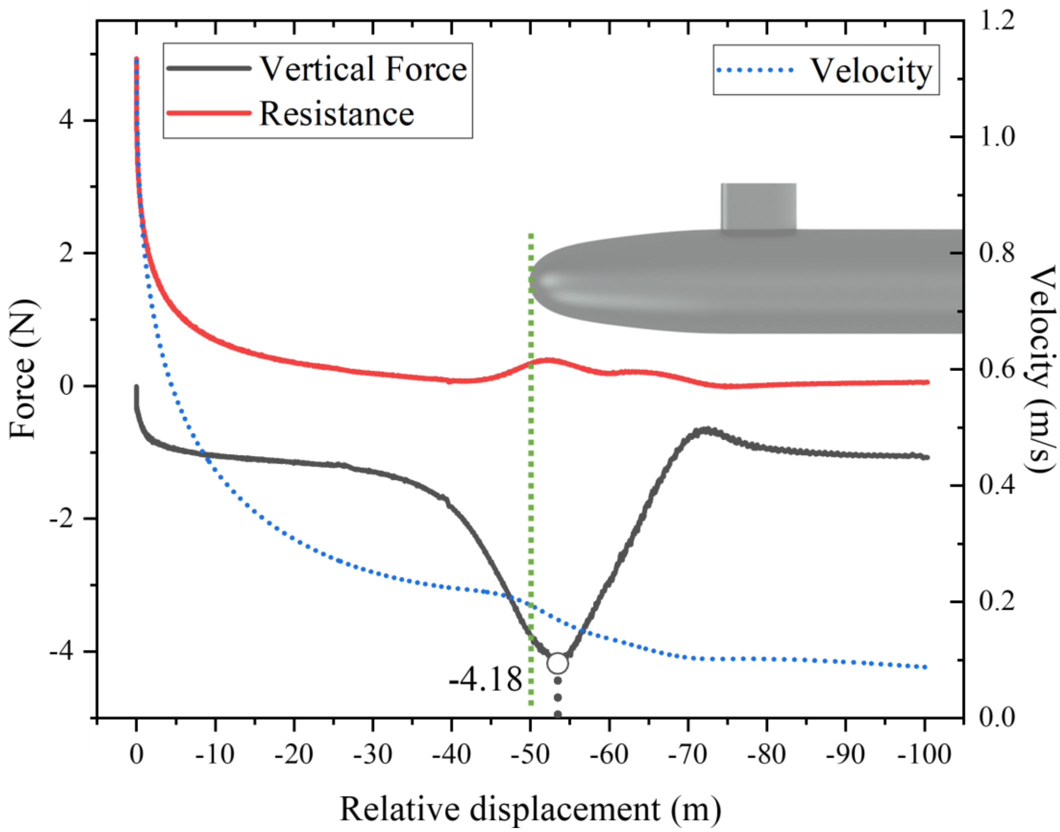

Figure 6-22 The force and the velocity during preparatory process in the capture-type path.

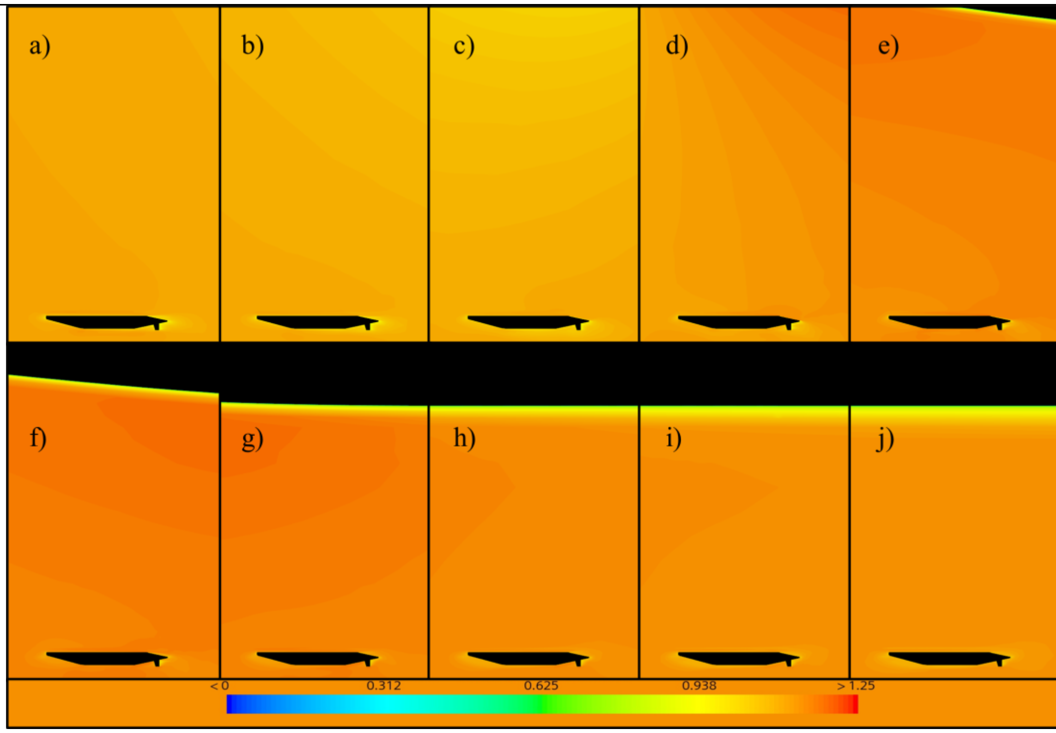

Figure 6-23 The velocity contours during preparatory process in the capture-type path.

In terms of the velocity, after a sudden reduction, the rate of velocity reduction diminishes gradually. After passing 25 m beyond the submarine's bow, the velocity stabilizes, maintaining an approximate velocity of 0.1 m/s between 25m and 50m post-bow. Regarding the resistance, its value tends to approach zero in the absence of thrust. However, within the region influenced by the submarine's bow, fluctuations in resistance are observed, leading to a slight increase. The resistance stabilizes once the AUV moves beyond a distance of 25m from the bow. Regarding the vertical force experienced by the AUV, once the thrust is removed, the vertical force acting on the AUV shifts downwards. Starting from 25m away from the bow of the submarine, the vertical force acting on the AUV increases. Within the affected region around the submarine's bow, the vertical force climbs from approximately 1N to its peak of 4.18N, occurring at a distance of 3.47 m behind the bow. Subsequently, as the AUV moves beyond the 25-meter mark from the bow, the vertical force starts to decline until it stabilizes. Eventually, the force reaches a similar level to the one observed before the AUV approached the bow.

b) Approaching Process in the Capture-Type Path

The velocity contours during the approaching process of the capture-type path are illustrated in Figure 6-24. These contours are mostly similar to those in the approaching-type path, displaying multiple contacts as shown in Figure 6-24 e) ~ h). However, owing to the difference in the initial velocity, which is close to zero, the AUV undergoes a distinct pitch behaviour during the ascending stage. Initially, the AUV pitches up, then pitches down to near zero, and finally pitches up again.

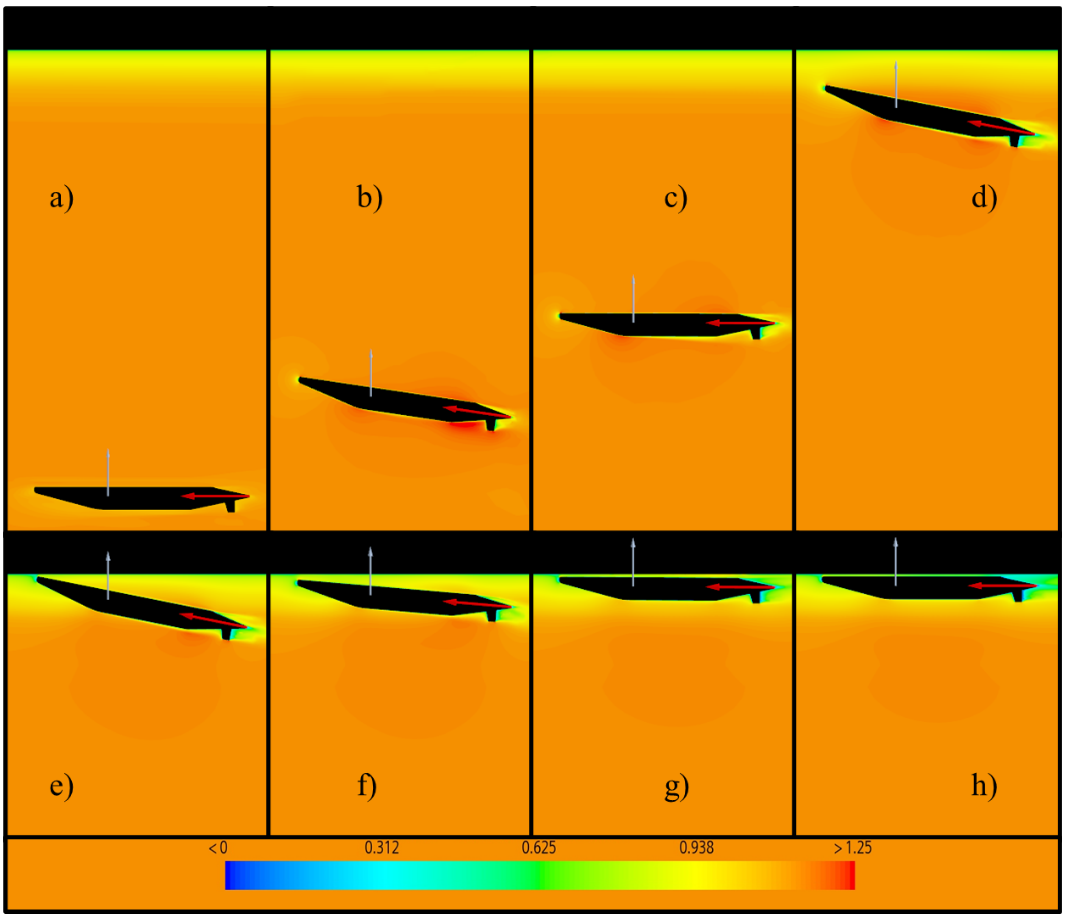

Figure 6-24 The velocity contours during the approaching process of capture-type path.

The vertical fluid force, pitch angle, resistance, AUV velocity and vertical velocity also were monitored. The pitch angle and the vertical velocity are illustrated in Figure 6-25 and Figure 6-26. Until the AUV reaches the boundary layer of the submarine (A-B), both the pitch angle and vertical velocity increases in the first 5 seconds, then decrease between fifth and twelfth seconds, and finally increase again. After entering the boundary layer (B-C), due to the vertical acceleration and angle acceleration being relatively higher, the pitch angle and the vertical velocity do not reduce immediately. The increase in the pitch angle starts to decrease until the AUV reaches to the designed docking region. The increase in the vertical velocity also decreases initially until the AUV travels to the position halfway through the submarine's boundary layer, and then vertical velocity starts to reduce. Once the AUV reached the designated docking region (C point), the vertical velocity also drops rapidly. Meanwhile, because the AUV's bow contact the docking region first, a moment generated by it causes the AUV to rotate counterclockwise until the AUV's bow reaches the docking region again. Before the AUV became stable, several small bounces occur between the time from D to F.

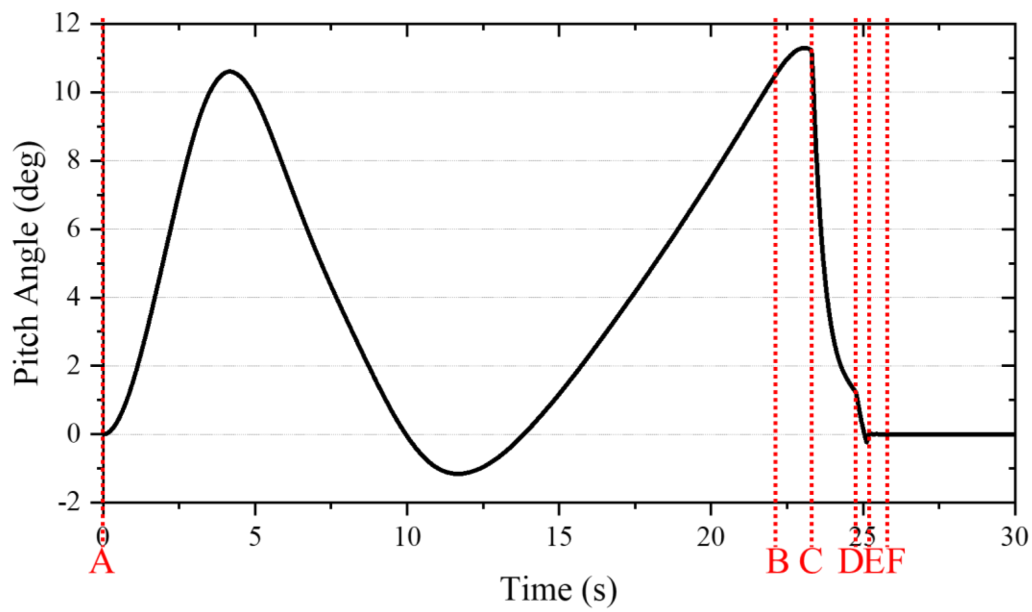

Figure 6-25 The pitch angle of the AUV during the approaching process of the capture-type path.

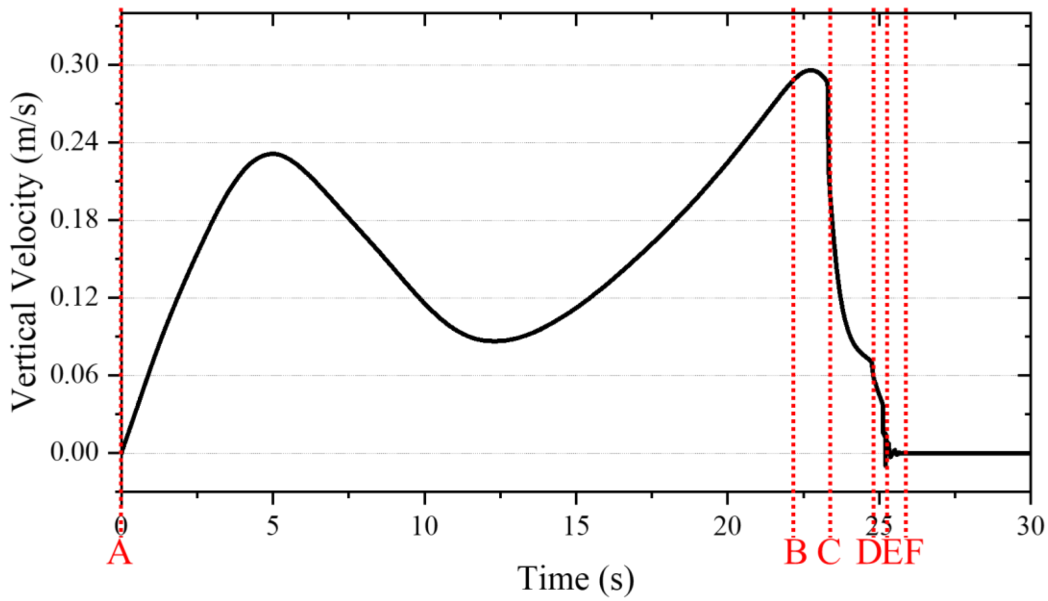

Figure 6-26 The vertical velocity of the AUV during the approaching process of the capture-type path.

In the capture-type path, the vertical fluid force exhibits a similar trend to that in the approaching-type path. Notably, the contact angles are different, measuring 7.67 (approaching-type path) and 11.03 (capture-type path) degrees as the AUV first reaches the docking region. However, the key contact points (C to F) amount to four. The first (C point) and second (D point) contacts occur at the AUV's bow. The third and fourth contacts (E point) occur in a very short period, specifically 0.09s, at the AUV's stern. Following these four main contacts, there are several minor collisions on both the bow and stern of the AUV. The peak impact forces of the four main contacts are 330.931N, 71.6001N, 267.366N, and 298.648N, respectively. These impact forces are not expected to cause potential damage to the AUV, consistent with the discussion of results in the approaching-type path. After docking, a force of 3.133N generated by fluid flow assists in suctioning the AUV towards the submarine, aligning with the results in the approaching-type path.

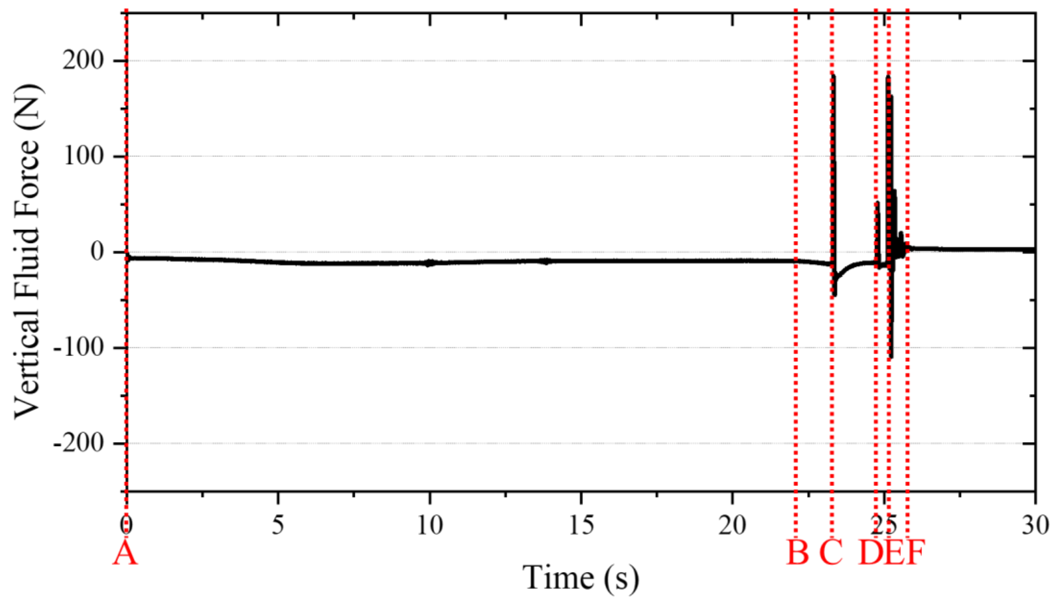

Figure 6-27 The vertical fluid force of the AUV during the approaching process of the capture-type path.

Regarding the AUV velocity, as shown in Figure 6-28, during the ascending stage, the velocity increases faster than that in approaching-type path, but the final velocity is lower. When the AUV enters the boundary layer of the submarine, the AUV velocity remain almost unchanged. In the first contact, the AUV velocity is suddenly reduced and then gradually increased. Meanwhile, as depicted in Figure 6-29, after first contact, the AUV resistance exhibits a similar trend to that in the approaching-type path, with greater fluctuations due to the effects of the four primary contacts. But in the ascending stage, due to the attitude changes, there are also several fluctuations in the resistance. The resistance increases with the increased pitch angle, conversely, the resistance decreases. After the AUV attaches to the submarine, the resistance decreased due to the boundary layer effect, and the velocity keeps rising. This phenomenon aligns with previous section, resulting in an approximately 20% reduction in resistance.

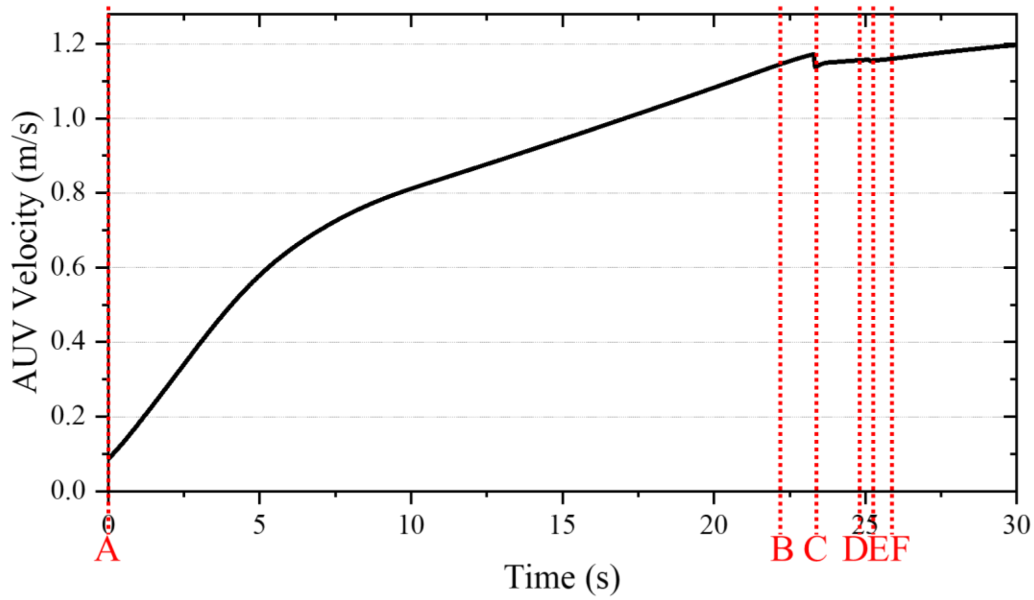

Figure 6-28 The AUV velocity during the approaching process of the capture-type path.

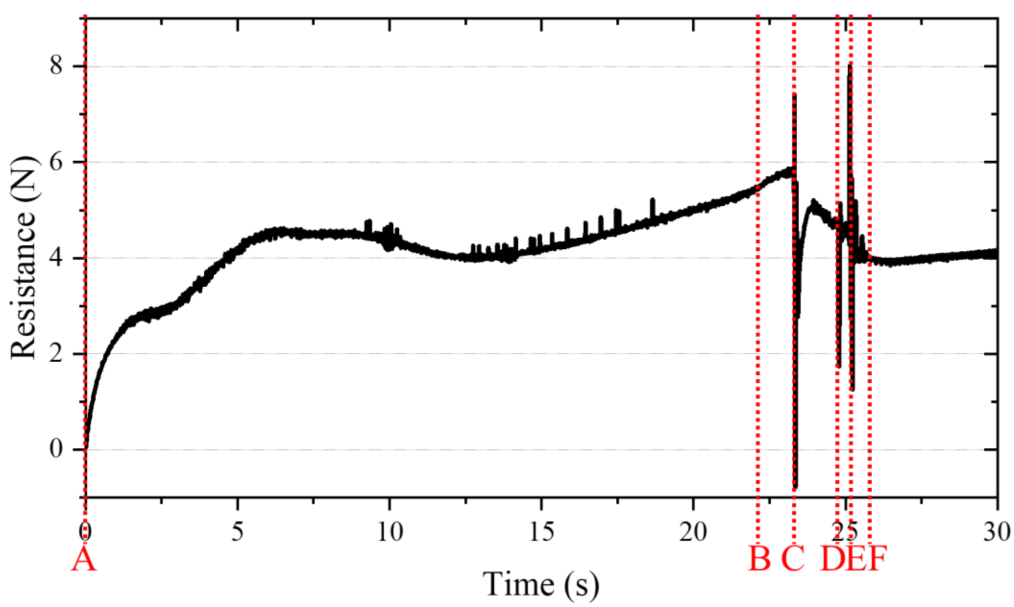

Figure 6-29 The resistance of the AUV during the approaching process of the capture-type path.

In summary, the approaching process of the capture-type path is almost similar to that of the approaching-type path and can be divided into five stages:

1. **Approach (A~B):** The AUV accelerates toward the submarine due to applied forces, and a fluctuation occurs in both pitch angle and vertical velocity.
2. **Enter (B~C):** The AUV enters the boundary layer of the submarine, experiencing a reduction in both vertical acceleration and pitch angle acceleration.
3. **Contact (C~E):** Taking approximately 1.5 seconds, the AUV reaches the designated docking position after entering the boundary layer. This stage involves four main contacts: the first and second on the AUV's bow and the third and the fourth on the AUV's stern. The impact forces peak at 330.931N, 71.6001N, 267.366N, and 298.648N, respectively.
4. **Bounces (E~F):** The AUV slightly bounces on the submarine surface several times, and this bouncing phenomenon quickly cease.
5. **Attach (after F):** The AUV is drawn toward the submarine by a suction force generated by the flow. Additionally, there was an approximately 20% reduction in resistance, further minimizing the force required to capture the AUV.

6.2.5 Result Analysis of the Chase-Type Path

a) Preparatory Process in the Chase-Type Path

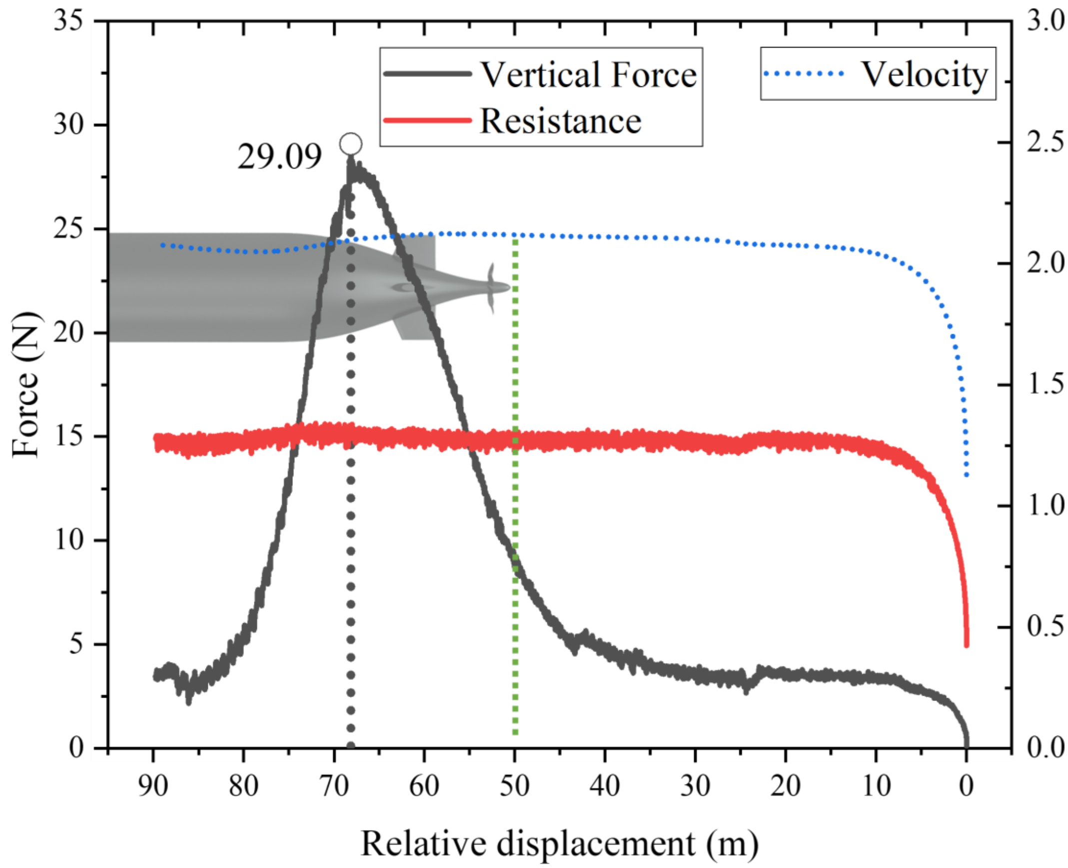

Figure 6-30 The force and the velocity of the AUV during preparatory process in the chase-type path.

Figure 6-30 provides details regarding the forces acting upon the AUV and its velocity in the preparatory process. As the increased propeller speed, there's an initial surge in the velocity, resistance, and vertical force experienced by the AUV. However, after traversing a relative distance of 10m, these parameters stabilize. Nevertheless, due to the complex flow dynamics in the proximity of the submarine's stern, slight oscillations persist in both the vertical force and resistance. Throughout this process, the velocity and resistance exhibit minimal variations until the end. Notably, a brief fluctuation is observed around the transitional region between the submarine's middle hull and stern. In contrast, the vertical force starts to increase significantly at 30m from the propeller. As the AUV advances and reaches a point roughly 68.15m ahead of the propeller, the vertical force reaches a peak value of 29.09 N. Following this peak, the vertical force experiences a sharp drop, reverting back to its initial value prior to the observed increase.

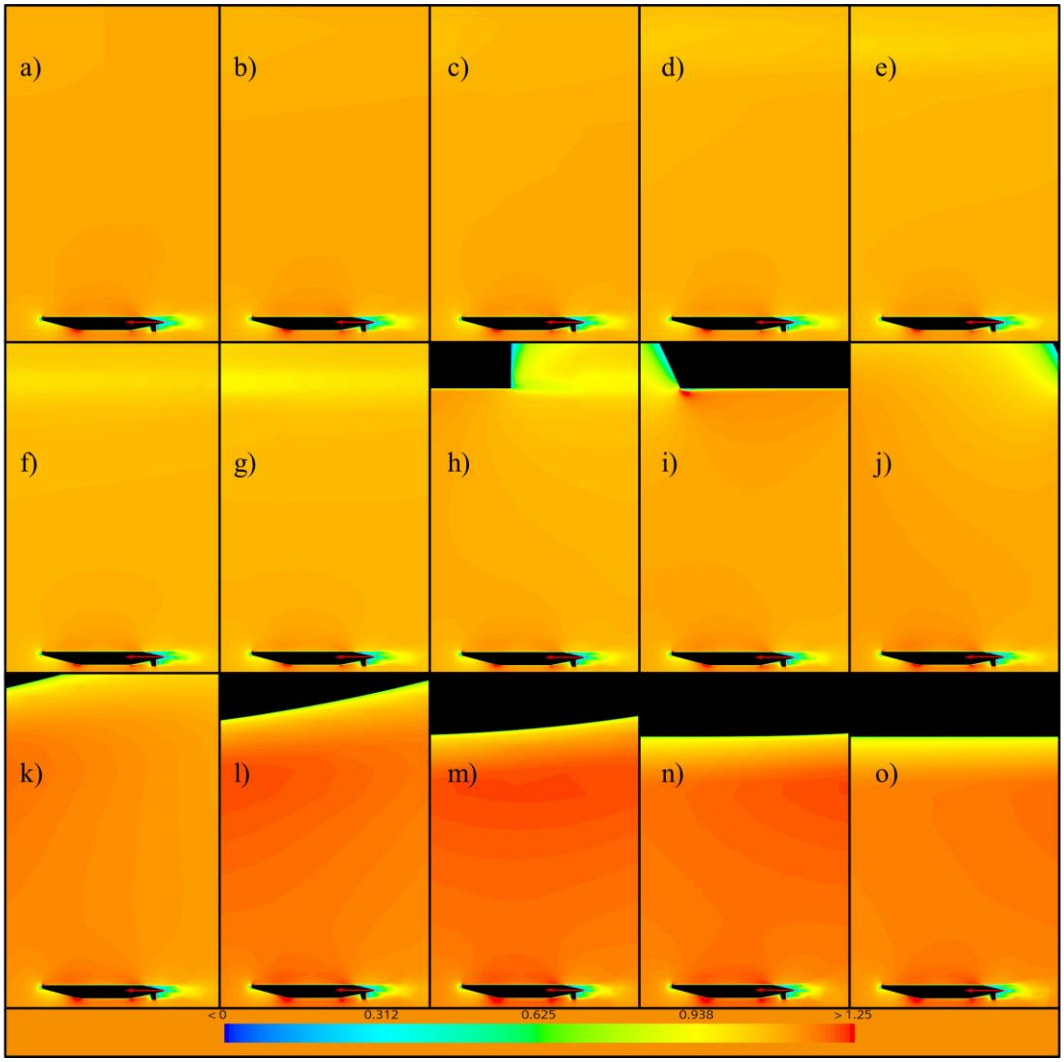

Figure 6-31 The velocity contours during preparatory process in the chase-type path, a) ~ e) the AUV is in the vicinity of the submarine's propeller, f) ~ j) the AUV in the vicinity of the submarine's rudders, k) ~ o) in the vicinity of the transition between the submarine's middle hull and stern.

Figure 6-31 offers a visual representation of the velocity contours as the AUV advances during the preparatory process in the chase-type path.Firstly, from Figure 6-31 a) to e), the AUV is observed near the submarine's propeller. Secondly, spanning Figure 6-31 f) to j), the AUV operates in proximity to the submarine's rudders. Lastly, in Figure 6-31 k) to o), the AUV navigates in the vicinity of the transition region between the submarine's midship hull and stern.

It should be noted that in Figure 6-31 a) ~ e) the low velocity region is the wake behind the submarine’s rudders. On the other hand, given the relatively slow rotational speed of the propeller and an approximate distance of 5L between the propeller and the AUV, the flow velocity contours surrounding the AUV seems to be only slightly affected by submarine’s motion. However, as the AUV approaches the submarine’s rudder and the transition region between the submarine's midship hull and stern, the flow velocity contours around the AUV occur pronounced changes. This is particularly evident in the transition region, where there is a significant area of high pressure.

Comparing the effects of the submarine’s motion when the AUV approaches the bow and stern of the submarine. Previous research by Leong, et al. [102] indicated that, without the appendages and the propeller’s motion, changes in the AUV's vertical force around the bow and stern were similar but in opposite directions. In another study by Luo, et al. [103], which utilized the DARPA Suboff AFF-8 submarine model with full appendages but without the propeller, results indicated that, when the AUV was in close proximity to the submarine, the AUV's lift coefficient under the transition region between the submarine's midship hull and stern was roughly 40% higher than under the submarine's bow. However, under the end point of the submarine (corresponding to the propeller position in this section's study), the AUV's lift coefficient changed only slightly. Combining these findings with the results in this section, it can be demonstrated that when the AUV travels near a self-propulsion submarine, the effects of the rudder in the submarine's stern and the propeller's motion both cannot be ignored, as they jointly significantly impact the vertical force on the AUV.

b) Approaching Process in the Chase-Type Path

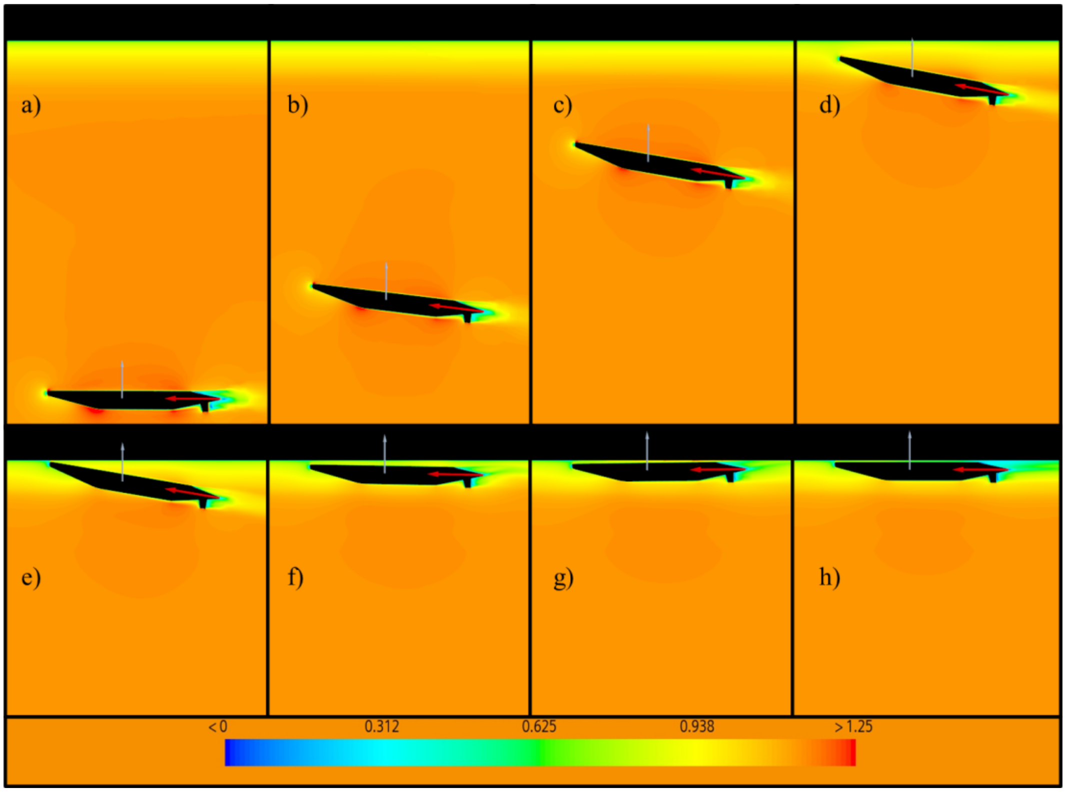

Figure 6-32 The velocity contours during the approaching process of chase-type path.

In Figure 6-32, velocity contours during the approaching process of the chase-type path appear similar to those in the approaching-type path. However, due to the higher initial velocity in the beginning, some differences emerge during the approaching process.

In terms of the pitch angle and vertical velocity, depicted in Figure 6-33 and Figure 6-34, respectively, the trends align with those of the approaching-type path. Both pitch angle and vertical velocity increase before the AUV reaches the submarine's boundary layer (A-B). Once the AUV enters the boundary layer (B-C), they star to decrease. As the AUV reaches the designated docking region (C point), the pitch angle and vertical velocity drop rapidly. However, compared to the other two paths, the total time required for the approaching is shortest, and the fluctuation of the vertical velocity are the largest in the contact stage. The contact angle in this path is 9.46 degree as the AUV first reaches the docking region.

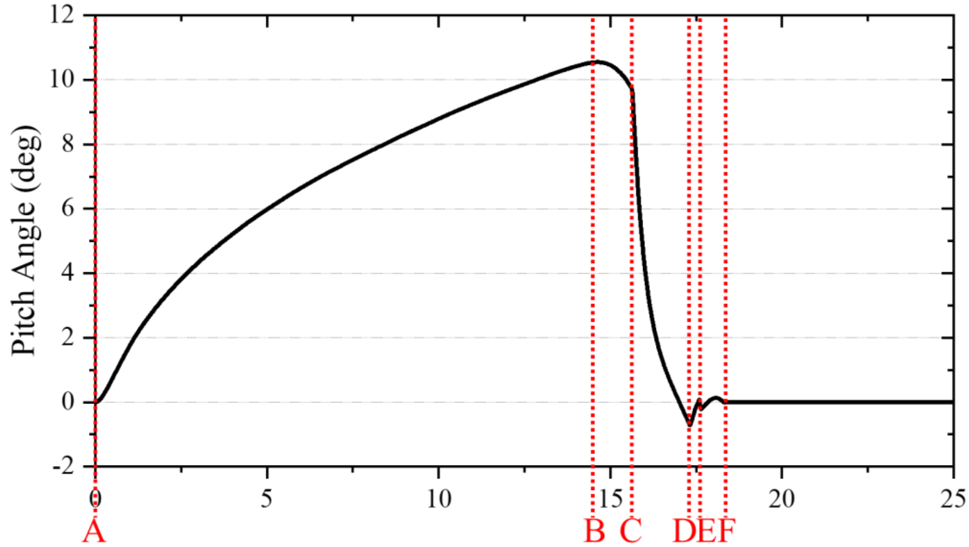

Figure 6-33 The pitch angle of the AUV during the approaching process of the chase-type path.

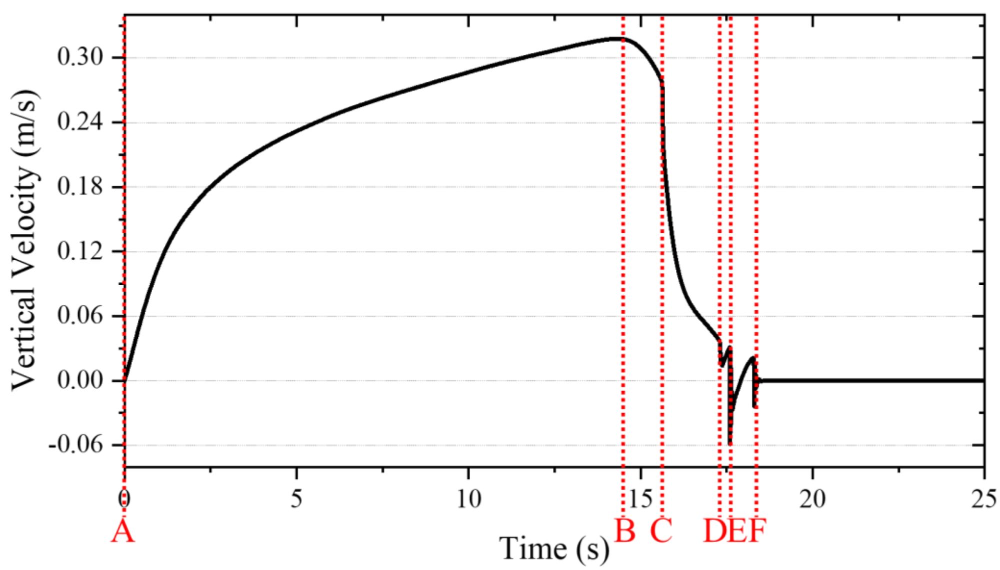

Figure 6-34 The vertical velocity of the AUV during the approaching process of the chase-type path.

Regarding the vertical fluid force on the AUV, as shows in Figure 6-35, there are six key contact points (C to F). The first (C point) and second (D point) contacts occur at the AUV's bow and stern, respectively. At E point and F point, there are two consecutive contacts each, with the AUV impacting once in front and once at the back in very short periods of 0.02s and 0.03s, respectively. The peak impact forces of the six main contacts are 301.277N, 161.044N, 1036.756N, 640.478N, 502.381N and 147.525N, respectively. Following these contacts, several minor contacts happened on both the bow and stern of the AUV. As discussed earlier, these impact forces are not expected to cause potential damage to the AUV. However, it's noteworthy that, despite the roughly 10% difference in contact angle, vertical velocity, and AUV velocity at the first contact between the three paths, the conditions of the contacts differ, resulting in a large difference in peak impact force. After docking, a force of 3.613N generated by fluid flow assists in suctioning the AUV towards the submarine. This force is higher than that in other two paths due to the higher AUV velocity.

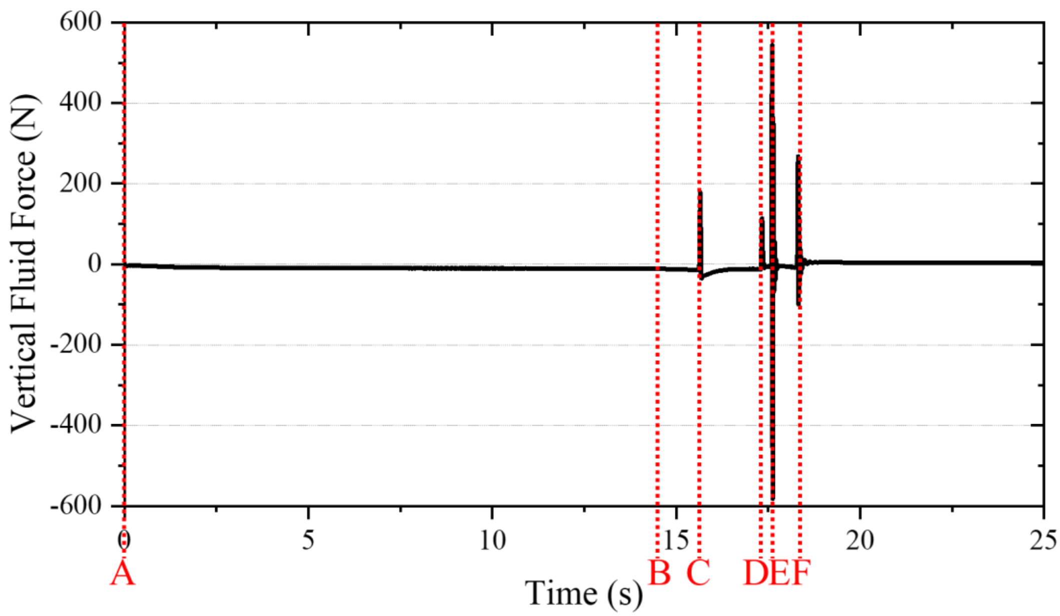

Figure 6-35 The vertical fluid force of the AUV during the approaching process of the chase-type path.

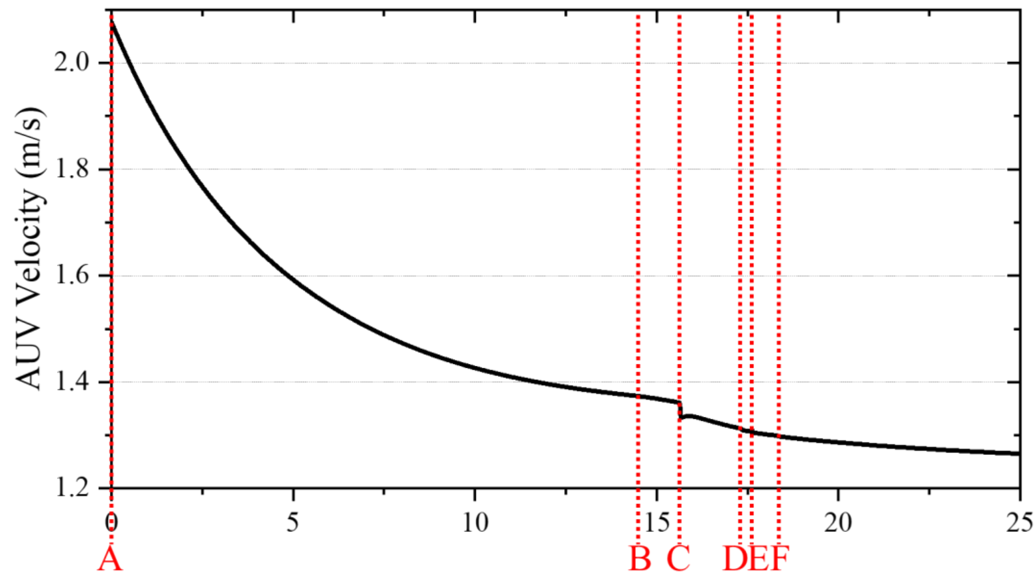

Figure 6-36 The AUV velocity during the approaching process of the chase-type path.

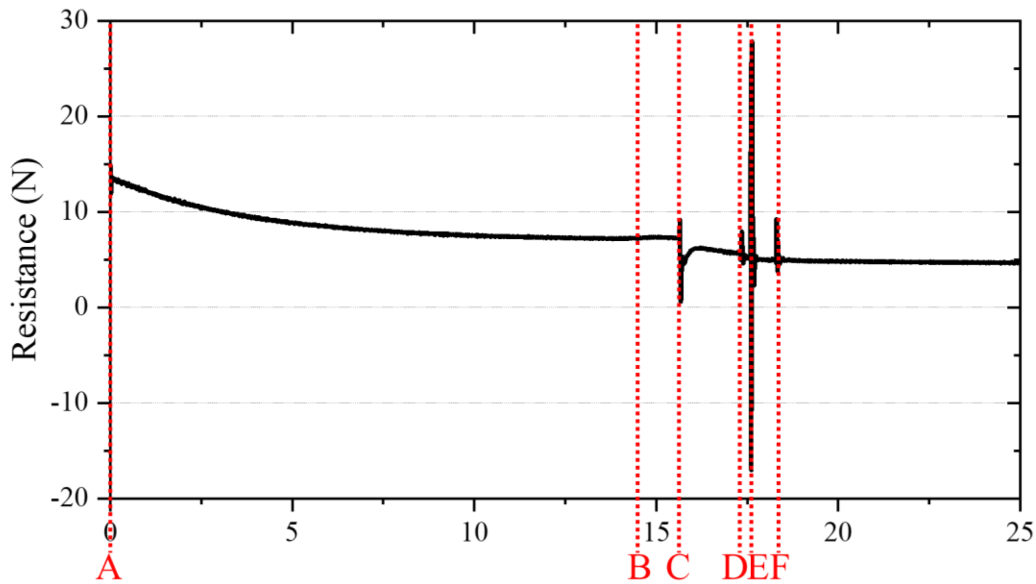

Figure 6-37 The resistance of the AUV during the approaching process of the chase-type path.

For the AUV velocity and resistance as illustrated in Figure 6-36 and Figure 6-37, due to the decreased thrust compared with the approaching process, the overall trend for both is decreasing. Concerning the AUV velocity, the contact velocity is relatively higher in this case, which contributes to the higher peak of the impact force. As for the resistance, after the first contact, there are more significant fluctuations due to the effects of the contacts. Following the AUV's attachment to the submarine, the resistance decreases due to the boundary layer effect, and the velocity continues to decrease. This phenomenon is consistent with the previous section, resulting in an approximately 20% reduction in resistance.

In summary, the approaching process of the chase-type path is also can be divided into five stages:

1. **Approach (A~B):** The AUV accelerates toward the submarine due to applied forces, and the AUV velocity and resistance are reduced as a result of decreased thrust.
2. **Enter (B~C):** The AUV enters the boundary layer of the submarine, experiencing a reduction in both vertical acceleration and pitch angle acceleration.
3. **Contact (C~E):** Taking approximately 1 second, the AUV reaches the designated docking position after entering the boundary layer. This stage involves six main contacts: At E point and F point, there are two consecutive contacts each, with the AUV impacting once in front and once at the back in very short periods of 0.02s and 0.03s, respectively. The peak impact forces of the six main contacts are 301.277N, 161.044N, 1036.756N, 640.478N, 502.381N and 147.525N, respectively.
4. **Bounces (E~F):** The AUV slightly bounces on the submarine surface several times, and this bouncing phenomenon quickly cease.
5. **Attach (after F):** The AUV is drawn towards the submarine by a suction force generated by the flow. Additionally, there was an approximately 20% reduction in resistance, further minimizing the force required to capture the AUV.

6.3 Concluding Remarks

This chapter presents an investigation of the hydrodynamic behaviours of the remora-inspired AUV during the docking operation. Three paths during the docking operation are analysed. These findings provide an understanding of the interaction between the AUV and the environment, and also the hydrodynamics as the AUV makes contact with the submarine. The following concluding remarks can be drawn:

1) A fully coupled analysis has been conducted to investigate the hydrodynamics of the remora-inspired AUV in the docking process. The docking processes can be unfolded in five stages: approach, enter, contact, bounce and attach. After the docking process, the AUV doesn’t require additional vertical thrust force as the fluid force naturally draws the AUV towards the submarine. The suction force increased with the increased forward velocities of the submarine and the AUV. However, since the AUV's propulsion must be halted to prevent potential damage to the submarine, an additional capture device is necessary to finalize the recovery process when the AUV reaches the designated recovery area.

2) In the simulation with the fixed AUV attitude, the docking time and impact force have been analysed, and a shorter docking time will result in a higher impact force.

3) Three recovery paths were proposed in this study: the approaching-type path, the capture-type path, and the chase-type path. Regarding the preparatory processes of recovery paths, when the AUV travels from the front and behind the submarine, there will be repulsion near the submarine’s bow and suction around the submarine’s stern in vertical direction. Additionally, due to the motion of the propeller and the complex stern structures, suction force increases significantly. Therefore, these factors should be considered in path design if the AUV needs to travel around those regions. On the other hand, these areas cause fluctuations in the horizontal motion of the AUV, but the effect is slight.

4) In terms of the approaching process, although these three paths have different initial speed, and there are differences in their states of motion, they can all be clearly categorised into five stages. In all three paths, once the AUV enters the boundary layer, the boundary layer of the submarine will generate a repulsive force on the AUV, which provides effects of reducing the contact speed and angle, but not to the extent of pushing the AUV away from the submarine. In the meantime, as the AUV enters the boundary layer, its resistance decreases gradually, as expected.

5) Among the three designed paths, the capture-type path requires the least energy because the speed required throughout the process is relatively low. Additionally, the impact forces during the contact stage are lower compared to the other two paths. However, as the submarine passes over the AUV from behind, the flow around the submarine's bow can affect the AUV's stability, which should be carefully considered. Furthermore, during the approaching process, the AUV's lower speed leads to greater disturbances in its attitude and vertical velocity.

6) The chase-type path demands higher performance from the AUV to reach the necessary high speed. When the submarine is self-propelled, the combined effects of the rudder and propeller motion at the submarine's stern significantly increase the force on the AUV, suctioning it towards the submarine. Due to the higher initial speed at the start of the approaching process, the impact force during the contact stage is the highest among the three paths.

7) The approaching-type path avoids the AUV passing near the submarine's bow and stern, where suction and repulsion forces are present. However, compared to the capture-type path, this approach demands higher energy consumption and speed. Given these considerations, both the capture-type and approaching-type paths are recommended.

Chapter 7

Conclusions & Recommendations for Future Research

The main objective of Chapter 7 is to provide a thorough overview of the research conducted in this thesis, highlighting the original contributions to the state-of-the-art while addressing the research aims and objectives. The focus is on exploring the feasibility of dynamic recovery systems for AUVs inspired by biomimetic principles. This chapter also summarises the key findings from the research and provides recommendations for future studies.

Following this introduction, Section 7.1 provides a comprehensive overview of the thesis, providing a holistic understanding of the research undertaken. Subsequently, Section 7.2 presents the main conclusions drawn from the research study. The chapter concludes with Section 7.3, which outlines recommendations for future research endeavours.

7.1 Overall Review of the Thesis and Contributions to the State-of-the-Art

AUVs have experienced widespread use and development in recent years. Despite the numerous studies on AUV recovery technologies, there are notable limitations in existing systems. A crucial gap exists in the absence of an underwater dynamic recovery system solution for AUVs that can effectively overcome the constraints of current systems. Moreover, comprehending the hydrodynamics involved when two underwater submersibles of markedly different sizes are in close proximity is imperative to evaluate the viability of such a system. However, existing research in this area is still insufficient.

This PhD project has made original and valuable contributions to the state-of-the-art in researching the feasibility of underwater dynamic recovery for AUVs. The study utilizes biomimetic principles to develop a dynamic recovery strategy employing a remora-inspired AUV. It also explores the implications of the AUV coming into close proximity with underwater vehicles of significantly different sizes. The computational fluid dynamics (CFD) method is employed as the primary tool for achieving these objectives.

The research begins by investigating the hydrodynamic mechanisms of the remora fish when docked to a shark, providing foundational insights from a hydrodynamic perspective. Building upon this understanding of the remora's attachment condition, a remora-inspired AUV is developed, and an optimal docking position on a submarine is identified. Finally, a systematic analysis is conducted to comprehend the hydrodynamics of the remora-inspired AUV during the docking process across various recovery paths. This study enhances confidence in the development of dynamic recovery systems for AUVs. Meanwhile, the research contributes valuable insights of the interactions between two underwater vehicles of significantly different sizes in close proximity. The findings provide an understanding of the hydrodynamics involved in such scenarios, paving the way for more effective designs of dynamic recovery systems for AUVs.

As outlined in **Chapter 1**, the research study had the five main objectives, which were successfully addressed in the thesis, providing insights into AUV recovery strategies, biomimetic design inspired by remora fish, and the dynamics of docking processes. Each chapter of this study contributes to achieving these objectives, as summarized below:

Chapter 2 provided a comprehensive literature review on the state-of-the-art AUV recovery methodologies and explored biomimetic applications inspired by remora fishes. This chapter highlighted significant gaps in current understanding and established the foundation for the research methodology employed throughout this thesis. The review emphasized the need for innovations in dynamic recovery systems and the potential for biomimetic adaptations, addressing *#Objective 1*.

Chapter 3 examined the hydrodynamic characteristics of remora fish in attached swimming conditions, focusing on the effects of boundary layer flows and attachment locations. The findings revealed significant drag reduction benefits, providing insights into the natural adaptations of remoras that can be applied to AUV design. This work addressed *#Objective 2* by enhancing our understanding of the hydrodynamic mechanisms that influence remora behaviour.

Chapter 4 introduced the development of an AUV inspired by remora fish, assessed through computational fluid dynamics. The design improvements led to a notable reduction in resistance, validating the biomimetic approach's effectiveness. The study demonstrated substantial benefits in drag reduction, supporting further application of these principles in AUV design, thereby addressing *#Objective 3*.

Chapter 5 investigated the hydrodynamic performance of the remora-inspired AUV when attached to various submarine locations. The study identified optimal docking positions that maximize efficiency while minimizing risk, taking into account factors such as resistance reduction and operational feasibility. This chapter effectively addressed *#Objective 4*.

Chapter 6 analysed the docking dynamics of the remora-inspired AUV, detailing the stages of docking and the forces involved. The research provided a comprehensive understanding of the interactions between the AUV and the submarine environment, highlighting the benefits of boundary layer interactions in reducing contact speed and resistance. These insights addressed *#Objective 5*.

In addition to reporting the research in this thesis, during the PhD the Author has also published/ publishing parts of this research in numerous respected journals and international conferences listed as follows:

<u>Thesis related paper</u>

1. Xu, Y., Shi, W., Song, Y., & Hou, H. (2024). Hydrodynamics of a remora-inspired autonomous underwater vehicle approaching and docking to a benchmark submarine. *Ocean Engineering, 291*, 116447
2. Xu, Y., Shi, W., Arredondo-Galeana, A., Mei, L., & Demirel, Y. K. (2021). Understanding of remora's “hitchhiking” behaviour from a hydrodynamic point of view. *Scientific Reports, 11*(1), 1-20.
3. Xu, Y., Shi, W., & Song, Y. (2024). Hydrodynamic investigation of a remora-inspired AUV approaching to a self-propulsion submarine during recovery process. In *43rd International Conference on Ocean, Offshore and Arctic Engineering, OMAE2024*.
4. Xu, Y., Shi, W., & Stark, C. (2022, June). Hydrodynamic investigation of a remora-inspired autonomous underwater vehicle docking onto a benchmark submarine. In *41st International Conference on Ocean, Offshore and Arctic Engineering, OMAE2022*.
5. Xu, Y., Shi, W., & Arredondo Galeana, A. (2021, June). Hydrodynamic characteristics of remora's symbiotic relationships. In *9th International Conference on Computational Methods in Marine Engineering.*

<u>Other publications during the PhD</u>

1. Hou, H., Shi, W., Xu, Y., & Song, Y. (2023). Actuator disk theory and blade element momentum theory for the force-driven turbine. *Ocean Engineering*, 285, 115488.

2. Song, Y., Shi, W., Wang, Y., Wu, H., Yang, S., Hou, H., & Xu, Y. (2023). Evaluation of energy consumption and motion accuracy for underwater gliders based on quadrant analysis. *Ocean Engineering*, 285, 115399.
3. Wang, J., Wang, S. Q., Jiang, Q. D., Xu, Y. X., & Shi, W. C. (2023). Effect of Different Raft Shapes on Hydrodynamic Characteristics of the Attenuator-Type Wave Energy Converter. *China Ocean Engineering*, 37(4), 645-659.
4. Ilter, Y. K., Shi, W., Wahren, K., Song, Y., Xu, Y., & Dai, S. (2023, June). A New Concept for a Wave-Propelled Autonomous Surface Vehicle: An Experimental Investigation. In *The 33rd International Ocean and Polar Engineering Conference. OnePetro*.
5. Hou, H., Galeana, A. A., Song, Y., Xu, G., Xu, Y., & Shi, W. (2023). Design of a novel energy harvesting mechanism for underwater gliders using thermal buoyancy engines. *Ocean Engineering*, *278*, 114310.
6. Tadros, M., Xu, Y., Das, T. K., & Shi, W.(2024). Energy efficiency for a hydrogen fueled offshore support vessel. In *43rd International Conference on Ocean, Offshore and Arctic Engineering, OMAE2024*.
7. Stark, C., Shi, W., Xu, Y., & Troll, M. (2022, June). Marine ducted thruster underwater radiated noise control through leading-edge tubercle blade modifications-a numerical hybrid approach. In *41st International Conference on Ocean, Offshore and Arctic Engineering, OMAE2022*.
8. Stark, C., Xu, Y., Zhang, M., Yuan, Z., Tao, L., & Shi, W. (2022). Study on applicability of energy-saving devices to hydrogen fuel cell-powered ships. *Journal of Marine Science and Engineering*, *10*(3), 388.
9. (Under Review) Controller Parameter Optimization for Underwater Gliders based on Energy Consumption and Motion Accuracy, Corresponding Author: Dr. Wendong Niu, Co-Authors: Yang Song; Xiao Yu; Weichao Shi; Hongyu Wu; Yunxin Xu; Wei Ma; Shaoqiong Yang

7.2 Main Conclusion

Complimenting the conclusion and summary of each chapter stated earlier, the following are the main conclusions that can be drawn from the study within the thesis:

1. This thesis investigates the feasibility of an underwater dynamic submersible recovery system incorporating biomimetic principles inspired by remora fish. The study highlights the potential of using natural models to enhance the design and functionality of AUVs, providing an original and useful contribution to the hydrodynamic characterisation of remoras and the interaction of underwater moving vehicles. And to provide new insights for the study of underwater dynamic recovery systems.
2. The thesis provides, for the first time, the results of a systematic and extensive numerical study aimed at utilising this bionic concept to advance the study of underwater dynamic recovery systems. The supporting findings in this study not only further increase confidence in applying this bionic concept to underwater dynamic recovery systems, but also provide reference data for further design of remora-inspired AUVs and interactions between underwater moving vehicles.
3. In terms of the remora most frequent attachment locations of the shark (the belly, the back and the pectoral fin). It is found that the belly and the back locations are the regions with the lowest velocities and adverse pressure gradient regions. This understanding elucidates why remora fish prefer low-velocity regions when attaching to their hosts, providing important insights into the hydrodynamic factors.
4. A remora-inspired AUV hull form is first time developed and evaluated using computational fluid dynamics. The improvements in the hull design, inspired by the remora fish's adaptations, resulted in an enhancement in the AUV's hydrodynamic performance.
5. In term of AUV docking onto the above 9 potential location, combining the resistance reduction effect and the practical operational feasibility, the location at the bottom of the

middle section is recommended. And the resistance reduction of the AUV remains almost constant for velocities

6. The docking processes can be unfolded in five stages: approach, enter, contact, bounce and attach. It was found that leveraging the boundary layer effects can significantly reduce the contact speed and resistance, thus improving the efficiency and safety of the docking operation. After the docking process, the AUV doesn't require additional vertical thrust force as the fluid force sucks the AUV towards the submarine. The suction force increased with the increased forward velocities of the submarine and the AUV. However, since the AUV's propulsion must be halted to prevent potential damage to the submarine, an additional capture device is necessary to finalize the recovery process when the AUV reaches the designated recovery area.
7. When the AUV approaches from the front or rear of the submarine, it encounters repulsion near the bow and suction around the stern in the vertical direction. Additionally, the motion of the propeller and the complex stern structures result in a notable increase in suction force. These factors must be considered when designing paths for the AUV to navigate around these regions. Although these areas cause fluctuations in the AUV's horizontal motion, the effect is relatively minor.
8. In all three paths, once the AUV enters the submarine's boundary layer, it experiences a repulsive force that reduces contact speed and angle, although not enough to push the AUV away from the submarine. Concurrently, the AUV's resistance decreases gradually as it enters the boundary layer, as anticipated.
9. Based on the investigation of the remora-inspired AUV docking onto the submarine, it shows the forces needed to dock the AUV onto the submarine. And it is numerically evidenced to be feasible to perform such operation. Following this research, further confidence has been gained to develop prototype of such bio-inspired AUV.

7.3 Recommendations for Future Research

Based on the thesis research, several future research directions have been identified to further enhance the development of a remora-inspired AUV with an underwater dynamic recovery system. The author is confident that the thesis has effectively met its aims and objectives within the constraints of time and resources. However, the following recommendations for future work are suggested:

Design Improvements of the Remora-Inspired AUV: While significant progress has been made in developing and refining the remora-inspired AUV, further optimization of its hydrodynamic characteristics is necessary. Future research should focus on enhancing its hydrodynamic performance to make it more efficient and suitable for dynamic recovery operations in underwater environments. This could involve exploring new materials, design tweaks, or advanced computational models to fine-tune its performance.

Capture Device of the Recovery System: The current study primarily focuses on the approach process during recovery operations. Future research should evaluate different capture device designs for the recovery system. Assessing various capture mechanisms could provide insights into optimizing the recovery process after the AUV reaches the designated recovery area, ensuring secure and efficient retrieval

Experimental Tests for Prototypes: Conducting experimental tests and sea trials for both the AUV and its recovery system prototypes is crucial. These tests will provide practical insights and validate the theoretical models and simulations used in the study. Real-world trials are essential to assess the feasibility and reliability of the designed system, especially considering the impact of scale and environmental factors on performance.

Reference

[1] J. Falcão Carneiro and F. Gomes de Almeida, "Model and simulation of the energy retrieved by thermoelectric generators in an underwater glider," *Energy Conversion and Management*, vol. 163, pp. 38-49, 2018/05/01/ 2018, doi: https://doi.org/10.1016/j.enconman.2018.02.031.

[2] F. Caruso *et al.*, "Science and dissemination for the UN ocean decade outcomes: Current trends and future perspectives," *Frontiers in Marine Science*, vol. 9, p. 863647, 2022.

[3] D. Pauly, "The Sea Around Us Project: documenting and communicating global fisheries impacts on marine ecosystems," *Ambio*, pp. 290-295, 2007.

[4] R. Lowry, A. Leadbetter, and O. Clements, "Intergovernmental Oceanographic Commission of UNESCO. 2019. Ocean Data Standards, Vol. 4: SeaDataNet Controlled Vocabularies for describing Marine and Oceanographic Datasets-A joint Proposal by SeaDataNet and ODIP projects. Ostend, IODE/UNESCO.(IOC Manuals and Guides, 54, Vol. 4.) 31 pp.(IOC/2019/MG/54 Vol. 4)," *Intergovernmental Oceanographic Commission Manuals and Guides*, 2019.

[5] K. L. Howell *et al.*, "A blueprint for an inclusive, global deep-sea ocean decade field program," *Frontiers in Marine Science*, p. 999, 2020.

[6] D. J. Amon *et al.*, "My Deep Sea, My Backyard: a pilot study to build capacity for global deep-ocean exploration and research," *Philosophical Transactions of the Royal Society B*, vol. 377, no. 1854, p. 20210121, 2022.

[7] O. S. Board and N. R. Council, *Enabling ocean research in the 21st century: Implementation of a network of ocean observatories*. National Academies Press, 2003.

[8] O. Schofield and M. Tivey, "Ocean research interactive observatory networks," *National Science Foundation*, 2005.

[9] O. Schofield *et al.*, "Slocum gliders: Robust and ready," *Journal of Field Robotics*, vol. 24, no. 6, pp. 473-485, 2007.

[10] S. Kemna, M. J. Hamilton, D. T. Hughes, and K. D. LePage, "Adaptive autonomous underwater vehicles for littoral surveillance: the GLINT10 field trial results," *Intelligent service robotics*, vol. 4, pp. 245-258, 2011.

[11] A. L. Forrest, B. E. Laval, R. Pieters, and D. S. Lim, "Convectively driven transport in temperate lakes," *Limnology and Oceanography*, vol. 53, no. 5part2, pp. 2321-2332, 2008.

[12] V. H. Fernandes, A. A. Neto, and D. D. Rodrigues, "Pipeline inspection with AUV," in *2015 IEEE/OES Acoustics in Underwater Geosciences Symposium (RIO Acoustics)*, 2015: IEEE, pp. 1-5.

[13] H. Zhang *et al.*, "The general design of a seafloor surveying AUV system," in *2013 OCEANS-San Diego*, 2013: IEEE, pp. 1-5.

[14] S. Venkatesan, "AUV for Search & Rescue at sea-an innovative approach," in *2016 IEEE/OES Autonomous Underwater Vehicles (AUV)*, 2016: IEEE, pp. 1-9.

[15] J. Nicholson and A. Healey, "The present state of autonomous underwater vehicle (AUV) applications and technologies," *Marine Technology Society Journal*, vol. 42, no. 1, pp. 44-51, 2008.

[16] T. Hardy and G. Barlow, "Unmanned Underwater Vehicle (UUV) deployment and retrieval considerations for submarines," 2008.

[17] E. Hayashi *et al.*, "Customizing an Autonomous Underwater Vehicle and developing a launch and recovery system," in *2013 IEEE International Underwater Technology Symposium (UT)*, 2013: IEEE, pp. 1-7.

[18] J. Heo, J. Kim, and Y. Kwon, "Technology development of unmanned underwater vehicles (UUVs)," *Journal of Computer and Communications,* vol. 5, no. 07, p. 28, 2017.

[19] MBARI, ed.

[20] H. Singh *et al.*, "Docking for an autonomous ocean sampling network," *IEEE Journal of Oceanic Engineering,* vol. 26, no. 4, pp. 498-514, 2001.

[21] P. Sun, X. Wu, J. Cai, X. Zhang, K. Qiao, and H. Shen, "Analysis of special technical problems of wireless charging at UUV docking stations and a new underwater electromagnetic coupler," *Energy Reports,* vol. 8, pp. 719-728, 2022.

[22] M. Lin *et al.*, "Docking to an underwater suspended charging station: Systematic design and experimental tests," *Ocean Engineering,* vol. 249, p. 110766, 2022.

[23] F. Lv, H. Xu, K. Shi, and X. Wang, "Estimation of Positions and Poses of Autonomous Underwater Vehicle Relative to Docking Station Based on Adaptive Extraction of Visual Guidance Features," *Machines,* vol. 10, no. 7, p. 571, 2022.

[24] T. Zhang, D. Li, and C. Yang, "Study on impact process of AUV underwater docking with a cone-shaped dock," *Ocean Engineering,* vol. 130, pp. 176-187, 2017.

[25] B. W. Hobson *et al.*, "The development and ocean testing of an AUV docking station for a 21" AUV," in *OCEANS 2007*, 2007: IEEE, pp. 1-6.

[26] E. I. Sarda and M. R. Dhanak, "A USV-Based automated launch and recovery system for AUVs," *IEEE journal of oceanic engineering,* vol. 42, no. 1, pp. 37-55, 2016.

[27] D. Pearson, E. An, M. Dhanak, K. von Ellenrieder, and P. Beaujean, *High-level fuzzy logic guidance system for an unmanned surface vehicle (USV) tasked to perform autonomous launch and recovery (ALR) of an autonomous underwater vehicle (AUV)*. IEEE, 2014.

[28] P. Norgren, M. Ludvigsen, T. Ingebretsen, and V. E. Hovstein, "Tracking and remote monitoring of an autonomous underwater vehicle using an unmanned surface vehicle in the Trondheim fjord," in *OCEANS 2015-MTS/IEEE Washington*, 2015: IEEE, pp. 1-6.

[29] E. I. Sarda and M. R. Dhanak, "Launch and recovery of an autonomous underwater vehicle from a station-keeping unmanned surface vehicle," *IEEE Journal of Oceanic Engineering,* vol. 44, no. 2, pp. 290-299, 2018.

[30] H. Cho, S.-K. Jeong, D.-H. Ji, N.-H. Tran, M. T. Vu, and H.-S. Choi, "Study on control system of integrated unmanned surface vehicle and underwater vehicle," *Sensors,* vol. 20, no. 9, p. 2633, 2020.

[31] E. Sarda and M. Dhanak, "Unmanned recovery of an AUV from a surface platform manuscript, oceans' 13 MTS/IEEE San Diego," in *2013 OCEANS-San Diego*, 2013: IEEE, pp. 1-6.

[32] F. Y. Lee, B. H. Jun, P. M. Lee, and K. Kim, "Implementation and test of ISiMI100 AUV for a member of AUVs Fleet," in *OCEANS 2008*, 2008: IEEE, pp. 1-6.

[33] K. Albert, ed.

[34] J. M. Brunnschweiler, "Sharksucker-shark interaction in two carcharhinid species," *Marine Ecology*, vol. 27, no. 1, pp. 89-94, 2006, doi: 10.1111/j.1439-0485.2005.00052.x.

[35] M. Beckert, B. E. Flammang, E. J. Anderson, and J. H. Nadler, "Theoretical and computational fluid dynamics of an attached remora (Echeneis naucrates)," *Zoology*, vol. 119, no. 5, pp. 430-438, 2016.

[36] J. M. Silva-Jr and I. Sazima, "Whalesuckers on spinner dolphins: an underwater view," *JMBA2–Biodiversity Records*, 2006.

[37] B. E. Flammang *et al.*, "Remoras pick where they stick on blue whales," *Journal of Experimental Biology*, vol. 223, no. 20, 2020.

[38] W. Nodland, T. Ewart, W. Bendiner, J. Miller, and E. Aagaard, "Spurv ii-an unmanned, free-swimming submersible developed for oceanographic research," in *OCEANS 81*, 1981: IEEE, pp. 92-98.

[39] C. Von Alt, "Autonomous underwater vehicles," in *Autonomous Underwater Lagrangian Platforms and Sensors Workshop*, 2003, vol. 3, p. 2.

[40] A. Sahoo, S. K. Dwivedy, and P. Robi, "Advancements in the field of autonomous underwater vehicle," *Ocean Engineering*, vol. 181, pp. 145-160, 2019.

[41] R. B. Wynn *et al.*, "Autonomous Underwater Vehicles (AUVs): Their past, present and future contributions to the advancement of marine geoscience," *Marine geology*, vol. 352, pp. 451-468, 2014.

[42] E. Bovio, D. Cecchi, and F. Baralli, "Autonomous underwater vehicles for scientific and naval operations," *Annual Reviews in Control*, vol. 30, no. 2, pp. 117-130, 2006.

[43] L. A. Mayer, "Frontiers in seafloor mapping and visualization," *Marine Geophysical Researches*, vol. 27, pp. 7-17, 2006.

[44] K. Zwolak *et al.*, "An unmanned seafloor mapping system: The concept of an AUV integrated with the newly designed USV SEA-KIT," in *OCEANS 2017-Aberdeen*, 2017: IEEE, pp. 1-6.

[45] D. Thompson, D. Caress, C. Paull, D. Clague, H. Thomas, and D. Conlin, "MBARI mapping AUV operations: In the Gulf of California," in *2012 Oceans*, 2012: IEEE, pp. 1-5.

[46] F. L. Chiocci, A. Cattaneo, and R. Urgeles, "Seafloor mapping for geohazard assessment: state of the art," *Marine Geophysical Research*, vol. 32, pp. 1-11, 2011.

[47] J. Escartin, N. Feuillet, and A. Lefriant, "SUBSAINTES'17 Cruise Report. N/O l'Atlante–ROV Victor 6000–AUV AsterX. 2-24 April 2017 Pointe à Pitre (Guadeloupe)-Pointe à Pitre (Guadeloupe)," 2017.

[48] M. Purcell *et al.*, "Use of REMUS 6000 AUVs in the search for the Air France Flight 447," in *OCEANS'11 MTS/IEEE KONA*, 2011: IEEE, pp. 1-7.

[49] D. C. Webb, P. J. Simonetti, and C. P. Jones, "SLOCUM: An underwater glider propelled by environmental energy," *IEEE Journal of oceanic engineering*, vol. 26, no. 4, pp. 447-452, 2001.

[50] J. Sherman, R. E. Davis, W. Owens, and J. Valdes, "The autonomous underwater glider" Spray"," *IEEE Journal of Oceanic Engineering*, vol. 26, no. 4, pp. 437-446, 2001.

[51] C. C. Eriksen *et al.*, "Seaglider: A long-range autonomous underwater vehicle for oceanographic research," *IEEE Journal of oceanic Engineering*, vol. 26, no. 4, pp. 424-436, 2001.

[52] T. Marine. Teledyne Marine. https://www.teledynemarine.com/en-us/products/Pages/slocum-glider.aspx (accessed 2023).

[53] M. SYSTEMS. MRV SYSTEMS. https://www.mrvsys.com/products/spray2 (accessed 2023).

[54] https://www.marinetechnologynews.com/news/fastwave-offers-kongsberg-seagliders-498722 (accessed 2023).

[55] E. Anderlini *et al.*, "A remote anomaly detection system for Slocum underwater gliders," *Ocean Engineering*, vol. 236, p. 109531, 2021.

[56] Z. Wang, C. Yu, M. Li, B. Yao, and L. Lian, "Vertical profile diving and floating motion control of the underwater glider based on fuzzy adaptive LADRC algorithm," *Journal of Marine Science and Engineering*, vol. 9, no. 7, p. 698, 2021.

[57] C. S. Reiss, A. M. Cossio, J. Walsh, G. R. Cutter, and G. M. Watters, "Glider-Based estimates of meso-zooplankton biomass density: a fisheries case study on antarctic krill (Euphausia superba) around the northern antarctic peninsula," *Frontiers in Marine Science*, vol. 8, p. 604043, 2021.

[58] L. A. Kahl, O. Schofield, and W. R. Fraser, "Autonomous gliders reveal features of the water column associated with foraging by Adelie penguins," *Integrative and Comparative Biology*, vol. 50, no. 6, pp. 1041-1050, 2010.

[59] D. K. Mellinger, H. Klinck, N. M. Bogue, J. Luby, H. Matsumoto, and R. Stelzer, "Gliders, floats, and robot sailboats: autonomous platforms for marine mammal research," *The Journal of the Acoustical Society of America*, vol. 131, no. 4_Supplement, pp. 3493-3493, 2012.

[60] M. D. Ohman *et al.*, "Zooglider: An autonomous vehicle for optical and acoustic sensing of zooplankton," *Limnology and Oceanography: Methods*, vol. 17, no. 1, pp. 69-86, 2019.

[61] D. L. Rudnick, R. E. Davis, C. C. Eriksen, D. M. Fratantoni, and M. J. Perry, "Underwater gliders for ocean research," *Marine Technology Society Journal*, vol. 38, no. 2, pp. 73-84, 2004.

[62] D. L. Rudnick, "Ocean research enabled by underwater gliders," *Annual review of marine science*, vol. 8, pp. 519-541, 2016.

[63] J. M. Anderson and N. K. Chhabra, "Maneuvering and stability performance of a robotic tuna," *Integrative and comparative biology*, vol. 42, no. 1, pp. 118-126, 2002.

[64] Y. Cai, S. Bi, and L. Zheng, "Design and experiments of a robotic fish imitating cow-nosed ray," *Journal of Bionic Engineering*, vol. 7, no. 2, pp. 120-126, 2010.

[65] F. E. Fish, "Advantages of aquatic animals as models for bio-inspired drones over present AUV technology," *Bioinspiration & biomimetics*, vol. 15, no. 2, p. 025001, 2020.

[66] F. E. Fish and J. T. Beneski, "Evolution and bio-inspired design: natural limitations," *Biologically inspired design: computational methods and tools*, pp. 287-312, 2014.

[67] M. Kruusmaa *et al.*, "Filose for svenning: A flow sensing bioinspired robot," *IEEE Robotics & Automation Magazine*, vol. 21, no. 3, pp. 51-62, 2014.

[68] A. U. V. A. Center. [Online] Available: https://auvac.org/explore-database/simple-search

[69] kongsberg. kongsberg. https://www.kongsberg.com/maritime/products/marine-robotics/autonomous-underwater-vehicles/AUV-eelume/ (accessed.

[70] G. Bianchi, L. Maffi, M. Tealdi, and S. Cinquemani, "A Bioinspired Cownose Ray Robot for Seabed Exploration," *Biomimetics*, vol. 8, no. 1, p. 30, 2023.

[71] J. Buck, G. Cavalcanti, P. Mandel, E. Schumacher, and S. B. Shiplet, "GhostSwimmer, A Biometric Robot Fish (Boston Engineering)," 2009.

[72] W. Dvorak *et al.*, "GhostSwimmer, A Biometric Robotic Fish (Boston Engineering)," 2010.

[73] T. Van Buren, D. Floryan, A. J. Smits, L. Daniel, and W. Soboyejo, "Bioinspired underwater propulsors," *Bioinspired structures and design*, pp. 113-139, 2020.

[74] P. Liljebäck and R. Mills, "Eelume: A flexible and subsea resident IMR vehicle," in *Oceans 2017-Aberdeen*, 2017: IEEE, pp. 1-4.

[75] Z. Chen, T. I. Um, J. Zhu, and H. Bart-Smith, "Bio-inspired robotic cownose ray propelled by electroactive polymer pectoral fin," in *ASME International Mechanical Engineering Congress and Exposition*, 2011, vol. 54884, pp. 817-824.

[76] G. Bianchi, S. Cinquemani, and F. Resta, "Bio-inspired design of an underwater robot exploiting fin undulation propulsion," *Applied Sciences*, vol. 11, no. 6, p. 2556, 2021.

[77] Y. Cai, S. Bi, G. Li, H. P. Hildre, and H. Zhang, "From natural complexity to biomimetic simplification: The realization of bionic fish inspired by the cownose ray," *IEEE Robotics & Automation Magazine*, vol. 26, no. 3, pp. 27-38, 2018.

[78] T. Hardy and G. Barlow, "Unmanned Underwater Vehicle (UUV) deployment and retrieval considerations for submarines," in *International Naval Engineering Conference and Exhibition 2008*, 2008.

[79] M. Szczotka, "AUV launch & recovery handling simulation on a rough sea," *Ocean Engineering*, vol. 246, p. 110509, 2022.

[80] C. Rauch, M. Purcell, T. Austin, and G. Packard, "Ship of opportunity launch and recovery system for REMUS 600 AUV's," in *OCEANS 2008*, 2008: IEEE, pp. 1-4.

[81] MBARI. https://www.mbari.org/technology/seafloor-mapping-auv/ (accessed 2023).

[82] iatlantic. https://www.iatlantic.eu/expedition_blog/art-of-auv-recovery/ (accessed 2023).

[83] K. Yan and L. Wu, "A survey on the key technologies for underwater AUV docking," *Robot*, vol. 29, no. 3, pp. 267-273, 2007.

[84] L. Meng, Y. Lin, H. Gu, G. Bai, and T.-C. Su, "Study on dynamic characteristics analysis of underwater dynamic docking device," *Ocean Engineering*, vol. 180, pp. 1-9, 2019.

[85] L. Meng, Y. Lin, H. Gu, and T.-C. Su, "Study on dynamic docking process and collision problems of captured-rod docking method," *Ocean Engineering*, vol. 193, p. 106624, 2019.

[86] J. M. Cena, "Power transfer efficiency of mutually coupled coils in an aluminum AUV hull," Monterey, California: Naval Postgraduate School, 2013.

[87] B. Allen *et al.*, "Autonomous docking demonstrations with enhanced REMUS technology," in *OCEANS 2006*, 2006: IEEE, pp. 1-6.

[88] B. R. Page and N. Mahmoudian, "Simulation-driven optimization of underwater docking station design," *IEEE Journal of Oceanic Engineering*, vol. 45, no. 2, pp. 404-413, 2019.
[89] T. Fukasawa, T. Noguchi, T. Kawasaki, and M. Baino, "" MARINE BIRD", a new experimental AUV with underwater docking and recharging system," in *Oceans 2003. Celebrating the Past... Teaming Toward the Future (IEEE Cat. No. 03CH37492)*, 2003, vol. 4: IEEE, pp. 2195-2200.
[90] J. Zhou *et al.*, "AUH, a new technology for ocean exploration," *Engineering*, vol. 25, pp. 21-27, 2023.
[91] C. Cai *et al.*, "A resident subsea docking system with a real-time communication buoy moored by an electro-optical-mechanical cable," *Ocean Engineering*, vol. 271, p. 113729, 2023.
[92] M. S. Services. https://www.modus-ltd.com/ (accessed 2024).
[93] H. Dong, Z. Wu, J. Wang, D. Chen, M. Tan, and J. Yu, "Implementation of autonomous docking and charging for a supporting robotic fish," *IEEE Transactions on Industrial Electronics*, vol. 70, no. 7, pp. 7023-7031, 2022.
[94] P. Balcombe *et al.*, "How to decarbonise international shipping: Options for fuels, technologies and policies," *Energy conversion and management*, vol. 182, pp. 72-88, 2019.
[95] M. Lin *et al.*, "Underwater fluid-driven soft dock for dynamic recovery of AUVs with improved pose tolerance," *Ocean Engineering*, vol. 309, p. 118466, 2024.
[96] Z. Yan, P. Gong, and W. Zhang, "Dynamic docking technology between AUV and mobile mothership," in *2020 Chinese Control And Decision Conference (CCDC)*, 2020: IEEE, pp. 3045-3049.
[97] F. Raspante, "Underwater mobile docking of autonomous underwater vehicles," *Proceedings of the 2012 Oceans, Hampton Roads, VA, USA*, pp. 14-19, 2012.
[98] B. R. Page and N. Mahmoudian, "AUV docking and recovery with USV: An experimental study," in *OCEANS 2019-Marseille*, 2019: IEEE, pp. 1-5.
[99] 기영이, "Consideration of launch and recovery systems for operation of underwater robot from manned platform," *Journal of Ocean Engineering and Technology*, vol. 30, no. 2, pp. 141-149, 2016.
[100] Q. Chen and R. Sun, "Analysis of launch and recovery UUV model for submarine," *Ship Sci. Technol*, vol. 33, pp. 146-149, 2011.
[101] Z. Wu, X. Guo, W. Yin, and B. Hunag, "Research on underwater recovery technology for underwater special vehicles," *Ship Science and Technology*, vol. 32, no. 2, pp. 140-143, 2016.
[102] Z. Q. Leong, D. Ranmuthugala, I. Penesis, and H. Nguyen, "Quasi-static analysis of the hydrodynamic interaction effects on an autonomous underwater vehicle operating in proximity to a moving submarine," *Ocean engineering*, vol. 106, pp. 175-188, 2015.
[103] W. Luo, C. Ma, D. Jiang, T. Zhang, and T. Wu, "The Hydrodynamic Interaction between an AUV and Submarine during the Recovery Process," *Journal of Marine Science and Engineering*, vol. 11, no. 9, p. 1789, 2023.
[104] M. Beckert, B. E. Flammang, and J. H. Nadler, "Remora fish suction pad attachment is enhanced by spinule friction," *J Exp Biol*, vol. 218, no. Pt 22, pp. 3551-8, Nov 2015, doi: 10.1242/jeb.123893.

[105] S. Su *et al.*, "Vertical Fibrous Morphology and Structure-Function Relationship in Natural and Biomimetic Suction-Based Adhesion Discs," *Matter*, vol. 2, no. 5, pp. 1207-1221, 2020, doi: 10.1016/j.matt.2020.01.018.

[106] D. Weihs, F. E. Fish, and A. J. Nicastro, "Mechanics of Remora Removal by Dolphin Spinning," *Marine Mammal Science*, vol. 23, no. 3, pp. 707-714, 2007, doi: 10.1111/j.1748-7692.2007.00131.x.

[107] F. Ayerst, ed.

[108] A. Izzotti, ed.

[109] D. W. Strasburg, "Some aspects of the feeding behavior of Remora remora," 1962.

[110] K. E. Cohen, B. E. Flammang, C. H. Crawford, and L. P. Hernandez, "Knowing when to stick: touch receptors found in the remora adhesive disc," *R Soc Open Sci*, vol. 7, no. 1, p. 190990, Jan 2020, doi: 10.1098/rsos.190990.

[111] Y. Wang *et al.*, "A biorobotic adhesive disc for underwater hitchhiking inspired by the remora suckerfish," *Science Robotics*, vol. 2, no. 10, 2017.

[112] S. H. Lee, H. W. Song, B. S. Kang, and M. K. Kwak, "Remora-inspired reversible adhesive for underwater applications," *ACS applied materials & interfaces*, vol. 11, no. 50, pp. 47571-47576, 2019.

[113] H. Jia, X. Peng, and C. Lang, "Remora optimization algorithm," *Expert Systems with Applications*, vol. 185, p. 115665, 2021.

[114] Y. P. Papastamatiou *et al.*, "Optimal swimming strategies and behavioral plasticity of oceanic whitetip sharks," *Sci Rep*, vol. 8, no. 1, p. 551, Jan 11 2018, doi: 10.1038/s41598-017-18608-z.

[115] H. Singh, D. F. Fletcher, and J. J. Nijdam, "An assessment of different turbulence models for predicting flow in a baffled tank stirred with a Rushton turbine," *Chemical Engineering Science*, vol. 66, no. 23, pp. 5976-5988, 2011.

[116] STAR-CCM+guidelines, "STAR-CCM+ Documentation."

[117] F. R. Menter, "Two-equation eddy-viscosity turbulence models for engineering applications," *AIAA journal*, vol. 32, no. 8, pp. 1598-1605, 1994.

[118] E. H. Williams Jr *et al.*, "Echeneid–sirenian associations, with information on sharksucker diet," *Journal of Fish Biology*, vol. 63, no. 5, pp. 1176-1183, 2003.

[119] CMS. "Puerto Rico (USA)." CMS SHARKS MOU. https://www.cms.int/sharks/en/country/puerto-rico-usa (accessed 17 December, 2019).

[120] R. Lessa, F. M. Santana, and R. Paglerani, "Age, growth and stock structure of the oceanic whitetip shark, Carcharhinus longimanus, from the southwestern equatorial Atlantic," *Fisheries Research*, vol. 42, no. 1-2, pp. 21-30, 1999.

[121] ITTC, "Practical guidelines for ship CFD applications," in *26th ITTC*, Hague, 2011, p. 18.

[122] T. Knopp, "Model-consistent universal wall-functions for RANS turbulence modelling," in *International Conference on Boundary and Interior Layers, Göttingen, Germany*, 2006: Citeseer.

[123] F. R. Menter, M. Kuntz, and R. Langtry, "Ten years of industrial experience with the SST turbulence model," *Turbulence, heat and mass transfer*, vol. 4, no. 1, pp. 625-632, 2003.

[124] L. Oggiano, F. Pierella, T. A. Nygaard, J. De Vaal, and E. Arens, "Comparison of experiments and CFD simulations of a braceless concrete semi-submersible platform," *Energy Procedia*, vol. 94, pp. 278-289, 2016.

[125] K. Chen, D.-b. Huang, and Y.-b. Li, "Grid convergence study in the resistance calculation of a trimaran," *Journal of Marine Science and Application,* vol. 7, no. 3, pp. 174-178, 2008, doi: 10.1007/s11804-008-7065-1.

[126] I. B. Celik, U. Ghia, P. J. Roache, and C. J. Freitas, "Procedure for estimation and reporting of uncertainty due to discretization in CFD applications," *Journal of fluids Engineering-Transactions of the ASME,* vol. 130, no. 7, 2008.

[127] H.-L. Liu and T. T. Huang, "Summary of DARPA SUBOFF experimental program data," NAVAL SURFACE WARFARE CENTER CARDEROCK DIV BETHESDA MD HYDROMECHANICS …, 1998.

[128] A. T. Chwang and Z. Dong, *Viscous Fluid Mechanics*. Tsinghua University Press, 2011.

[129] T.-H. Shih, *A generalized wall function*. National Aeronautics and Space Administration, Glenn Research Center, 1999.

[130] R. F. Roddy, "Investigation of the stability and control characteristics of several configurations of the DARPA SUBOFF model (DTRC Model 5470) from captive-model experiments," David Taylor Research Center Bethesda MD Ship Hydromechanics Dept, 1990.

[131] S. Sezen, A. Dogrul, C. Delen, and S. Bal, "Investigation of self-propulsion of DARPA Suboff by RANS method," *Ocean Engineering,* vol. 150, pp. 258-271, 2018.

[132] N. Chase and P. M. Carrica, "Submarine propeller computations and application to self-propulsion of DARPA Suboff," *Ocean Engineering,* vol. 60, pp. 68-80, 2013.

[133] F. Di Felice, M. Felli, M. Liefvendahl, and U. Svennberg, "Numerical and experimental analysis of the wake behavior of a generic submarine propeller," *Prism,* vol. 1, no. 8, p. 158, 2009.

[134] "7.5-02-03-01.1 Testing and Extrapolation Methods Propulsion, Performance Propulsion Test," *ITTC – Recommended Procedures and Guidelines*.

[135] S. Sezen, C. Delen, A. Dogrul, and M. Atlar, "An investigation of scale effects on the self-propulsion characteristics of a submarine," *Applied Ocean Research,* vol. 113, p. 102728, 2021.

[136] Q. T. Do, T. Muttaqie, P.-T. Nhut, M. T. Vu, N. D. Khoa, and A. R. Prabowo, "Residual ultimate strength assessment of submarine pressure hull under dynamic ship collision," *Ocean Engineering,* vol. 266, p. 112951, 2022.

[137] W. Pan and Y. Zhang, "Research on Dynamic Docking Process and Collision Problems of AUV Based on Joint Control Simulation," in *2021 7th International Conference on Computer and Communications (ICCC)*, 2021: IEEE, pp. 1057-1061.